COPY

AD-A220 810

REPORT DOCUMENTATION PAGE

Form Approved
OMB No. 0704-0188

1. AGENCY USE ONLY (*Leave blank*)

2. REPORT DATE
March 1990

3. REPORT TYPE AND DATES COVERED
Paper Jan 89 - Sep 89

4. TITLE AND SUBTITLE
Thin-Layer Navier-Stokes Solutions of the Asymmetric Vortical Flow on a Tangent Ogive Body

5. FUNDING NUMBERS
PE: 61102F
PR: 2307
TA: E1
WU: 26

AUTHOR(S)
AFATL Program Manager: Kirk J. Vanden

PERFORMING ORGANIZATION NAME(S) AND ADDRESS(ES)
Aerodynamics Branch
Aeromechanics Division
Air Force Armament Laboratory (AFATL/FXA)
Eglin Air Force Base, FL 32542-5434

8. PERFORMING ORGANIZATION REPORT NUMBER
AFATL-TP-90-04

SPONSORING/MONITORING AGENCY NAME(S) AND ADDRESS(ES)

10. SPONSORING/MONITORING AGENCY REPORT NUMBER

DTIC
ELECTE
APR 12 1990
S D
D

11. SUPPLEMENTARY NOTES
This paper was not edited nor published by AFATL/DOIR.

12a. DISTRIBUTION/AVAILABILITY STATEMENT
Approved for public release; distribution is unlimited

12b. DISTRIBUTION CODE

13. ABSTRACT (*Maximum 200 words*)

Laminar solutions for asymmetric vortical flow on a five caliber tangent ogive with an eight caliber cylindrical afterbody were calculated with a thin-layer Navier-Stokes code on a one block algebraic grid.

Solutions were obtained for Mach 1.4 at 25, 30, 37.5, 38.5, and 40 degrees angle of attack. The Reynolds number for all cases was 200,000 based on the maximum body diameter. Two-dimensional particle traces in cross-sections of the flow and the limiting streamlines were calculated from the solutions.

The validity of the thin-layer approximation in the flow field far away from the boundary layer was studied by recomputing the 37.5 degree case with the viscosity turned off at a distance away from the body. The solution was not significantly different, indicating that the outer vortex flow is basically inviscid.

Both symmetric and asymmetric cases were calculated and analyzed. The secondary flow was shown in detail. The complexity of the secondary flow increased with angle of attack.

Crossflow topology diagrams were given in detail for symmetric and asymmetric conditions to illustrate the fundamental difference between

14. SUBJECT TERMS

15. NUMBER OF PAGES

16. PRICE CODE

17. SECURITY CLASSIFICATION OF REPORT	18. SECURITY CLASSIFICATION OF THIS PAGE	19. SECURITY CLASSIFICATION OF ABSTRACT	20. LIMITATION OF ABSTRACT
UNCLASSIFIED	UNCLASSIFIED	UNCLASSIFIED	SAR

90 04 12 107

13. ABSTRACT (CONCLUDED)

these conditions. Asymmetry, according to this research, was characterized by the change in the topological structure near the saddle point associated with the primary vortices. In addition, the creation of vortex by ~~the~~ pinching of another vortex, was found to occur. This phenomenon was observed in both the primary and secondary flow.

The singular points obtained from the two-dimensional particle traces satisfied the topological summation rule for two-dimensional sections of a three-dimensional flow. The primary separation and associated vortices agree qualitatively with experimental data. The secondary separation region, however, contained additional topological structures that have not been resolved in previous experimental studies.

PREFACE

This paper was prepared by Kirk J. Vanden of the Computational Fluid Dynamics Section, Aerodynamics Branch, Aeromechanics Division, Air Force Armament Laboratory, Eglin Air Force Base, Florida. The work was performed under Work Unit 2307E126 during the period from January 1989 to September 1989.

This paper presents an investigation of asymmetric vortical flow on a tangent ogive body based upon solutions obtained by a thin-layer Navier-Stokes code in use in the Computational Fluid Dynamics Section.

TABLE OF CONTENTS

Page

CHAPTER

LIST OF FIGURES

KEY TO SYMBOLS

a_∞	freestream speed of sound
c	local speed of sound
CFL	Courant number
e	total specific energy
F,G,H	curvilinear coordinate flux vectors
G^d	diffusive flux vector
J	metric Jacobian (cell volume)
l	reference length
L	length of body
M	Mach number
N	nodal point
n	normal coordinate
P	pressure
P_r	Prandtl number
q	heat flux
Q	curvilinear coordinate dependent variable vector
Re	Reynolds number
S	saddle point
t	time
T	temperature
u,v,w	Cartesian velocity components
U,V,W	contravariant velocities
V_∞	freestream velocity

x,y,z	cartesian coordinates
α	angle of attack
β	side slip angle
γ	ratio of specific heats
ρ	density
μ	fluid dynamic viscosity
ν	fluid kinematic viscosity
τ	transformed time variable, fluid stress vector
ξ,η,ζ	curvilinear coordinates
ω	vorticity

Subscripts

i,j,k	grid point location
L	laminar
∞	freestream values
ξ,η,ζ	partial differentiation
x,y,z	partial differentiation

Superscripts

n	time level
'	half singular point

CHAPTER I

INTRODUCTION

The purpose of this research is to investigate asymmetric vortical flow around a body of revolution at high angles of attack. The phenomena of interest are the sheets of vorticity formed on the leeward side at moderate angles of attack. At low angles of attack the flow separates symmetrically on both sides of a body of revolution at some point between the windward and leeward sides. The separated flow rolls up into a pair of symmetric vortices. At moderate angles of attack the vortices become asymmetric but steady and move away from the body with respect to the downstream direction, while new vortices form underneath them. At even higher angles of attack the flow in the wake becomes unsteady and the vortices alternately shed off the body. Asymmetric vortices can induce large asymmetric loads on the body, even at zero sideslip. The vortex induced sideforce can easily exceed the normal force[1]. Wind tunnel tests of the F-111[2] have shown the vortex-induced yawing moment can exceed the available control authority, through full rudder deflection, by an order of magnitude. Also, vehicle roll can cause the vortex induced forces and moments to switch from left to right suddenly, especially on missiles flying uncoordinated manuevers.

In this analysis, a modified version of the Program EAGLE - Flow Solver[3] is used to solve the thin-layer approximation to the Navier-Stokes equations to obtain the separated flow solutions. Program

EAGLE - Grid Generator is used to construct the algebraic grid. This research uses a framework for the observation of aerodynamic flows which stresses physical features and descriptive mathematics[4]. To provide a systematic and rigorous base to this framework the mathematics of topology is used. Topology had its beginning in the observation that there are a number of geometrical properties that are unchanged by continuous deformations. The use of topology in aerodynamics was first introduced systematically by Legendre[5], who noted that the important structures of the flow can be described by a finite number of singular (critical) points which must conform to summation rules. The topology of singular points has proved to be a very useful tool in analyzing skin-friction patterns and streamlines from experimental studies or numerical calculations.

Experimental studies of asymmetric vortex flow have been conducted by many researchers. Lamont[6] performed low Mach number wind tunnel tests of an ogive-cylinder and identified two mechanisms for producing asymmetric flow. One mechanism operates in the fully laminar or fully turbulent regime and is qualitatively described by the impulsive flow analogy. The second mechanism observed was in transitional flow and is analogous to the two-dimensional crossflow on a circular cylinder in the transitional separation regime. Yanta[7] et al. performed wind tunnel tests of a tangent ogive in low turbulence incompressible flow with asymmetric vortices. These results supported hydrodynamic instability as being a cause of vortex asymmetry. The leeside flow was examined in detail including the streamlines and singular points on two-dimensional cross sections of the flow. The effect of nose bluntness was found to have no effect on the basic qualitative topological structure in the crossflow plane. Keener[8] conducted subsonic and supersonic wind tunnel tests of ogival, parabolic, and conical forebodies over a wide range of Reynolds numbers. The principle cause of vortex asymmetry was also found to be the hydrodynamic instability of the inviscid flow field with additional asymmetry being observed in the boundary layer at transitional conditions. Nose bluntness was observed to add additional structure in one case. An additional vortex pair, not observed on sharp nosed ogives, was observed above the primary vortices on a blunted ogive forebody. These vortices were believed to be generated at the nose. Chapman[4] discusses the topology of bodies of revolution in general and notes that, except for crossflow shocks, the topology is basically the same for both subsonic and supersonic flows. Keener[9] et al. and Keener and Chapman[10] have conducted wind tunnel measurements of asymmetric induced forces and moments on various bodies of revolution for both subsonic and supersonic flows, with the former study noting that as the Mach number approaches supersonic values the vortex-induced side force approaches zero. The control of vortex orientation has been investigated by Peake[11] et al. using injection of air near the nose, and by Fidler[12] who used rotation of the nose region.

Several numerical investigations have also been done. Ying[13] et al. conducted transonic laminar thin-layer Navier-Stokes calculations of the asymmetric vortical flow on a hemisphere cylinder and studied the connection between surface flow topology and the surfaces of separation. More recently, Siclari and Marconi[14] calculated supersonic laminar formation of steady asymmetric vortices on a cone. These calculations were converged to machine zero using a Navier-Stokes algorithm modified with the assumption of conical flow.

In this thesis, details of the secondary flow associated with asymmetric vortex flow are numerically investigated and found to agree qualitatively with previous experimental results. In addition, the crossflow topology for a number of angles of attack is given to illustrate the difference between symmetric flow and various asymmetric flows.

A description of the governing equations and the numerical algorithm is given in Chapter II followed by a description of the use of topology in the analysis of fluid flows in Chapter III. The numerical grids and convergence history are given in Chapter IV. Finally, Chapter V presents and discusses the results of the calulations performed.

CHAPTER II

FLOW SOLVER

The boundary-layer equations are useful for many different types of viscous flows. However, there are many problems in which the boundary-layer assumption is not valid and a more exact form of the Navier-Stokes equations must be used. The current problem of the high angle-of-attack flow over a body of revolution is an example. The thin-layer approximation to the complete Navier-Stokes equations is particularly useful in this case since separated and reverse flow regions can still be computed but with a significant decrease in computational requirements. In the formal derivation of the unsteady boundary-layer equations all terms on the order of $1/(Re_l)^{1/2}$ and smaller are neglected. This results in the viscous terms containing derivatives in the directions parallel to the body being dropped since they are significantly smaller than the viscous term normal to the boundary. In addition, the momentum equation is reduced to a simpler equation in which the pressure normal to the wall is constant. In the thin-layer approximation the viscous terms parallel to the body are dropped again, but all other terms of the momentum equation are retained. The thin-layer Navier-Stokes equations are a mixed set of hyperbolic-parabolic partial differential equations.

The thin-layer Navier-Stokes Program EAGLE flow solver calculates the viscous terms explicitly and implements them after the inviscid terms have been calculated in an implicit upwind method. The inviscid portion of the algorithm optionally uses either flux-vector split or flux-difference split finite-volume formulations. By computing the viscous terms explicitly the cost of the thin-layer algorithm is only about

15% greater than the Euler algorithm on an identical grid. This is due to the separate calculation of the inviscid terms for which upwind differencing is most effective. Whitfield[15] developed the baseline algorithm with flux-vector splitting, Belk and Whitfield[16] extended it to obtain time-accurate solutions on multi-block grids, and Gatlin and Whitfield[17] added the thin-layer approximation.
The version of the Program EAGLE flow solver used in this study was further modified by Simpson[18] to include a flux-difference splitting scheme due to Roe[19]. This scheme was used for all calculations performed.

2.1 Thin-Layer Navier-Stokes Approximation

In the thin-layer approximation all viscous terms except those normal to the body are eliminated from the full Navier-Stokes equations. The thin-layer Navier-Stokes equations are transformed using generalized boundary conforming curvilinear coordinates to allow the implementation of boundary conditions for arbitrary geometries. These curvilinear coordinates are

$$\begin{aligned} \xi &= \xi(x,y,z) \\ \eta &= \eta(x,y,z) \\ \zeta &= \zeta(x,y,z) \\ \tau &= t. \end{aligned} \tag{1}$$

Applying this transformation, the non-dimensional, divergence form of the time-dependent thin-layer Navier-Stokes equations become

$$\frac{\partial Q}{\partial \tau} + \frac{\partial F}{\partial \xi} + \frac{\partial G}{\partial \eta} + \frac{\partial H}{\partial \zeta} = \frac{\partial G^d}{\partial \eta}, \tag{2}$$

where

$$Q = J\begin{bmatrix}\rho \\ \rho u \\ \rho v \\ \rho w \\ e\end{bmatrix},$$

$$F = J\begin{bmatrix}\rho U \\ \rho u U + \xi_x P \\ \rho v U + \xi_y P \\ \rho w U + \xi_z P \\ U(e+P)\end{bmatrix} \quad \text{and } U = \xi_x u + \xi_y v + \xi_z w,$$

$$G = J\begin{bmatrix}\rho V \\ \rho u V + \eta_x P \\ \rho v V + \eta_y P \\ \rho w V + \eta_z P \\ V(e+P)\end{bmatrix} \quad \text{and } V = \eta_x u + \eta_y v + \eta_z w,$$

$$H = J\begin{bmatrix}\rho W \\ \rho u W + \zeta_x P \\ \rho v W + \zeta_y P \\ \rho w W + \zeta_z P \\ W(e+P)\end{bmatrix} \quad \text{and } W = \zeta_x u + \zeta_y v + \zeta_z w,$$

$$G^d = \begin{bmatrix} 0 \\ \eta_x \tau_{xx} + \eta_y \tau_{xy} + \eta_z \tau_{xz} \\ \eta_x \tau_{yx} + \eta_y \tau_{yy} + \eta_z \tau_{yz} \\ \eta_x \tau_{zx} + \eta_y \tau_{zy} + \eta_z \tau_{zz} \\ \{\eta_x (u\tau_{xx} + v\tau_{xy} + w\tau_{xz} - q_x) + \\ \eta_y (u\tau_{yx} + v\tau_{yy} + w\tau_{yz} - q_y) + \\ \eta_z (u\tau_{zx} + v\tau_{zy} + w\tau_{zz} - q_z)\} \end{bmatrix}.$$

Here u, v, and w are the velocity components in the x, y, and z cartesian coordinates, respectively, ρ is the density of the gas, P is the pressure, and γ is the ratio of the specific heats. U,V, and W are the contravariant velocities and J is the Jacobian of the inverse transformation and is given by

$$J = x_\xi(y_\eta z_\zeta - z_\eta y_\zeta) - y_\xi(x_\eta z_\zeta - z_\eta x_\zeta) + z_\xi(x_\xi y_\zeta - y_\eta x_\zeta). \qquad (4)$$

Assuming a perfect gas the total specific energy of the fluid can be given as

$$e = [P/(\gamma - 1)] + (\rho/2)[u^2 + v^2 + w^2]. \qquad (3)$$

For this finite volume method the Jacobian is the volume of a computational cell. The metric quantities are given by

$$\xi_x = J^{-1}(y_\eta z_\zeta - z_\eta y_\zeta),\ \eta_x = J^{-1}(z_\xi y_\zeta - y_\xi z_\zeta),\ \zeta_x = J^{-1}(y_\xi z_\eta - z_\xi y_\eta)$$

$$\xi_y = J^{-1}(z_\eta x_\zeta - x_\eta z_\zeta),\ \eta_y = J^{-1}(x_\xi z_\zeta - z_\xi x_\zeta),\ \zeta_y = J^{-1}(z_\xi x_\eta - x_\xi z_\eta)$$

$$\xi_z = J^{-1}(x_\eta y_\zeta - y_\eta x_\zeta),\ \eta_z = J^{-1}(y_\xi x_\zeta - x_\xi y_\zeta),\ \zeta_z = J^{-1}(x_\xi y_\eta - y_\xi x_\eta)$$

and give the projected area of cell faces on the cartesian coordinate planes when multiplied by the Jacobian. The stress terms are

$$\tau_{xx} = \frac{2}{3}\frac{\mu M_\infty}{Re}\,[2\eta_x u_\eta - \eta_y v_\eta - \eta_z w_\eta]$$

$$\tau_{yy} = \frac{2}{3}\frac{\mu M_\infty}{Re}\,[2\eta_y v_\eta - \eta_x u_\eta - \eta_z w_\eta]$$

$$\tau_{zz} = \frac{2}{3}\frac{\mu M_\infty}{Re}\,[2\eta_z w_\eta - \eta_x u_\eta - \eta_y v_\eta]$$

and

$$\tau_{xy} = \frac{\mu M_\infty}{Re}\,[\eta_y u_\eta + \eta_x v_\eta]$$

$$\tau_{xz} = \frac{\mu M_\infty}{Re}\,[\eta_z u_\eta + \eta_x w_\eta]$$

$$\tau_{zy} = \frac{\mu M_\infty}{Re}\,[\eta_y w_\eta + \eta_z v_\eta].$$

The heat flux terms in the thin-layer assumption are

$$q_x = \frac{[\eta_x T_\eta]}{(\gamma - 1)} \left[\frac{\mu M_\infty}{P_r Re}\right]$$

$$q_y = \frac{[\eta_y T_\eta]}{(\gamma - 1)} \left[\frac{\mu M_\infty}{P_r Re}\right]$$

$$q_z = \frac{[\eta_z T_\eta]}{(\gamma - 1)} \left[\frac{\mu M_\infty}{P_r Re}\right].$$

2.2 Boundary Conditions

If the governing equations are cast in characteristic variable form there will be an eigenvalue associated with each characteristic variable indicating the direction in which information is propogated across each constant computational surface. This is the basis for determining boundary conditions known as characteristic variable boundary conditions. This technique is implemented by a layer of phantom points surrounding the block boundaries at which the change in dependent variables is taken to be zero. Since these boundary conditions are treated explicitly, they are first-order accurate. Characteristic variable boundary conditions are employed at all farfield boundaries except the one at the rear of the body. It was found that when using characteristic variable boundary conditions on this boundary, negative densities were generated at the phantom points and propagated forward through the subsonic boundary layer. Therefore, the flow solver was modified to implement extrapolated boundary conditions in this region.

No-slip conditions are applied to the momentum terms at impermeable surfaces. The momentum values at the body surface are mirrored with negative values at the image point. This gives a zero momentum flux at solid wall boundaries. The normal temperature derivative is set to zero at the shearing surface for adiabatic wall conditions. Since the normal pressure gradient is assumed to be negligible at the solid wall, the boundary conditions for energy and density are given as

$$\frac{\partial e}{\partial n}\Big|_w = 0 \qquad \text{and} \qquad \frac{\partial \rho}{\partial n}\Big|_w = 0. \tag{5}$$

CHAPTER III

TOPOLOGY

The mathematical basis for the behavior of the elementary singular points of skin-friction lines and the topological rules these points obey have been known for a long time. Davey[20] and Lightill[21] were the first to point out that skin-friction lines must obey a specific topological rule: the sum of nodal points and foci must exceed the number of saddle points by two. Nodal points, foci, and saddle points are examples of singular points (Figure 1). Singular points are divided into two types known as nodes and saddle points. Node points are further divided into nodal points and foci. These singular points in the skin-friction lines occur at isolated locations on the surface where the surface vorticity and skin-friction become identically zero.

A nodal point is the point that is common to an infinite number of skin-friction lines. All the lines associated with that point, except one, are tangential to a single common line. At a nodal point of separation, all the skin friction lines are directed inward toward the node. At a nodal point of attachment, all the skin-friction lines are directed away from the node. A focus differs from a nodal point in that an infinite number of skin-friction lines spiral around the singular points. The lines spiral away from an attachment focus while a separation focus has all the lines spiraling into it. The singular point associated with a saddle point has only two skin-friction lines that pass

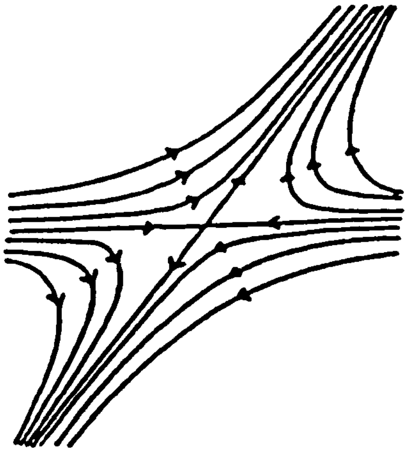

Saddle Point

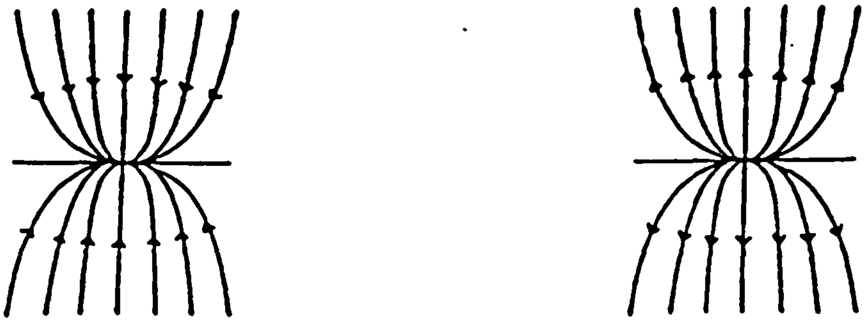

Node of
Separation

Node of
Attachment

Spiral Nodes
FOCI

Figure 1. Singular Points

through it. The halves of one line are directed inwards towards the center while the halves of the remaining line are directed outwards. These two lines act as barriers, making one set of skin-friction lines inaccessible to an adjacent set.

3.1 Topology of Streamlines

J.H.B. Smith[22], Perry and Fairlie[23], and J.C.R Hunt[24] et al. were the first to report that the rules governing skin-friction line behavior are easily extended to yield similar rules governing behavior of the flow itself. The singular points of streamlines in any of the sectional views of a steady three-dimensional flow must obey topological rules also. All of the singular points that are observed in skin-friction lines also appear in the topology of streamlines. In addition, half-nodes and half-saddles can occur on the boundary. A singular point in these sectional views is a point (x_0, y_0) where the velocity is identically zero. This can be stated as

$$\begin{aligned} u(x_0, y_0) &= 0 , \\ v(x_0, y_0) &= 0 . \end{aligned} \qquad (6)$$

With the assumption of a continuous vector field, isolated critical points conform to topological summation rules. For a three-dimensional simply connected body, the critical points in a sectional view must satisfy the relation

$$\left(\sum N + \tfrac{1}{2}\sum N'\right) - \left(\sum S + \tfrac{1}{2}\sum S'\right) = -1 \qquad (7)$$

where N denotes nodes and S indicates saddles with the primes denoting half singular points.

3.2 Topology of Separation

Topology has also played a key role in defining the nature of separated flows. Tobak and Peake[25] have given a definition of attached and separated flows in which they define two types of separation called global and local. An attached flow is defined as a flow containing two and only two singular points in the skin-friction lines. These two points are a nodal point of attachment and a nodal point of separation. Global separation occurs when the skin-friction patterns contain more than two nodal points. For every nodal point over two a saddle point must exist. This topological rule is stated as

$$\sum N - \sum S = 2 \tag{8}$$

For example, when the flow contains three nodal points of which two must be the same type the lines emanating from these alike nodal points must be prevented from crossing. The separatrixes of a saddle point provide the needed barrier. A separation line is defined as one of these two separatrixes. To summarize Tobak and Peake[25], skin-friction lines for attached flow cannot contain any saddle points, while they must contain at least one saddle point in globally separated flow.

Crossflow separation, however, does not always obey this topological rule. The skin-friction lines on a body with only a crossflow type of separation contain only lines connecting the nodal point of attachment at the nose with the nodal point of separation at the rear. This is the same topological pattern that exists without crossflow separation. Even though no separation saddle point exists, converging streamlines can squeeze together at a rate that forces the fluid away from the body. The line on which the limiting streamlines eventually converge appears to emerge from the region of the attachment node on the nose. This type of separation is known as local separation. The concept of limiting streamlines, first used by Sears[26] and later extended by Legendre[27], becomes important for determining the point at which the flow is forced away from the body. Limiting streamlines are streamlines that, except near flow separation, exist infinitesimally close to the surface of the body and their direction is the same as the skin-friction lines. Therefore, the limiting streamlines can be viewed as a surface of streamlines whose projection on the body are skin-friction lines.

Limiting streamlines rising on either side of the line of separation are prevented from crossing by a stream surface which emanates from the line of separation itself. On a body of revolution the dividing surfaces usually roll up into vortices as they progress downstream.

CHAPTER IV

NUMERICAL CALCULATIONS

The configuration selected for this research is a five caliber tangent ogive nose with a circular afterbody eight diameters long. This configuration was selected because of the wide range of experimental studies performed using tangent ogive shapes.

4.1 Numerical Grids

The grids used in this analysis were generated using the Program EAGLE - Numerical Grid Generation System[28] developed jointly by the Air Force Armament Laboratory's Computational Fluid Dynamics Section and the Department of Aerospace Engineering of Mississippi State University.

The single block algebraic fine grid (Figures 2 and 3) has 70 axial, 60 normal, and 100 circumferential points. This equates to a total of 420,000 grid points. The thin-layer Navier-Stokes solutions on this grid required over 114 million words of core memory on the Cray-2 machine at the United States Air Force SuperComputer Center-Kirtland(AFSCC-K). This grid was used for all calculations except for a grid refinement study. A single block algebraic grid (Figures 4 and 5) with 60 axial, 50 normal, and 61 circumferential points was used for a grid refinement study at 30.0 degrees angle of attack. The results of

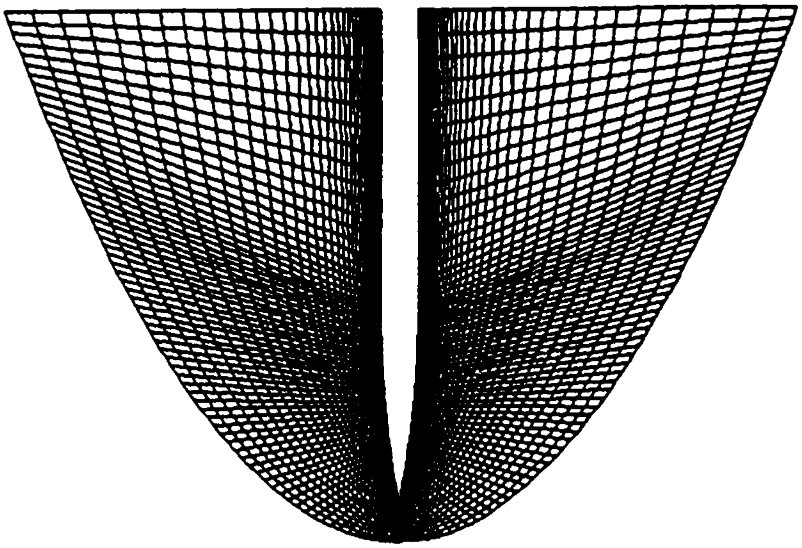

Figure 2. Algebraic Fine Grid - Side View

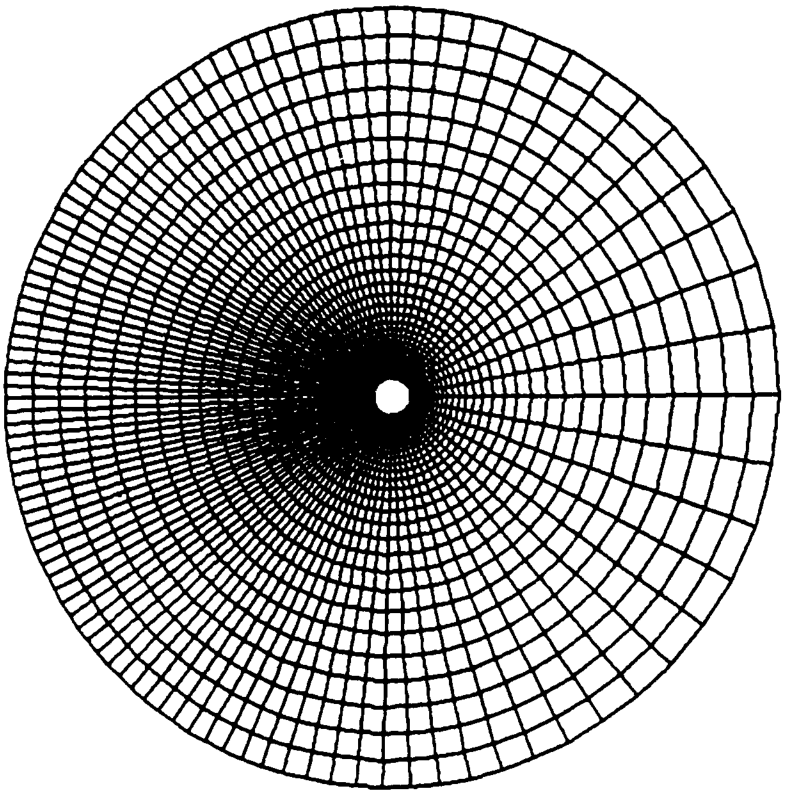

Figure 3. Algebraic Fine Grid - Back Plane

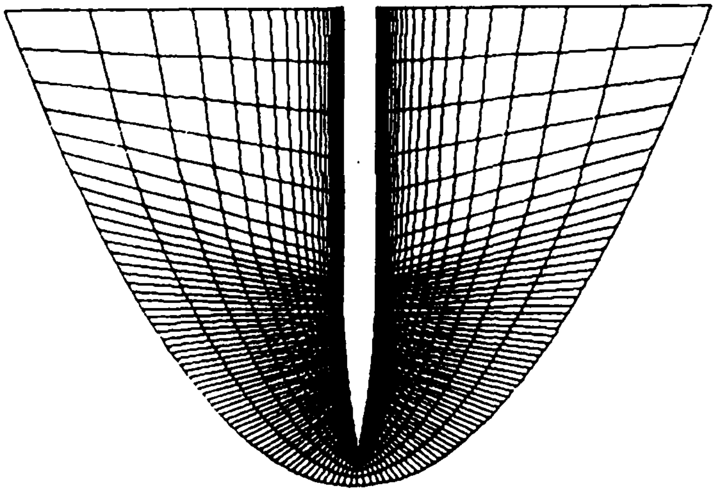

Figure 4. Algebraic Coarse Grid - Side View

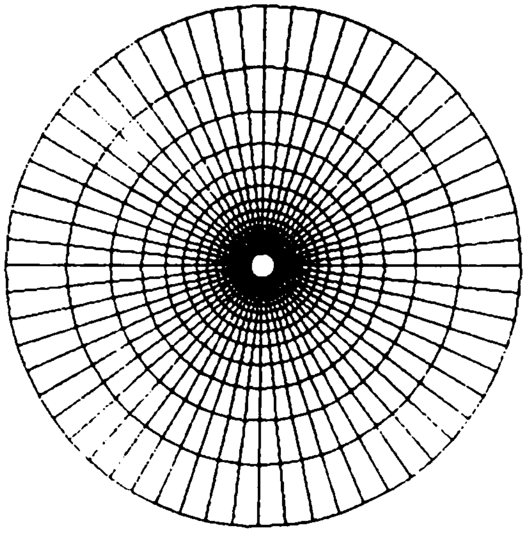

Figure 5. Algebraic Coarse Grid - Back Plane

the grid refinement study are discussed in the analysis chapter.

4.2 Convergence History

Due to the slow rate of convergence typical of viscous solution algorithms, it was impractical to obtain solutions converged to machine zero. The L2 norm of the residual were reduced between three and four orders of magnitude for all calculations. To insure that the flow structure was not dependent on the convergence level, contours of flow variables were compared to insure that no visible change had occured in the last 500 iterations. Typical convergence histories are show.. in Figures 6 and 7. Figure 6 is a symmetric vortex case at an angle of attack of 25 degrees, and Figure 7 shows the convergence history for a 30 degree angle of attack case, which is an asymmetric condition.

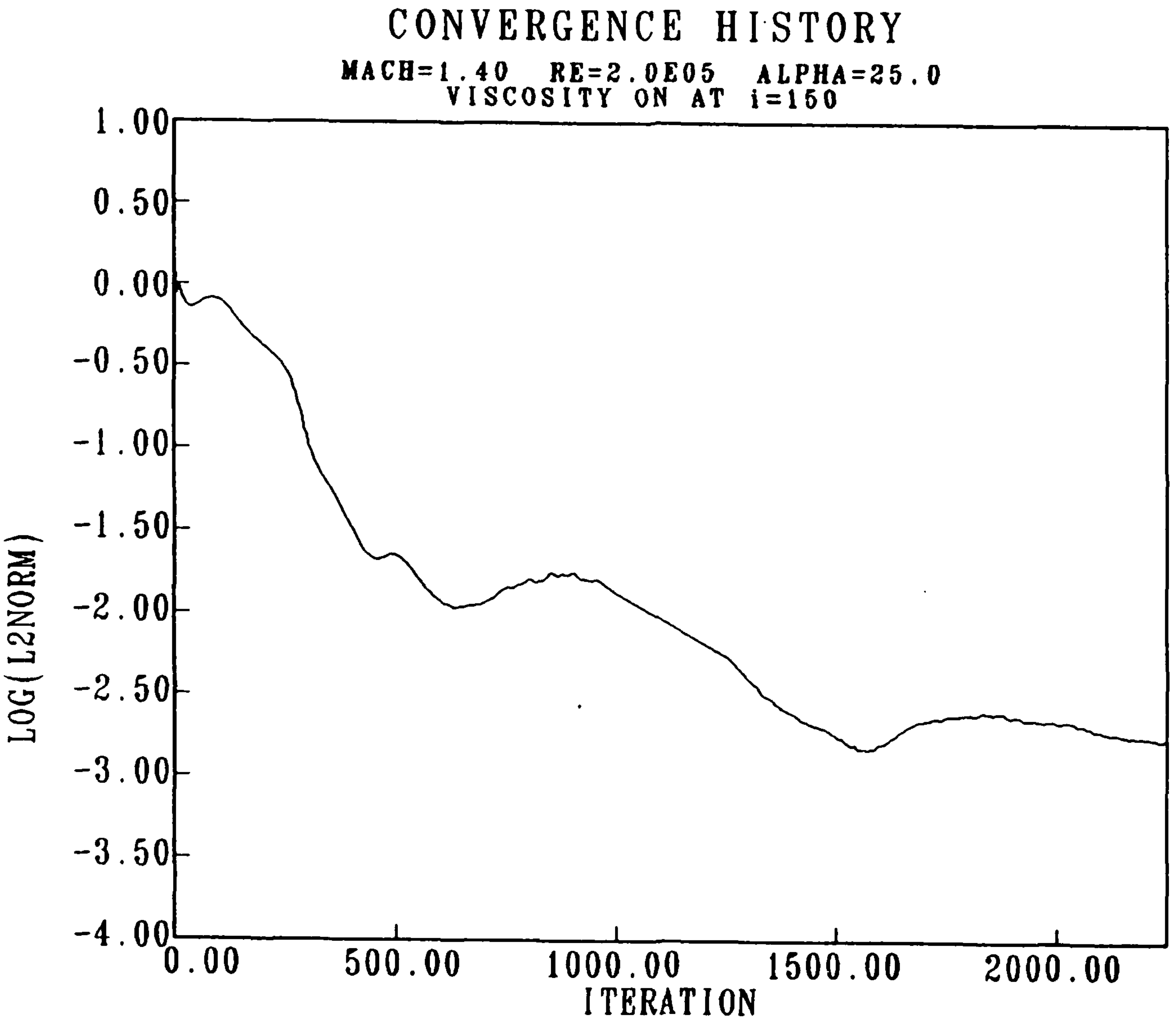

Figure 6. Convergence History - Alpha = 25.0 deg

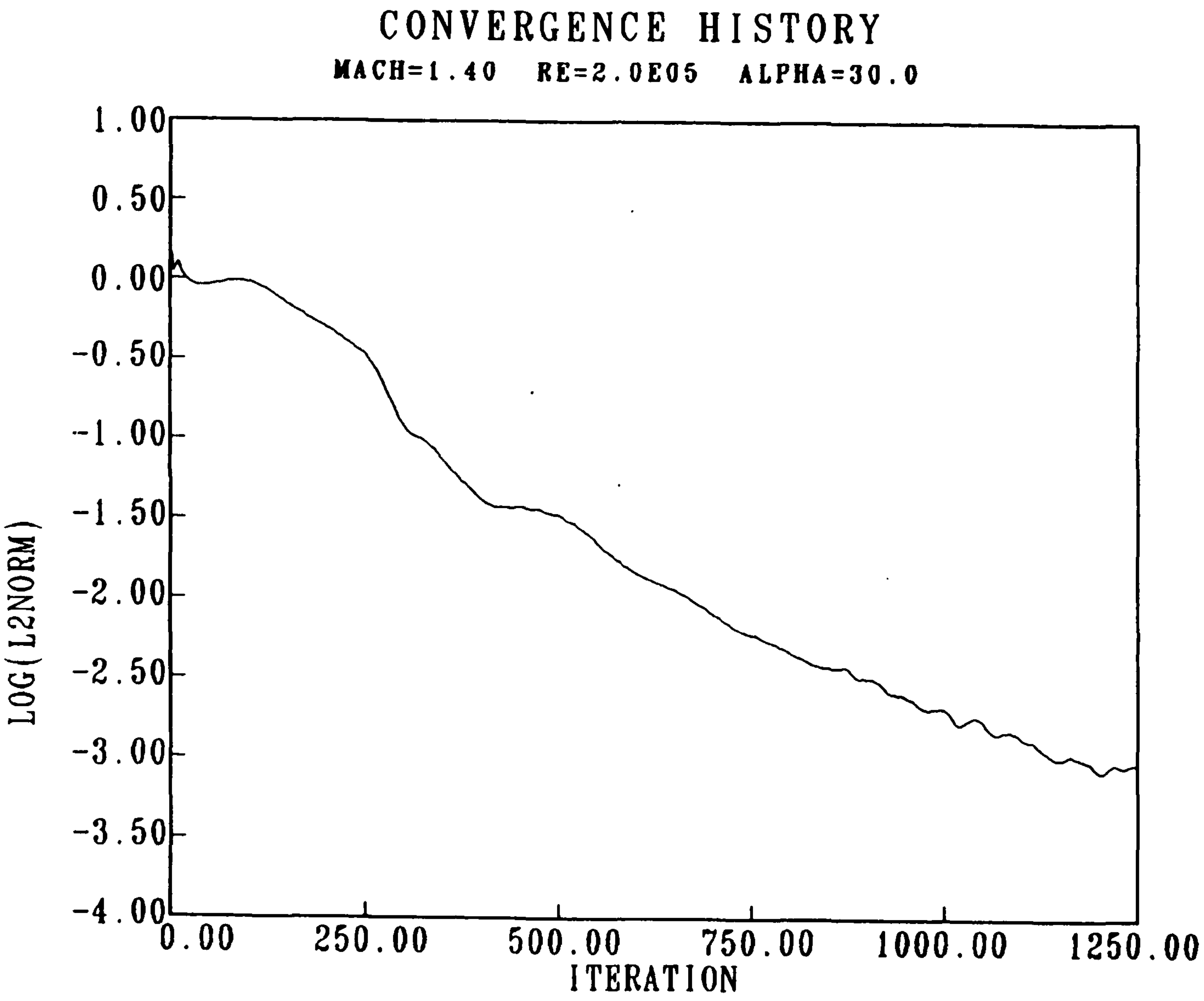

Figure 7. Convergence History - Alpha = 30.0 deg

CHAPTER V

ANALYSIS

Flow solutions are presented for the five caliber tangent ogive configuration at supersonic high angle of attack conditions. The Mach number was 1.4 for all calculations and the angle of attack varied from 25 to 40 degrees. The Reynolds number was 200,000 based on body base diameter. These flight conditions were chosen because of the wide range of asymmetric vortical flow patterns that arise. All calculations were performed assuming laminar flow so as to eliminate any effects a turbulence model may have on the onset and development of asymmetry. Based on Binion and Stanewsky[29], the assumption of laminar flow at this Reynolds number and high angles of attack is a valid one.

In this analysis all streamlines were computed using PLOT3D.[30] This program uses a 2nd order Runge-Kutta integration routine with five integration steps per grid cell. The streamlines on all of the two-dimensional cross-sections of the flow were calculated on a plane one half cell foward of the last constant i grid plane since it is perpendicular to the body longitudinal direction. Since the plane of cell centers is not exactly perpendicular, the longitudinal momentum component was set to zero for plotting purposes. A non-zero momentum term, while using PLOT3D, will give incorrect two-dimensional streamlines if the grid is not perpendicular to the body. These streamline plots are viewed from the upstream direction. Since these streamline calculations involve only two of the three velocity components they are not necessarily projections of the three-dimensional streamlines onto the cross-sectional plane. A particle injected into the flow at a specific location will not neccessarily follow the streamlines given by the two-dimensional calculations. During the analysis, sufficient three-dimensional streamline calculations were performed to insure that the two-dimensional calculations represent true three-dimensional structures. For example, three-dimensional streamlines originating near the nose were traced to the end of the body to insure that the vortex centers are located in the spots indicated by the two-dimensional calculations (Figure 8). Also, the points of attachment and separation as given by the limiting streamlines were compared to the points of attachment and separation suggested by the two-dimensional streamlines (Figure 9).

Figure 10 shows the streamlines at 25 degress. The flow is symmetric at this angle of attack. This two-dimensional streamline calculation is on a cross-section one half cell forward of the back of the body. This location is X/L=97.0%. The flow is dominated by two large, symmetric vortices formed by the separation and roll up of the shear layer. Figures 11 and 12 show the left and right secondary flow regions, respectively. Each secondary flow region contains three nodes, 1 saddle, and four half saddle points. Figure 13 shows the crossflow topology for this case. This is in agreement with equation (7), and thus is a kinematically possible flow.

Figure 14 shows the vortical flow pattern at 30 degrees angle of attack. In this case the flow is dominated by two large, slightly asymmetric vortices. These primary vortices induce a complicated structure of secondary separations, attachments, and vortices. Figure 15

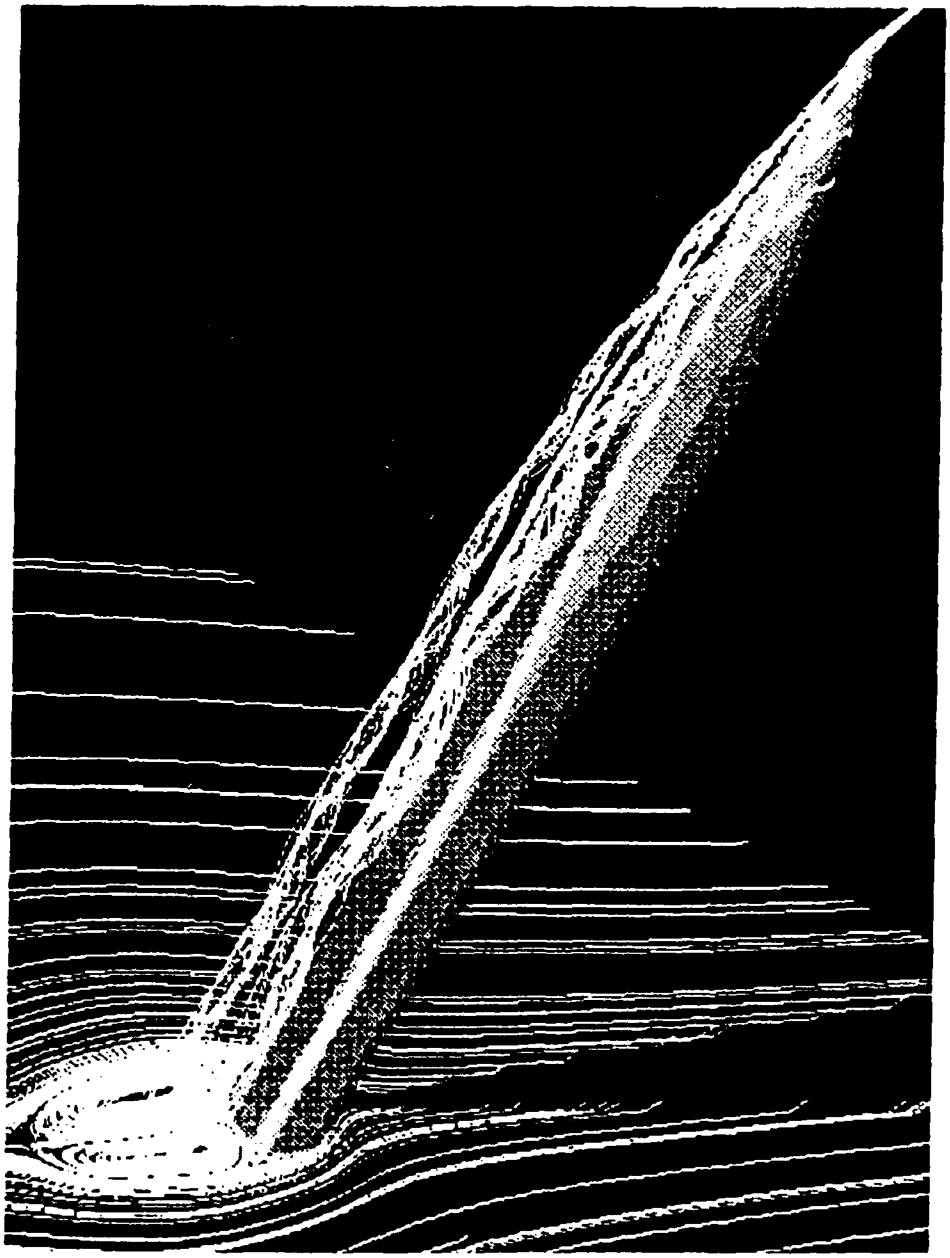

Figure 8. Comparison of Three-Dimensional and Two-Dimensional Streamlines

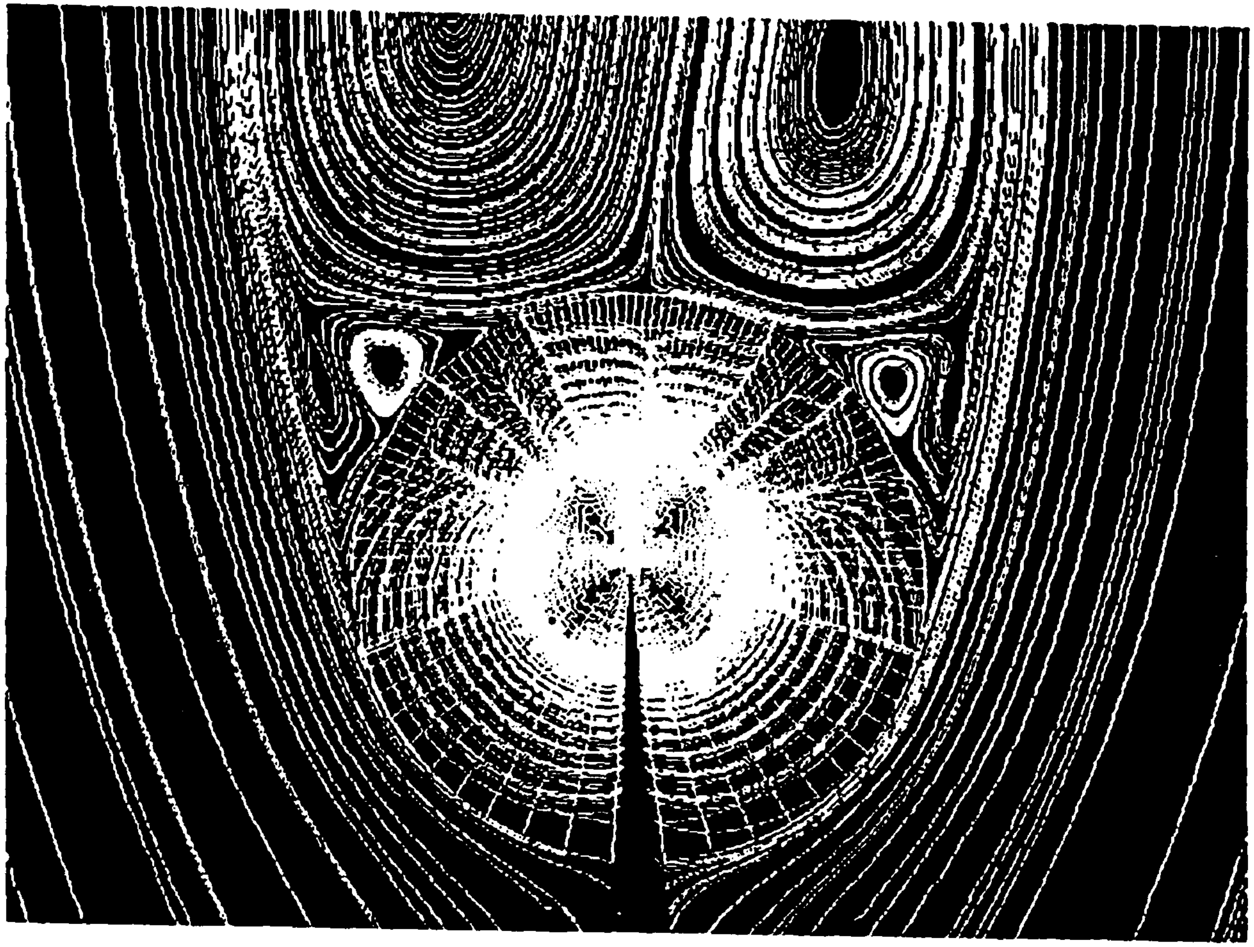

Figure 9. Comparison of Limiting Streamlines and Two-Dimensional Streamlines

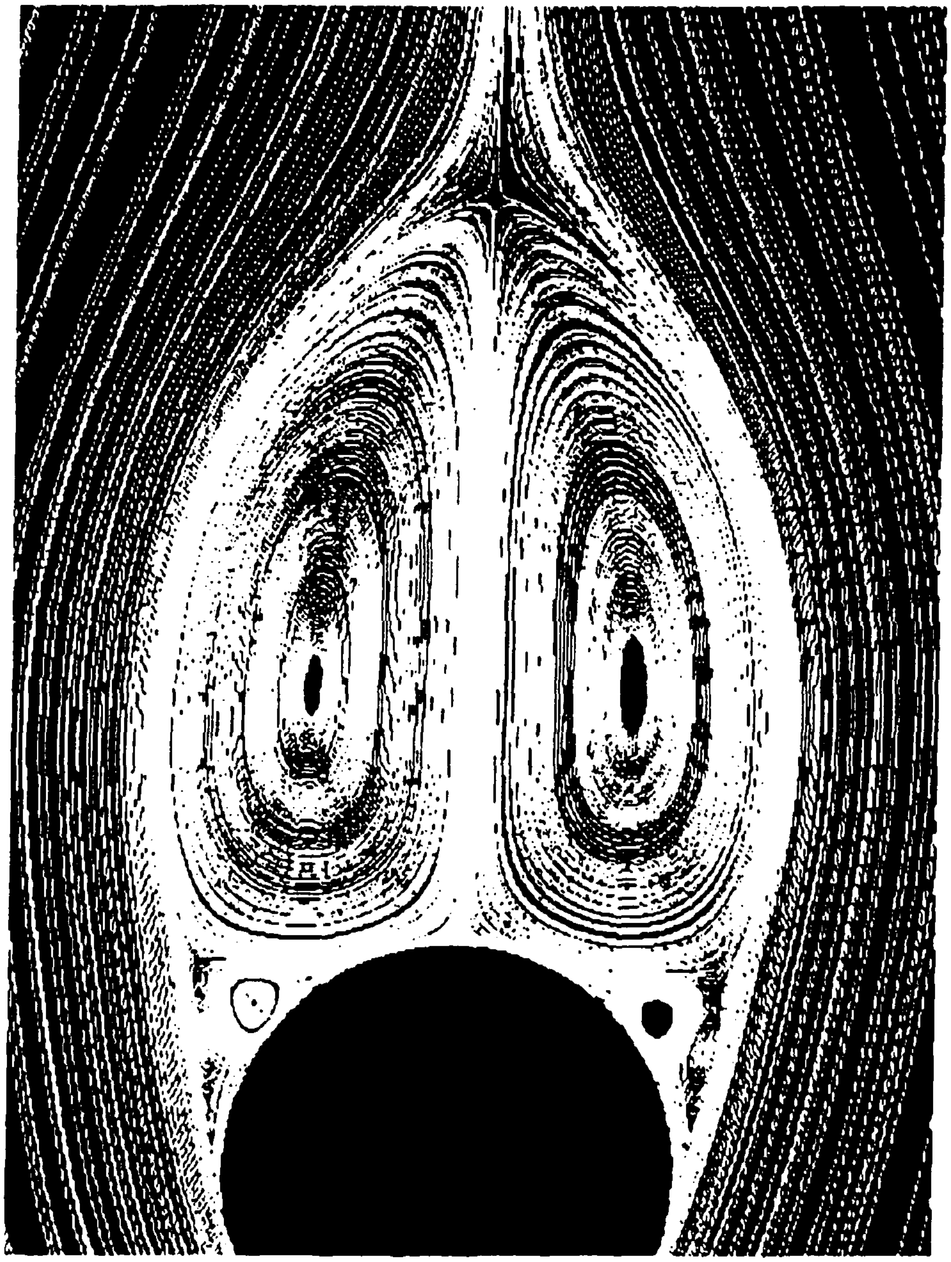

Figure 10. Streamlines - Alpha = 25.0 deg, X/L = 97.0%

Figure 11. Left Secondary Flow Streamlines - Alpha = 25.0 deg, X/L = 97.0%

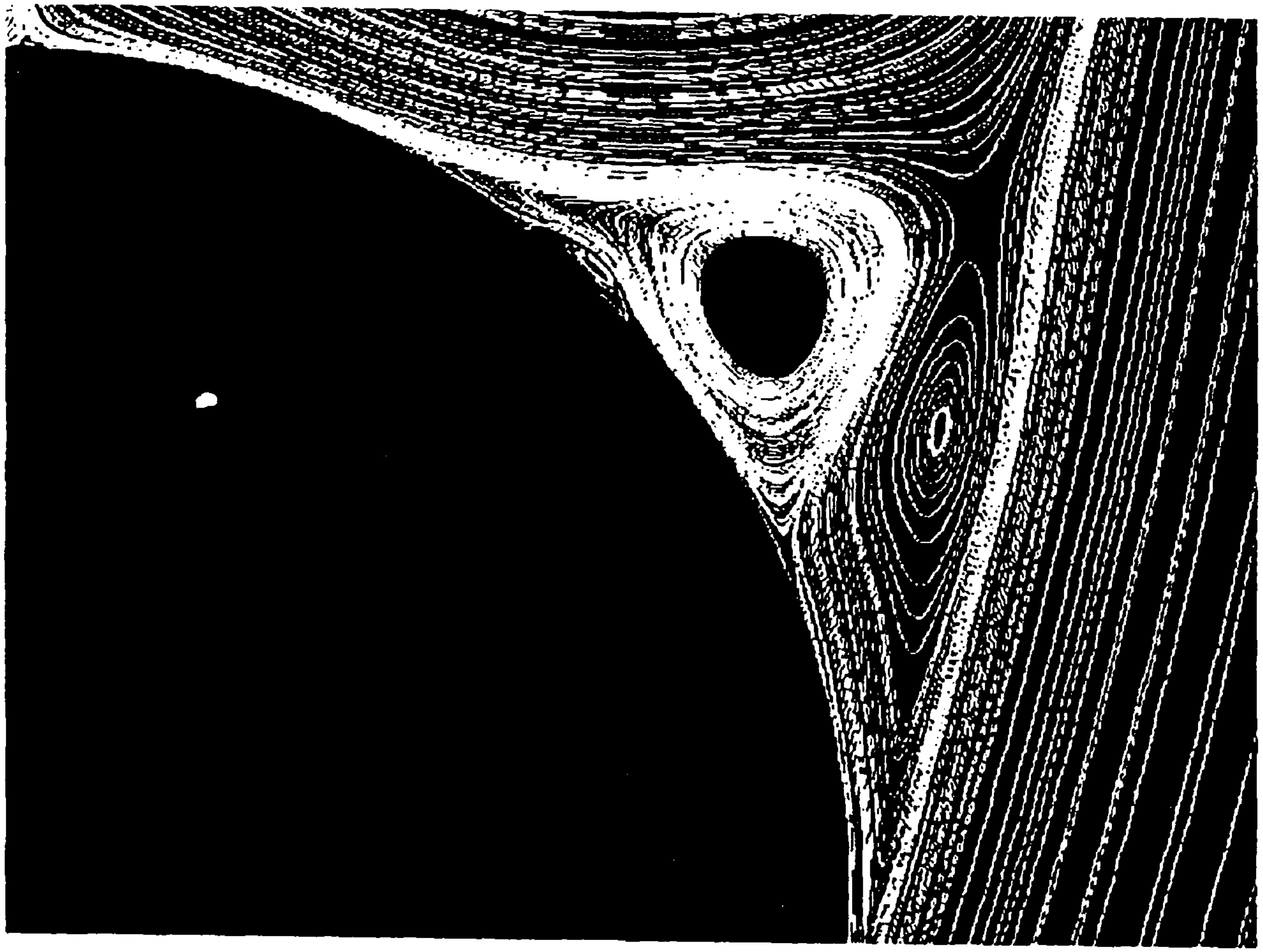

Figure 12. Right Secondary Flow Streamlines -
Alpha = 25.0 deg, X/L = 97.0%

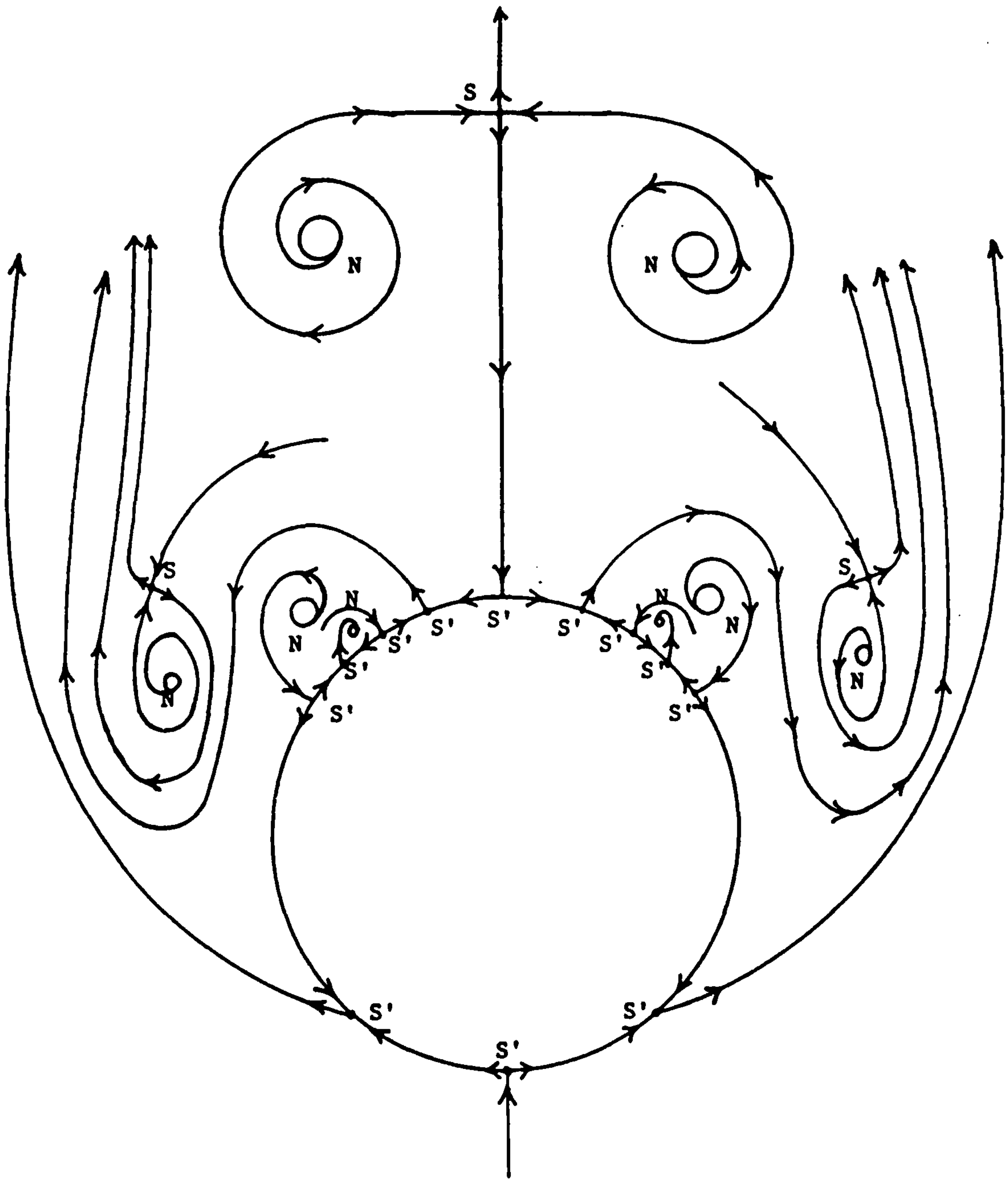

Figure 13. Crossflow Topology - Alpha = 25.0 deg, X/L = 97.0%

Figure 14. Streamlines - Alpha = 30.0 deg, X/L = 97.0%

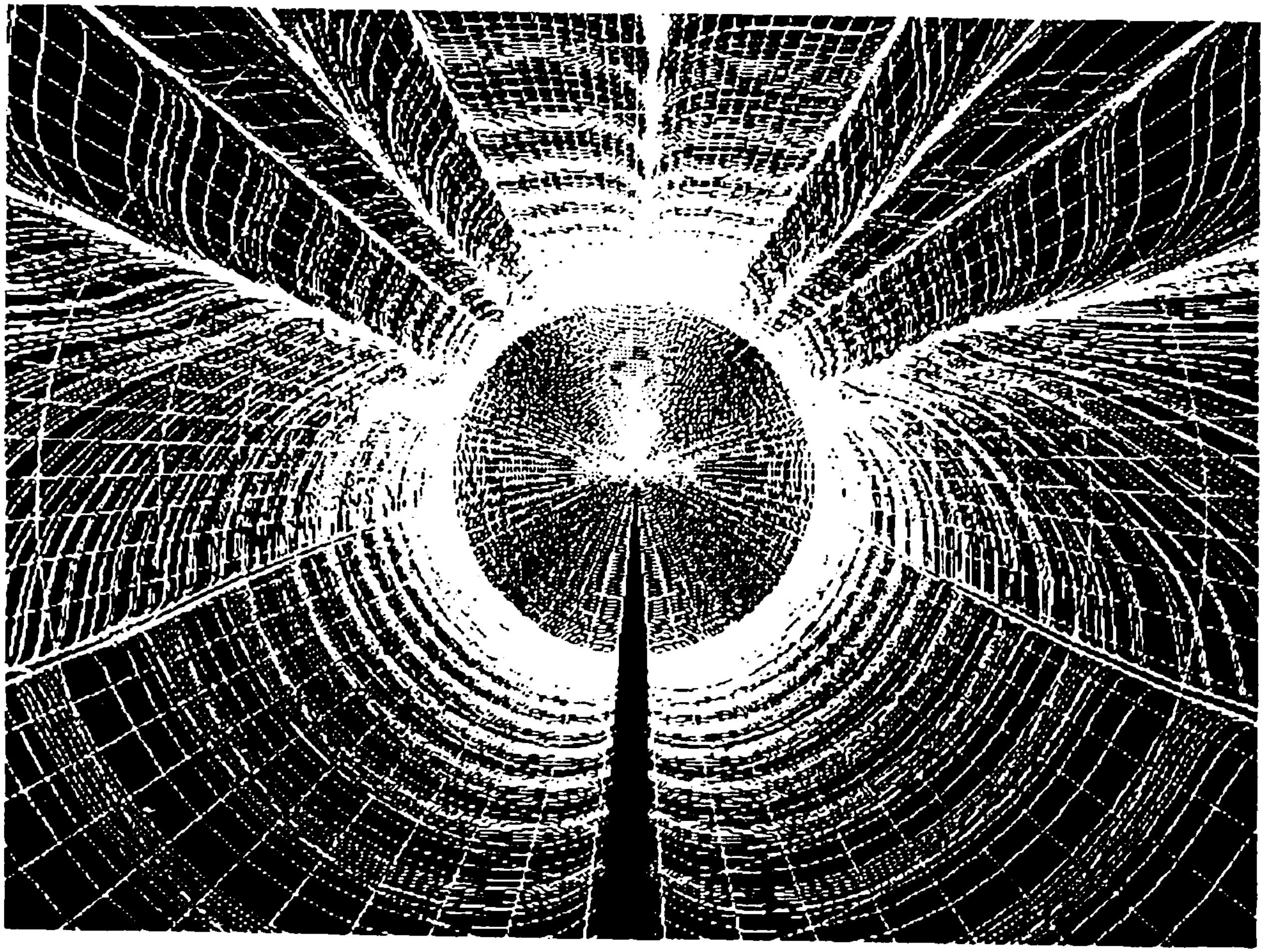

Figure 15. Rear Body Limiting Streamlines - Alpha = 30.0 deg

shows the limiting streamlines plotted on the back portion of the body. The view shown is one in which the observer is at the rear of the body looking down inside the body towards the nose. The first layer of grid points is shown to give a sense of perspective. The blank region at the stagnation point is the block to block connection. There are 12 points of separation and attachment visible. The primary separation nodes at the rear of the body look as if they each consist of two unconnected groups of streamlines. These are connected near the nose as shown in Figure 16 but split apart about a third of the way down the body. They briefly reconnect before splitting a second and final time (Figure 17). Several places were observed where streamlines connect these two lines but these were very few. It is not known whether this is a feature of the flow, the effect of decreasing grid resolution near the rear of the body, or the lack of a sufficient concentration of particle traces generated by the plotting package. Grid resolution appears to be the least likely since the two regions reconnect in a coarser region of the grid than where they first separated. A two-dimensional streamline calculation in a cross-sectional view of this region shows no unusual structure associated with the primary separation line (Figure 18). All of the separation and attachment lines start at the nose (Figure 19).

A detailed streamline calculation of the left secondary separation region is shown in Figure 20. There are three nodes, one saddle, and four half saddle points in this region. The two vortices closest to the body (Figure 21) are associated with separation and reattachment half saddle points, while the remaining vortex is associated with a full saddle point and is separated from the other two vortices by streamlines from the primary vortices. This vortex does not appear to be directly

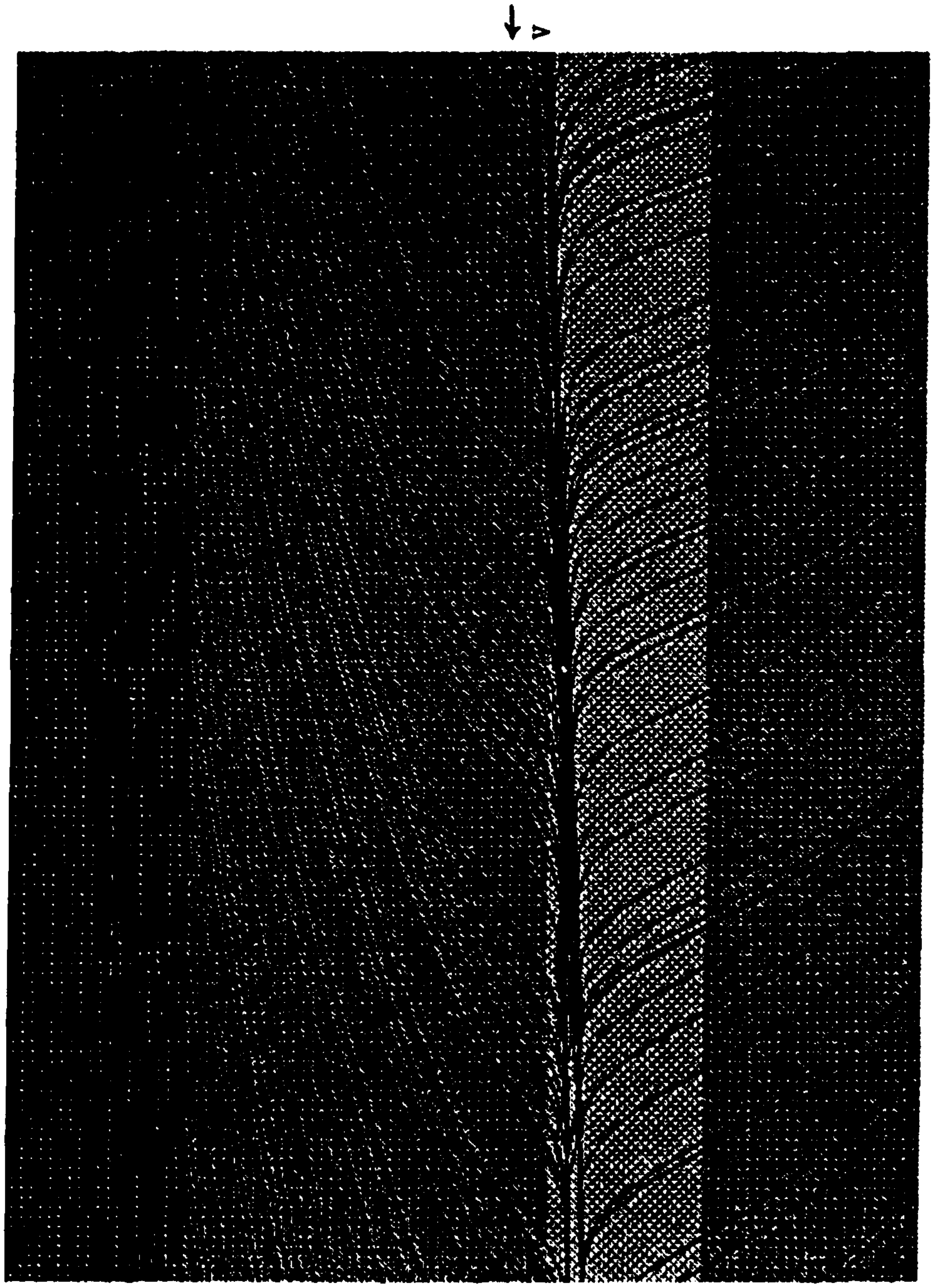

Figure 16. Primary Separation Limiting Streamlines -
Nose Region, Alpha = 30.0 deg

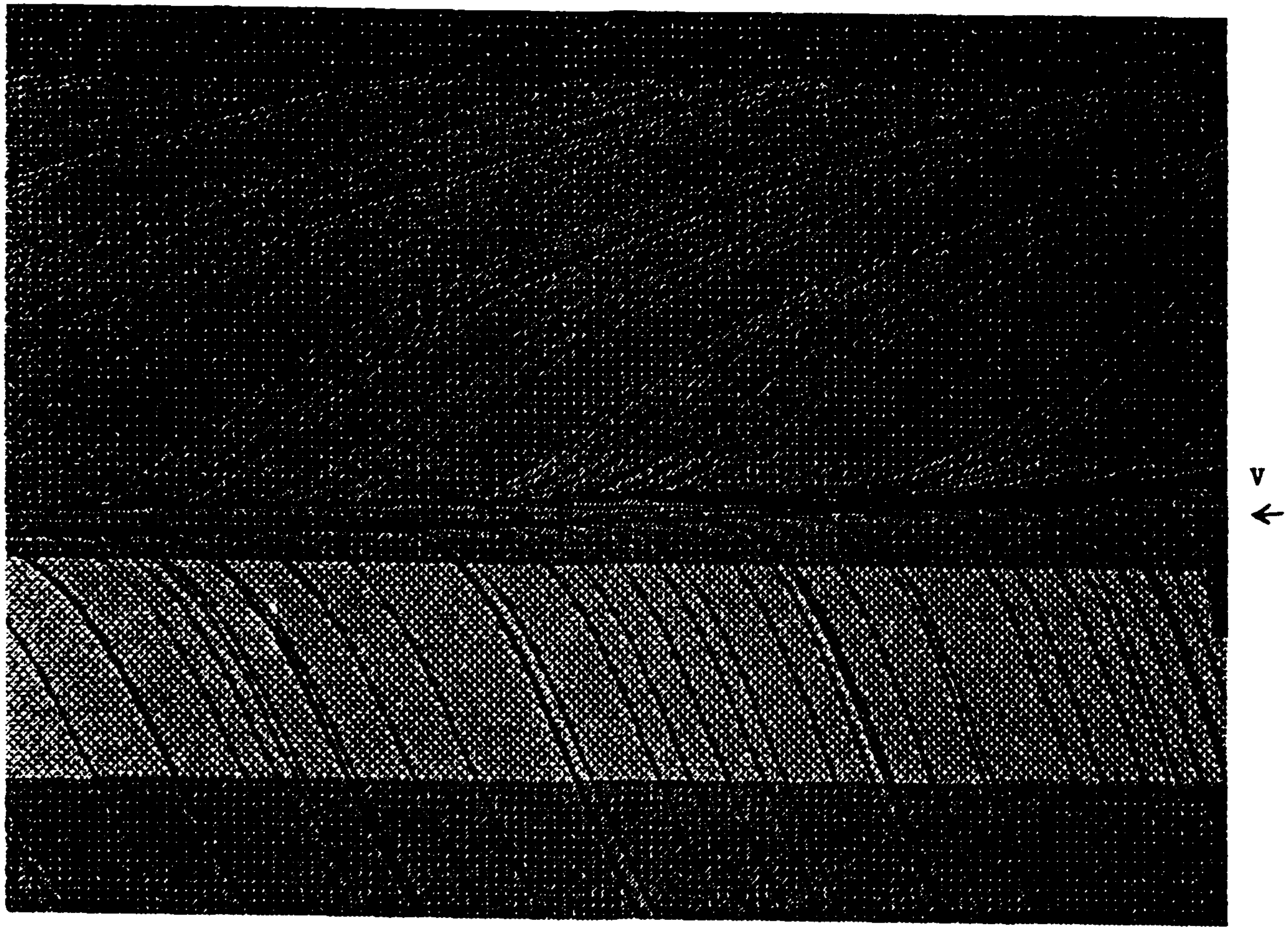

Figure 17   Primary Separation Limiting Streamlines - Mid-Body Region, Alpha = 30.0 deg

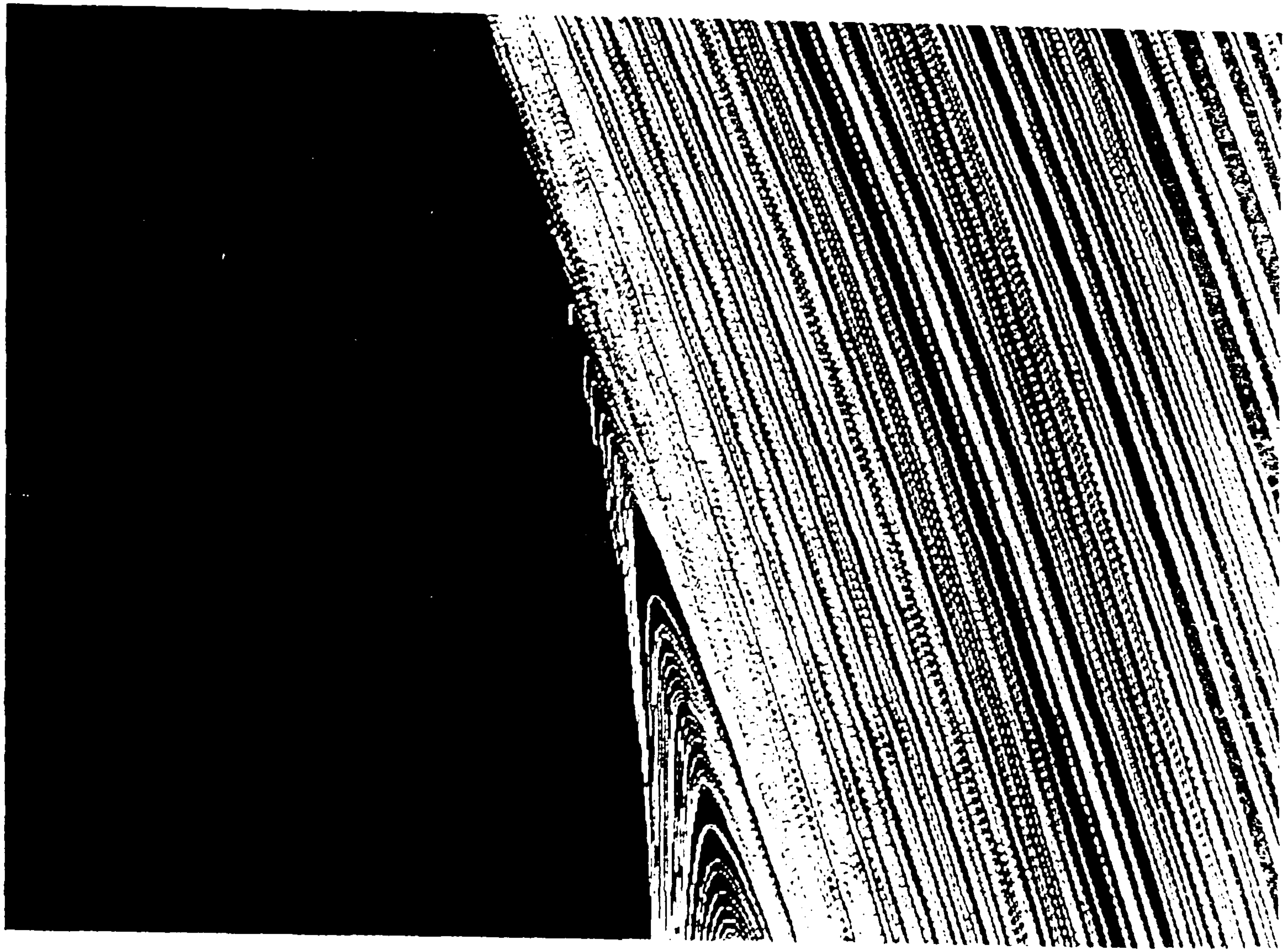

[illegible]

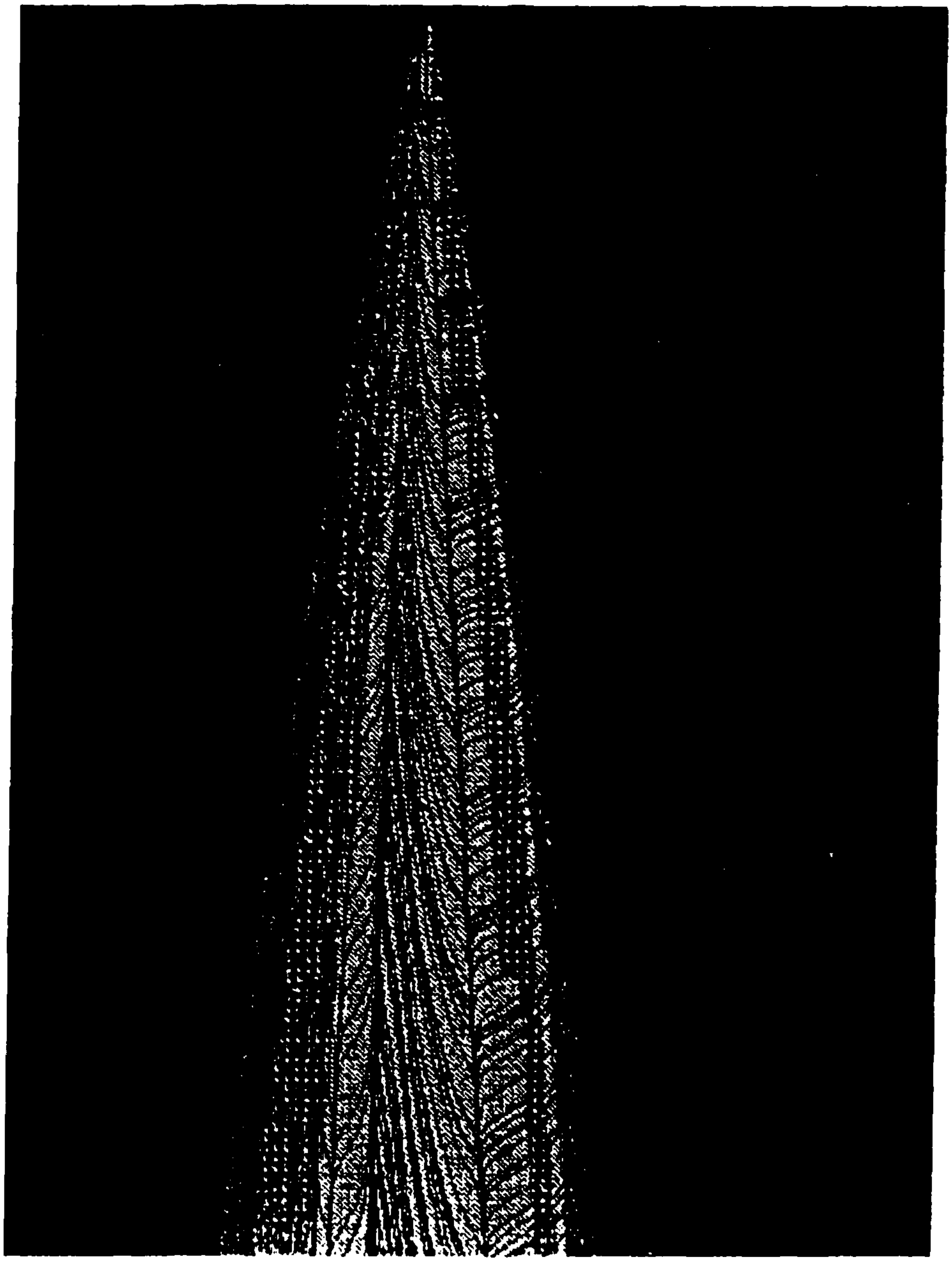

Figure 19. Primary Separation Limiting Streamlines - Body Nose, Alpha = 30.0 deg

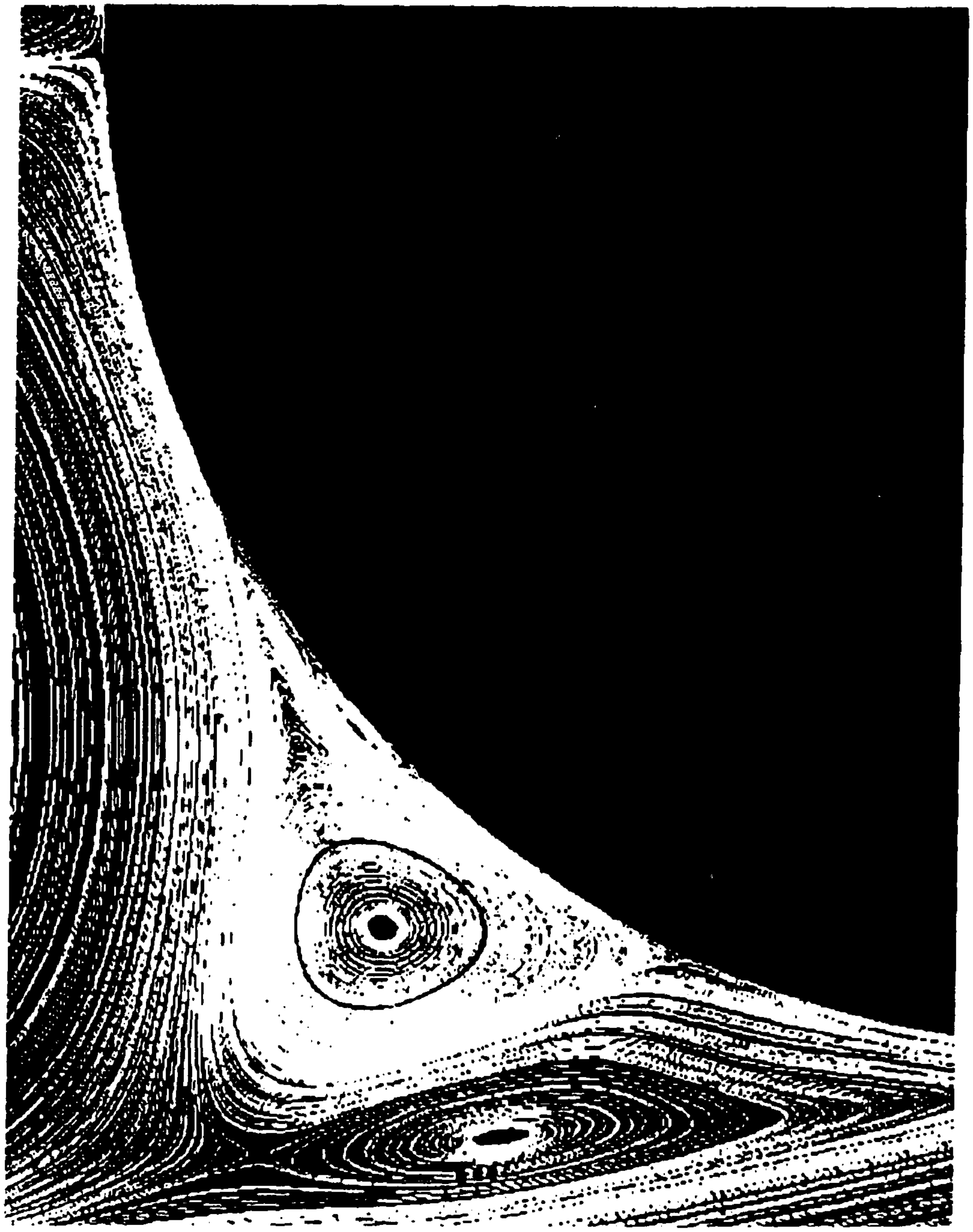

Figure 20. Left Side Secondary Flow Streamlines -
Alpha = 30.0 deg, X/L = 97.0%

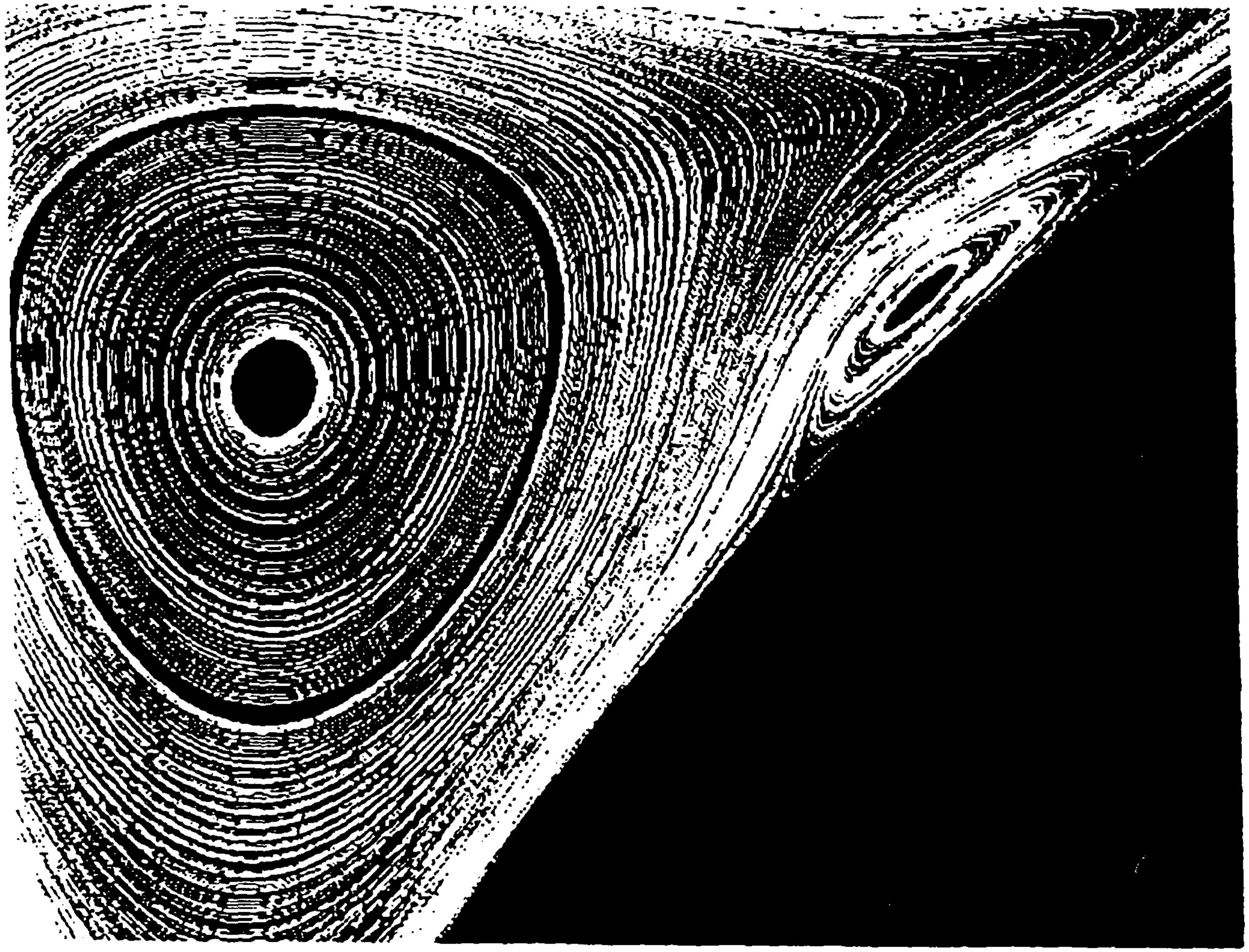

Figure 21. Left Side Secondary Flow Streamlines - Alpha = 30.0 deg, X/L = 97.0%

related to the secondary separations and attachments. Instead, it appears to be formed when the streamlines from the primary vortex are turned from moving towards the windward side to the leeward side by the free stream flow. This secondary flow pattern was observed in experimental two-dimensional cylinder flow by Bouard and Coutanceau[31]. The secondary flow on the other side of the cross-section is similar (Figures 22-24).

There are, in total, 8 foci, 3 saddle points, and 12 half saddle points in the entire cross-sectional plane. In addition to the 16 singular points associated with the secondary separation regions, there are a half saddle at the windward stagnation point, two half saddles corresponding to the primary separations, two foci denoting the primary vortices, a saddle at the top of the primary vortices, and a half saddle where the primary vortices induce attachment at the top of the body (Figure 25). Equation (7) can now be used to test the validity of this topology. Substituting the values of nodal, half nodal, saddle, and half saddle points gives

$$\left(8 + \frac{0}{2} \right) - \left(3 + \frac{12}{2} \right) = -1$$

which is in complete agreement. Therfore, this is a kinematically possible flow structure. The primary structure agrees with that given by Yanta[7] et al. for a tangent ogive configuration in incompressible flow.

The grid refinement study was performed at this angle of attack. Figure 26 shows the two-dimensional streamlines for the coarse grid at the same location as Figure 14 for the fine grid. The basic

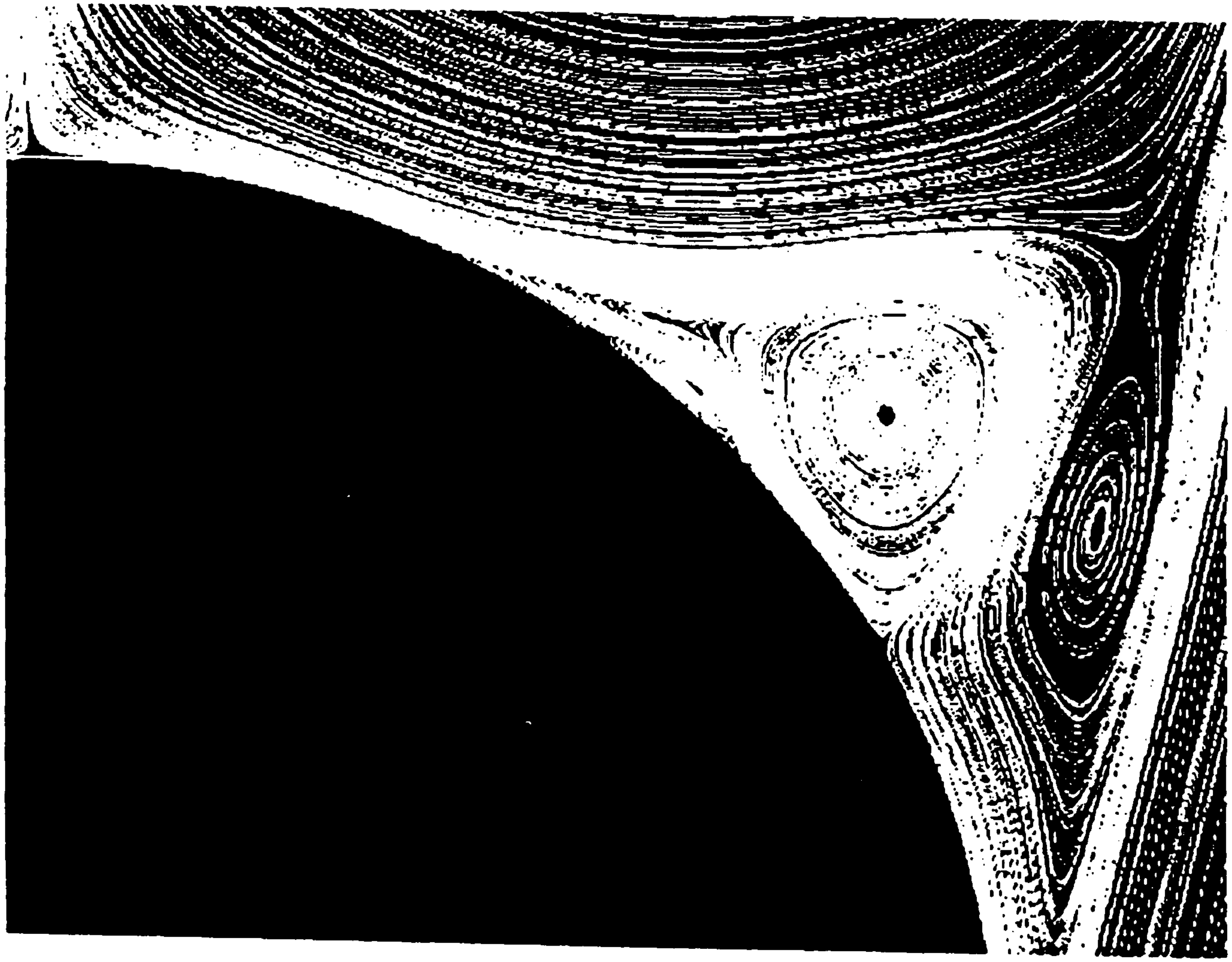

Figure 22. Right Side Secondary Flow Streamlines - Alpha = 30.0 deg, X/L = 97.0%

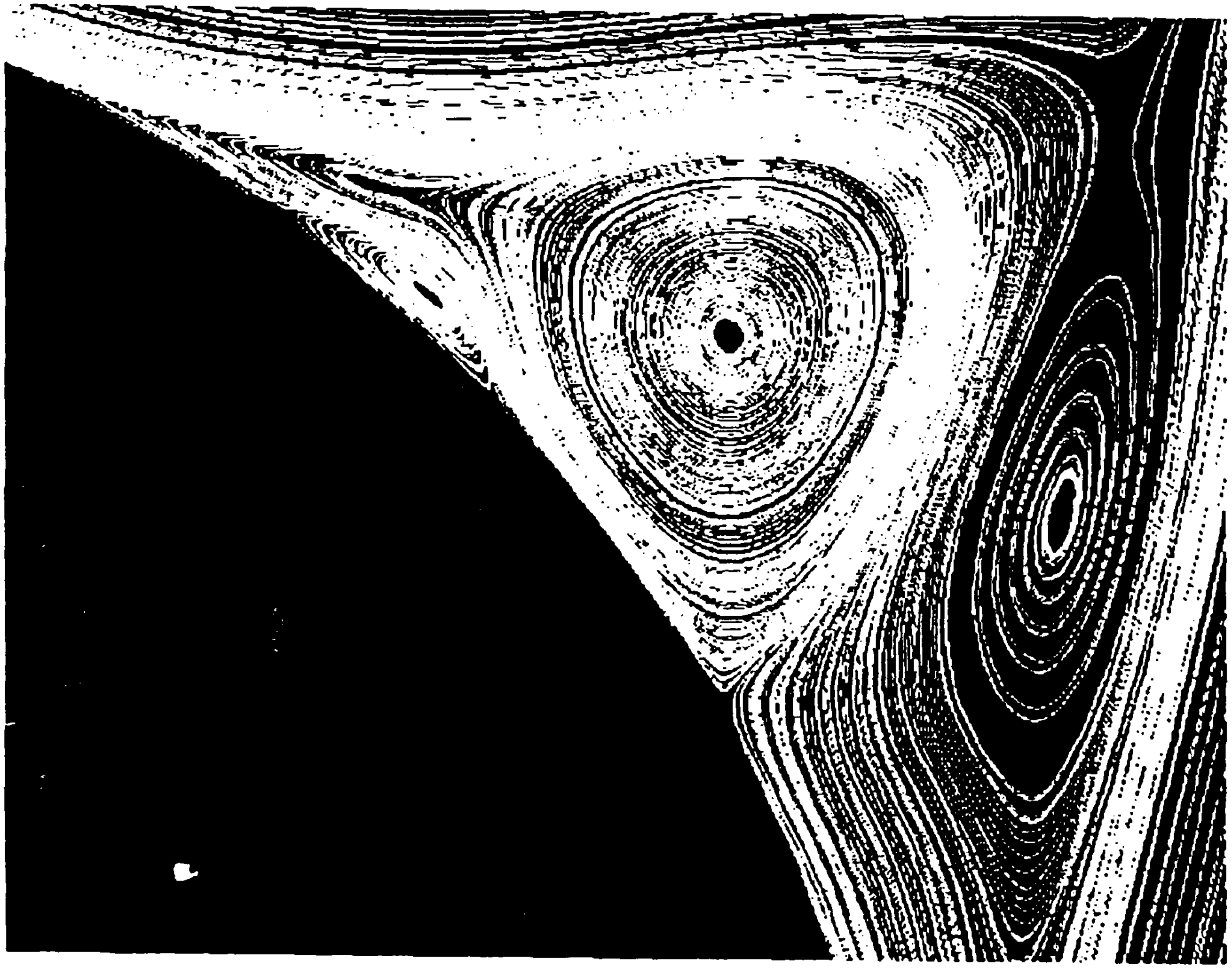

Figure 23. Right Side Secondary Flow Streamlines - Alpha = 30.0 deg, X/L = 97.0%

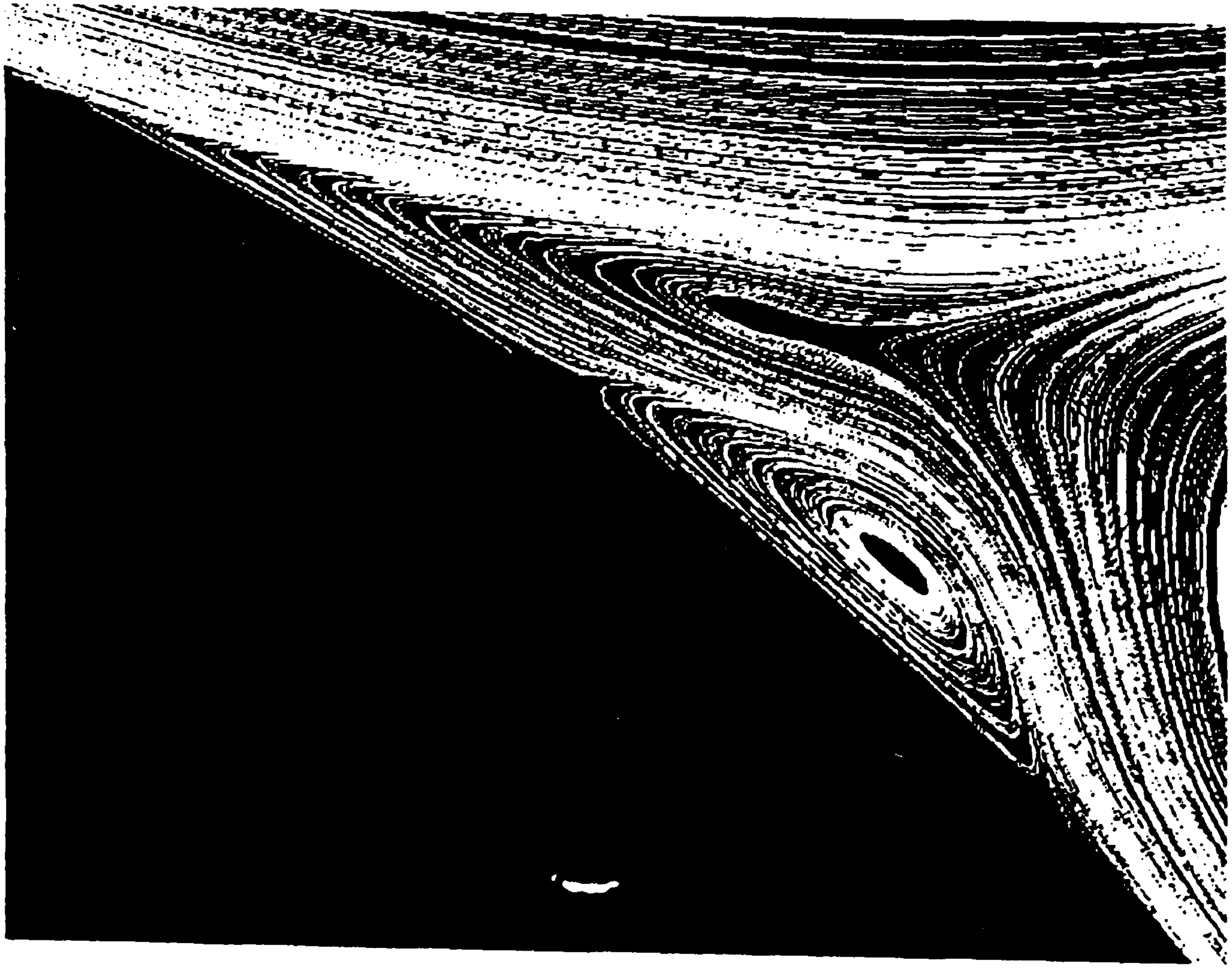

Figure 24. Right Side Secondary Flow Streamlines - Alpha = 30.0 deg, X/L = 97.0%

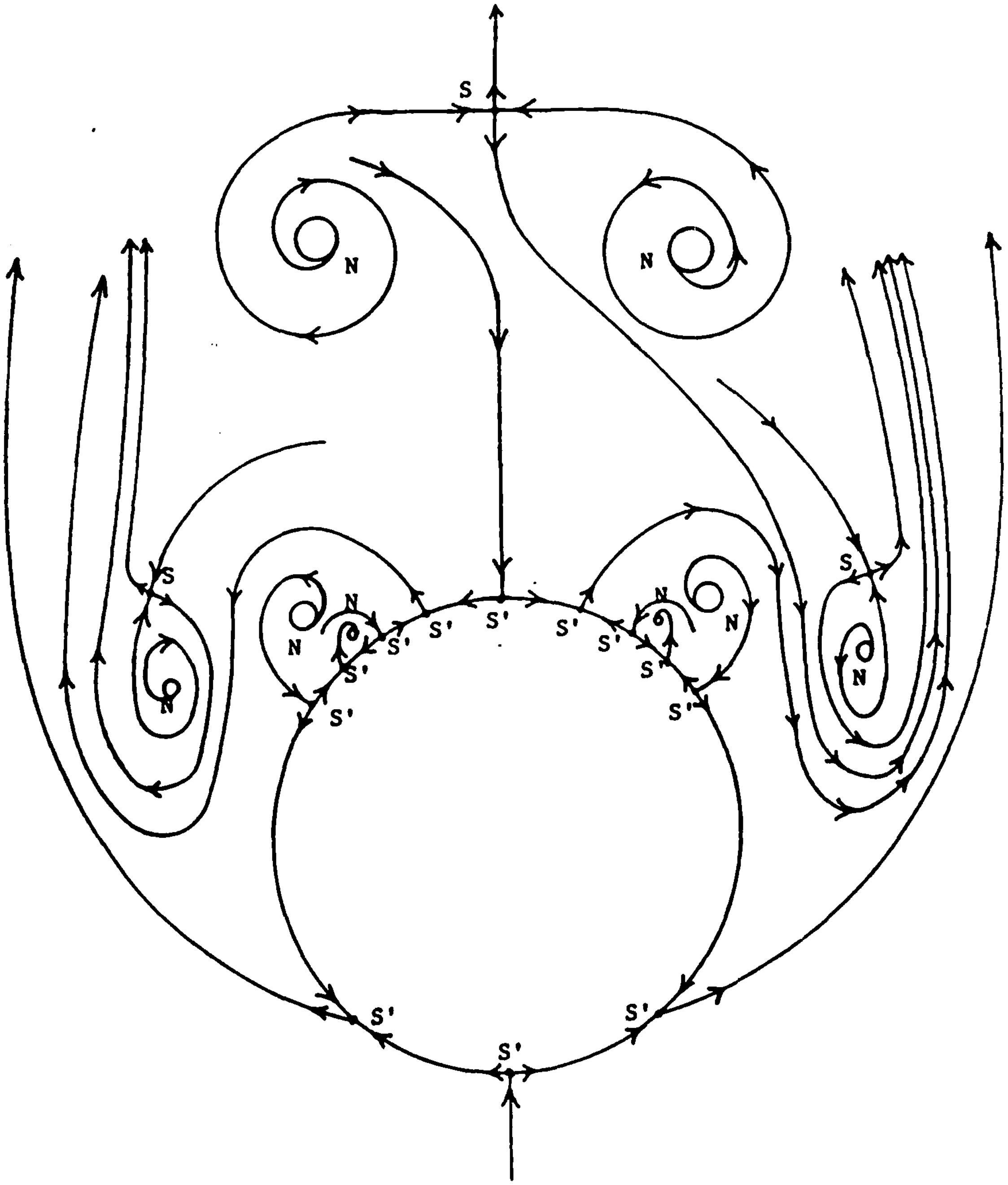

Figure 25. Crossflow Topology - Alpha = 30.0 deg, X/L = 97.0%

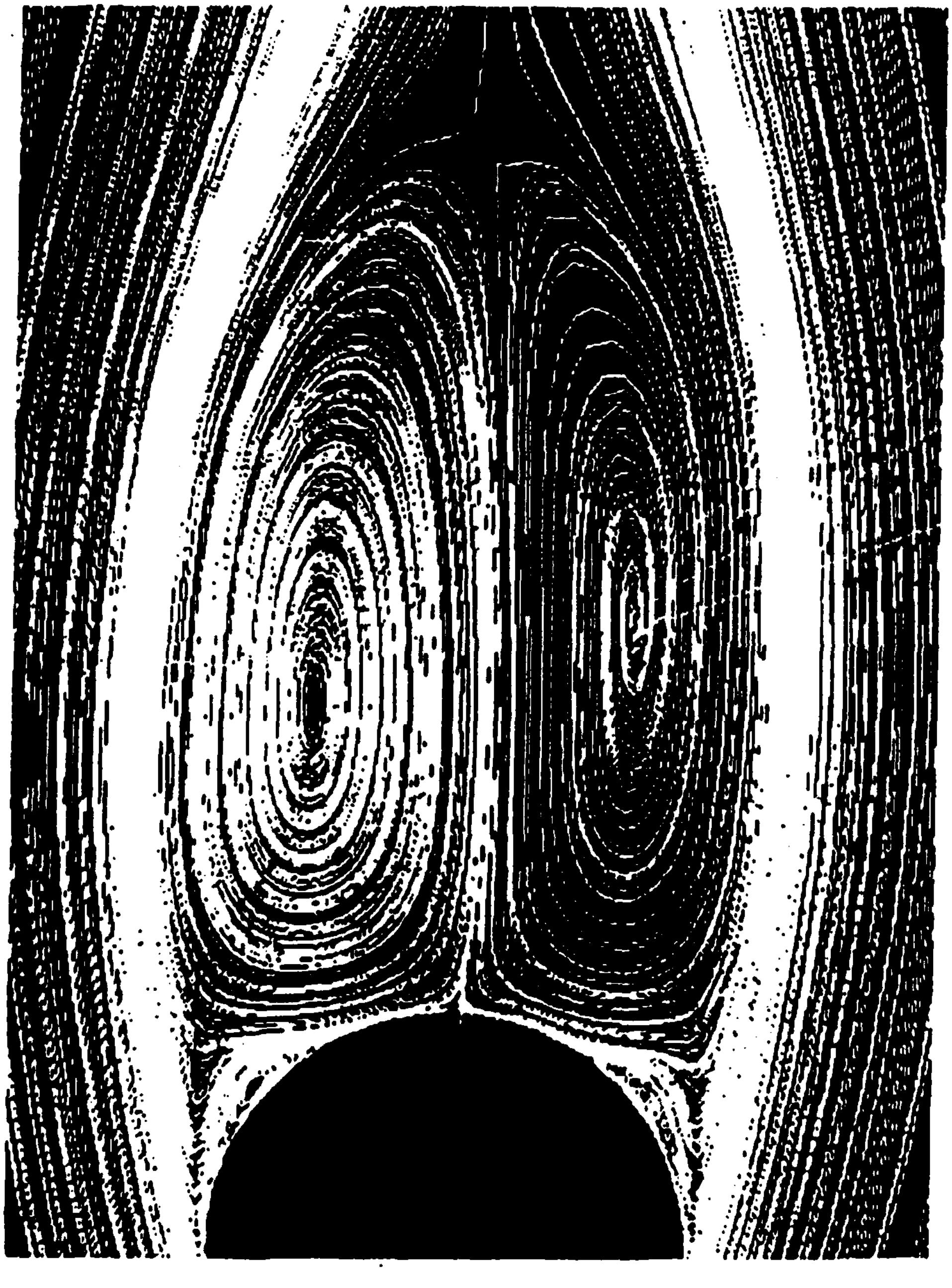

Figure 26. Coarse Grid Streamlines -
Alpha = 30.0 deg, X/L = 97.0%

structure of the primary vortices remained the same. The secondary flow is not the same, but is similar. Much of the detail shown in Figures 20-24 is missing. This is to be expected since the grid resolution was much lower in this region. This may indicate that if the dimensions of the fine grid used was increased substantially, additional singular points might appear. The limiting streamlines are shown in Figure 27.

Figure 28 shows the streamlines, at X/L=97.0%, for an angle of attack of 37.5 degrees. Calculations were not done to see how the structure changed between 30 degrees (Figure 14) and 37.5 degrees. With such a large gap in angle of attack it is possible that the flow structure passed through some intermediate step rather than the change portrayed by just looking at the two cases 7.5 degrees apart. Comparing 30 degrees (Figure 14) and 37.5 degrees (Figure 28), one primary vortex has moved above the other one and is very irregular in shape. The center of this vortex is located approximately two body diameters away from the body. Figure 29 shows the three-dimensional streamlines that form this vortex. The other vortex is much closer to the body than in the 30 degree case. Figure 30 shows an enlargement of the left secondary flow region. A new node and saddle combination has appeared within one of the previous secondary flow vortices. This new, and very small vortex, appeared when a portion of the vortex containing it flattened and pinched off (Figure 31). The right side (Figure 32) retains the same stucture as the 30 degree case (Figure 22). Except for the left secondary flow region and asymmetric primary vortices, the 37.5 case is very similar to the 30 degree case in terms of location and types of singular points. With the addition of a new foci and saddle, compared to the 30 degrees (Figure 25), the summation equation is still satisfied. Figure 33 shows

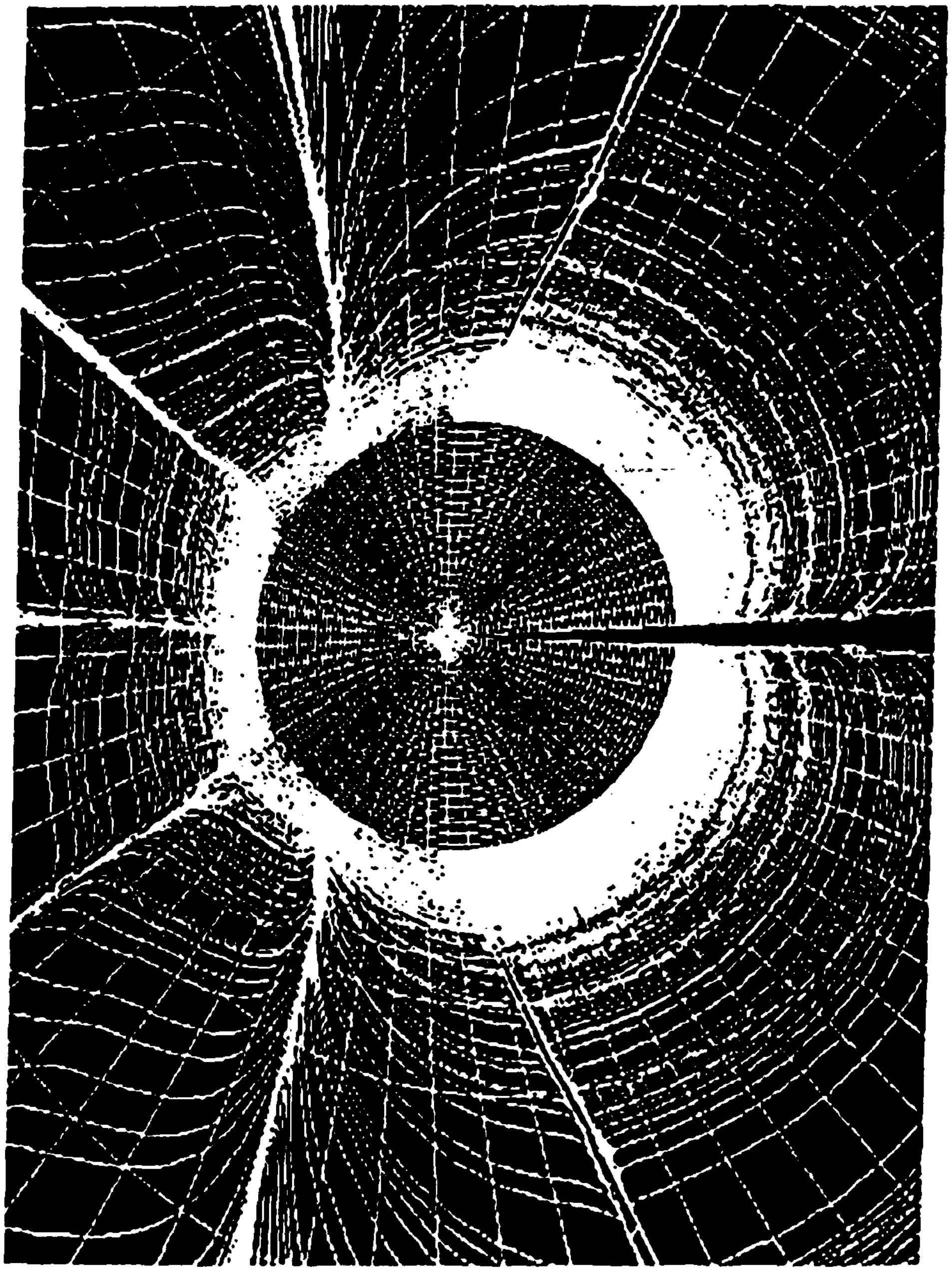

Figure 27. Coarse Grid Rear Body Limiting Streamlines -
Alpha = 30.0 deg, X/L = 97.0%

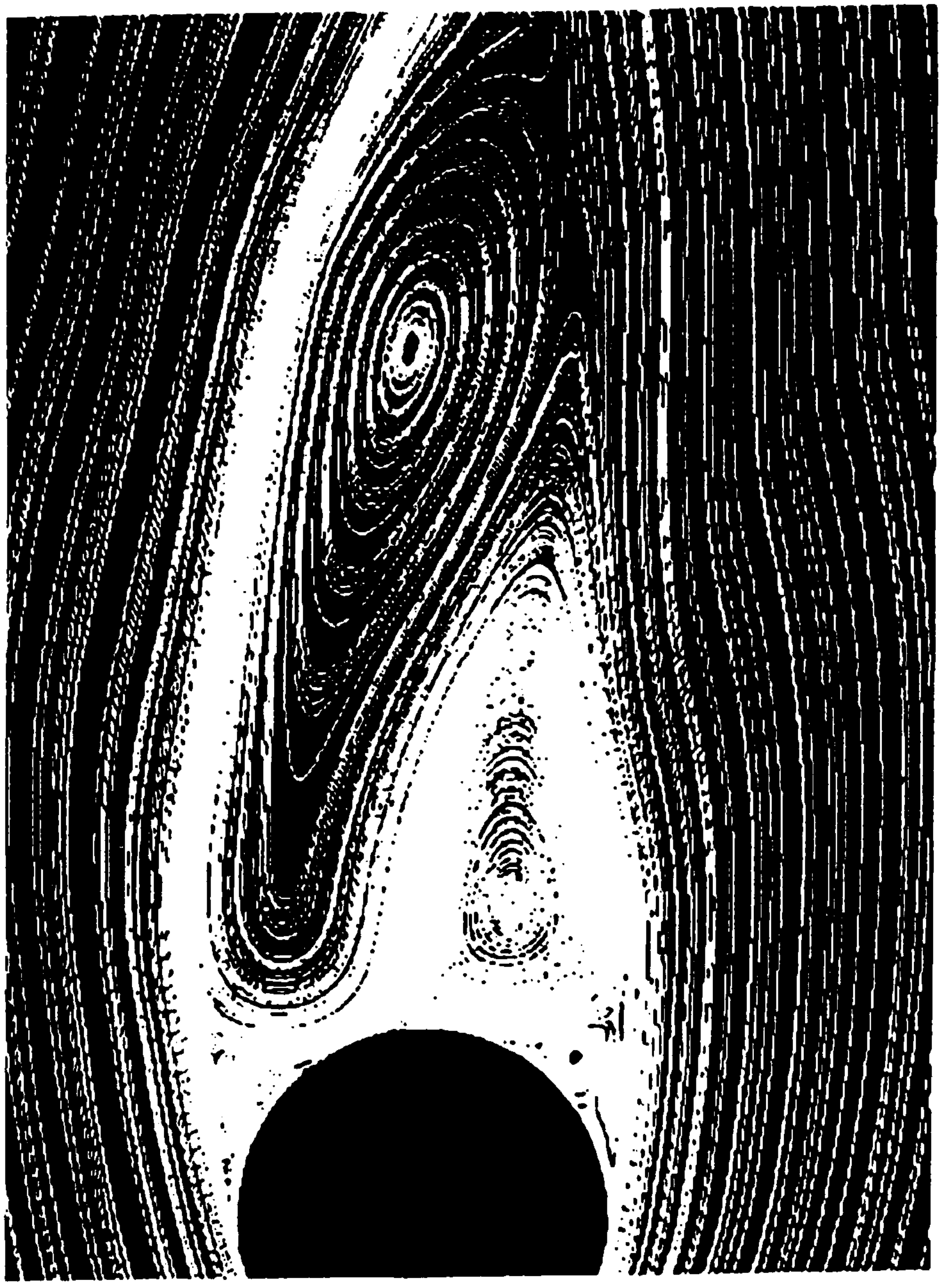

Figure 28. Streamlines - Alpha = 37.5 deg, X/L = 97.0%

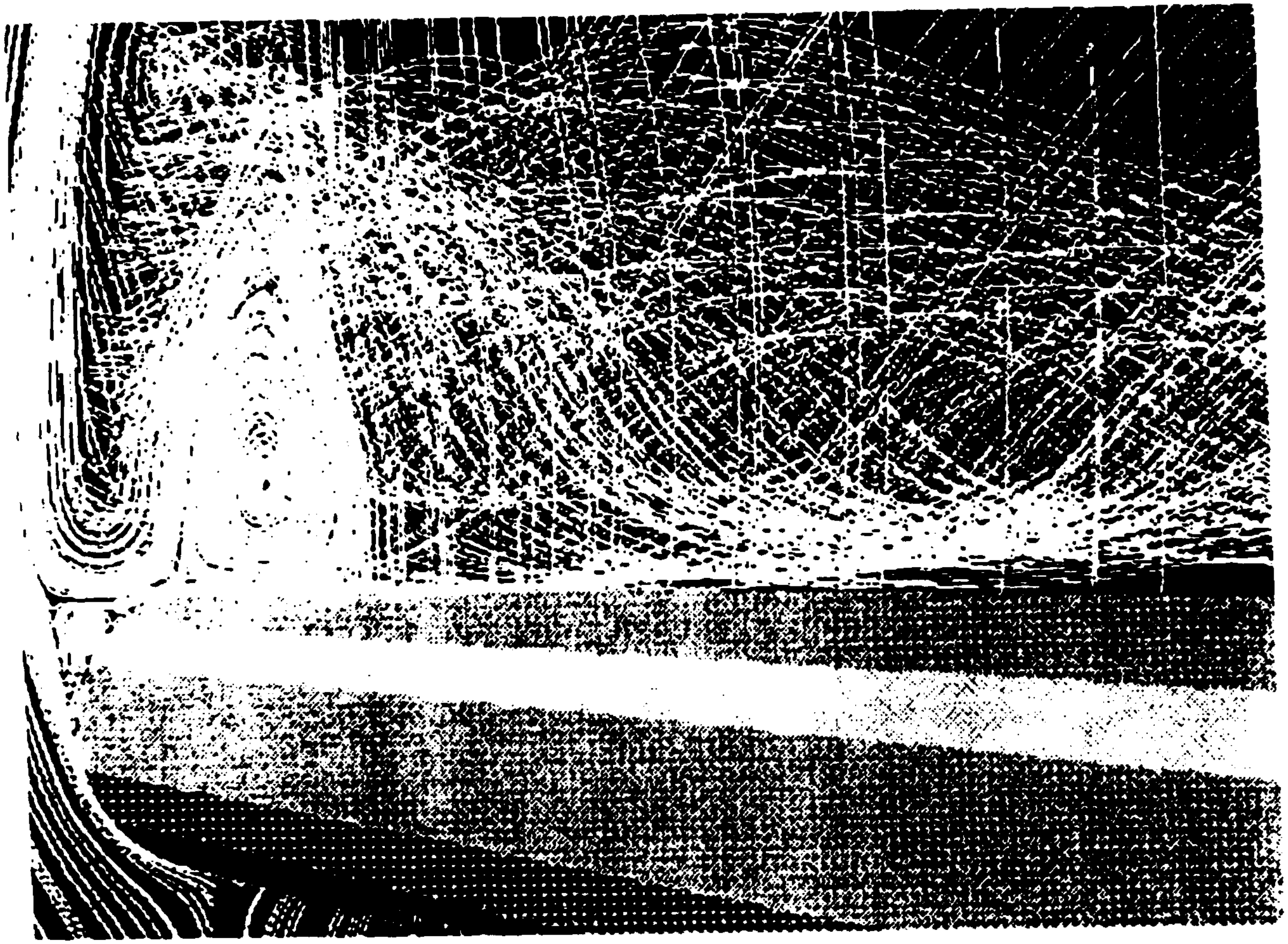

Figure 29. Three-Dimensional Streamlines of Left Vortex - Alpha = 37.5 deg, X/L = 97.0%

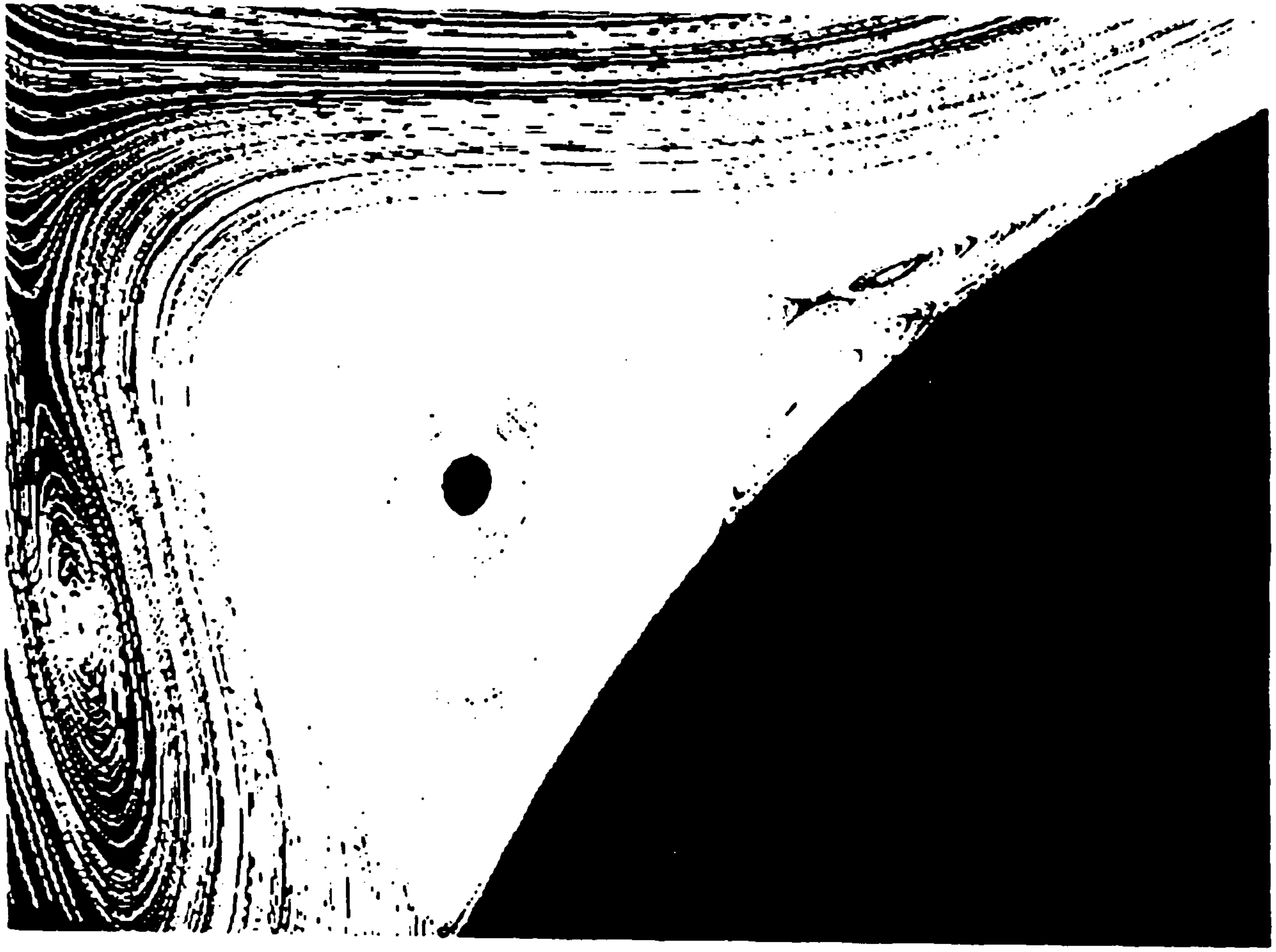

Figure 30. Left Side Secondary Flow Streamlines - Alpha = 37.5 deg, X/L = 97.0%

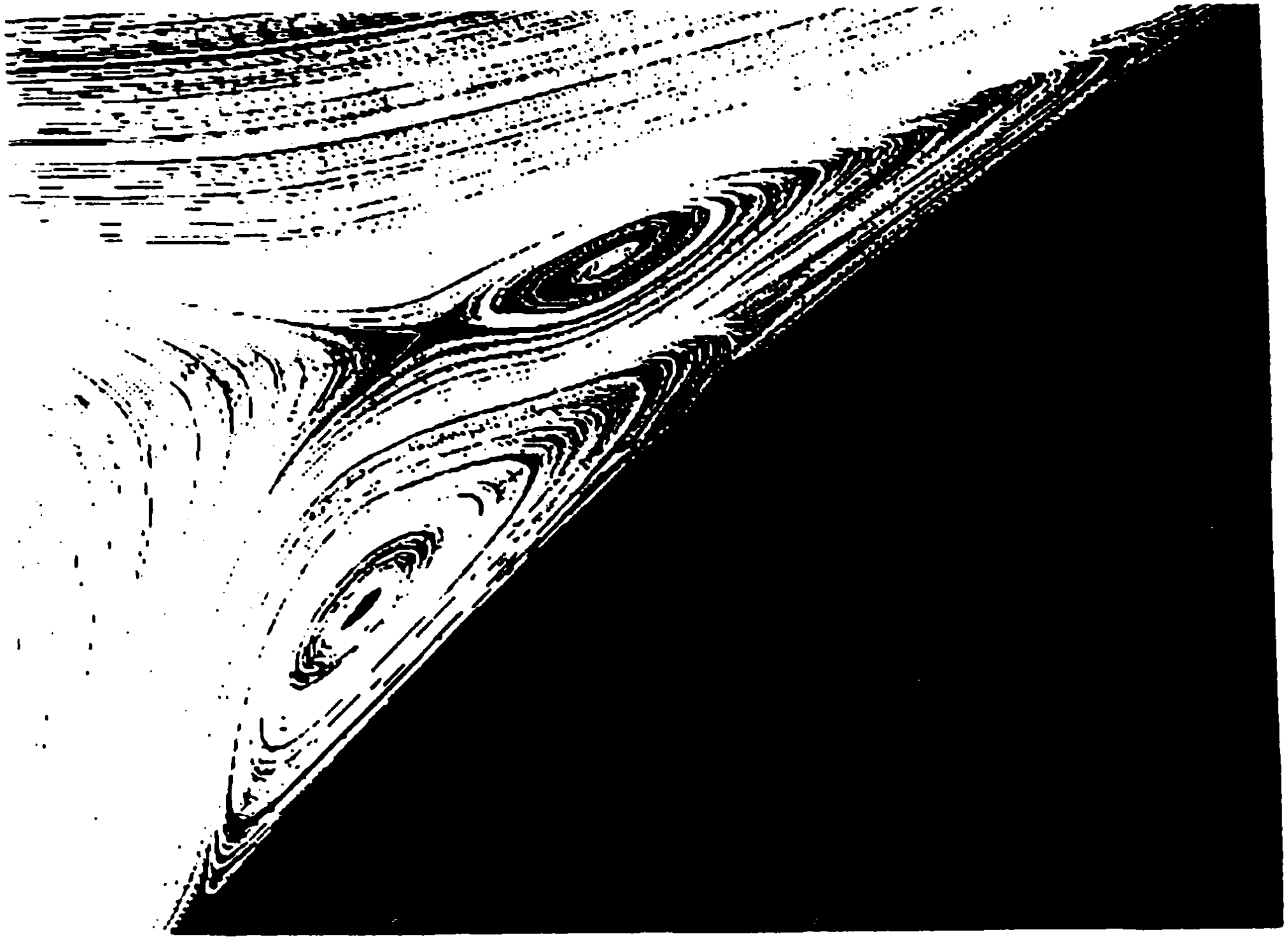

Figure 31. Left Side Secondary Flow Streamlines -
Alpha = 37.5 deg, X/L = 97.0%

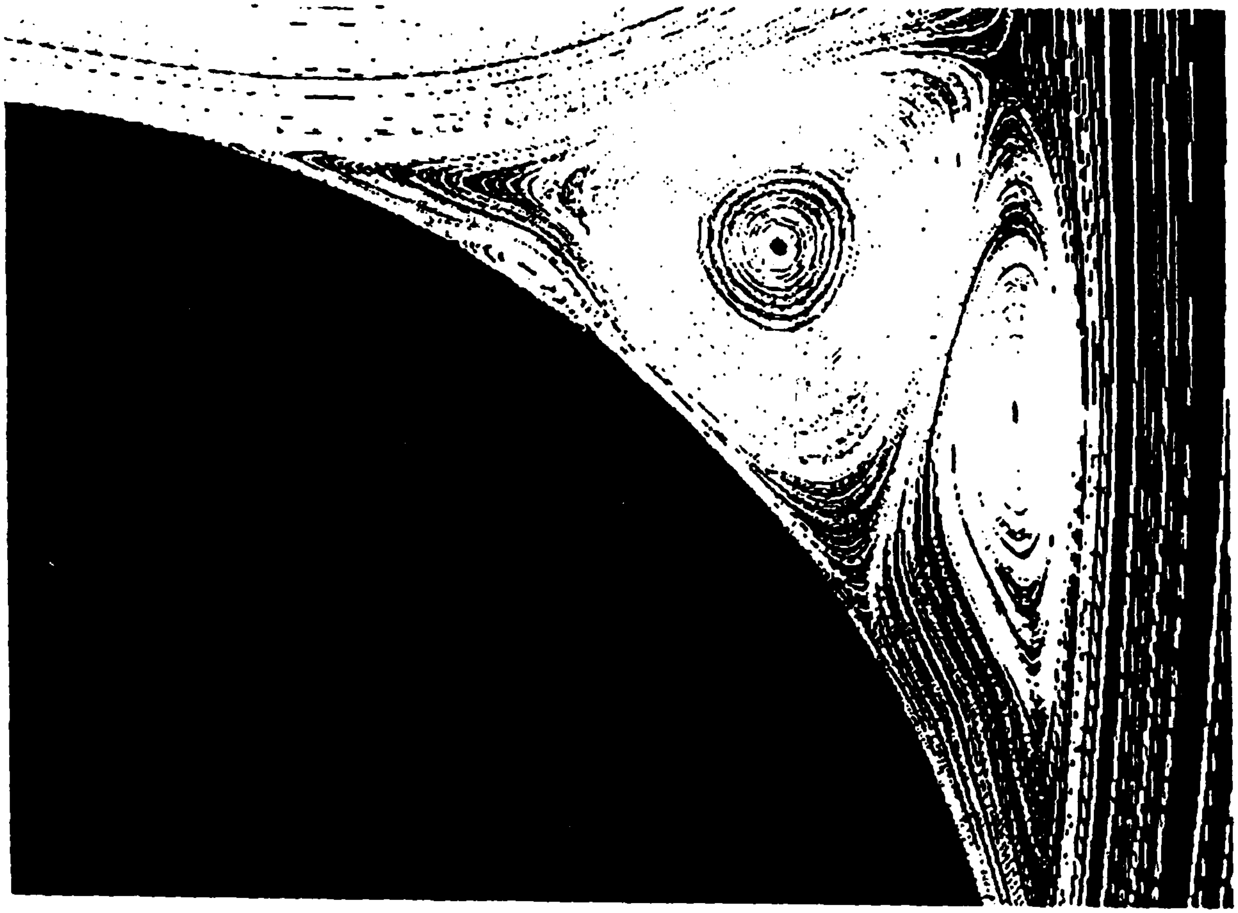

Figure 32. Right Side Secondary Flow Streamlines - Alpha = 37.5 deg, X/L = 97.0%

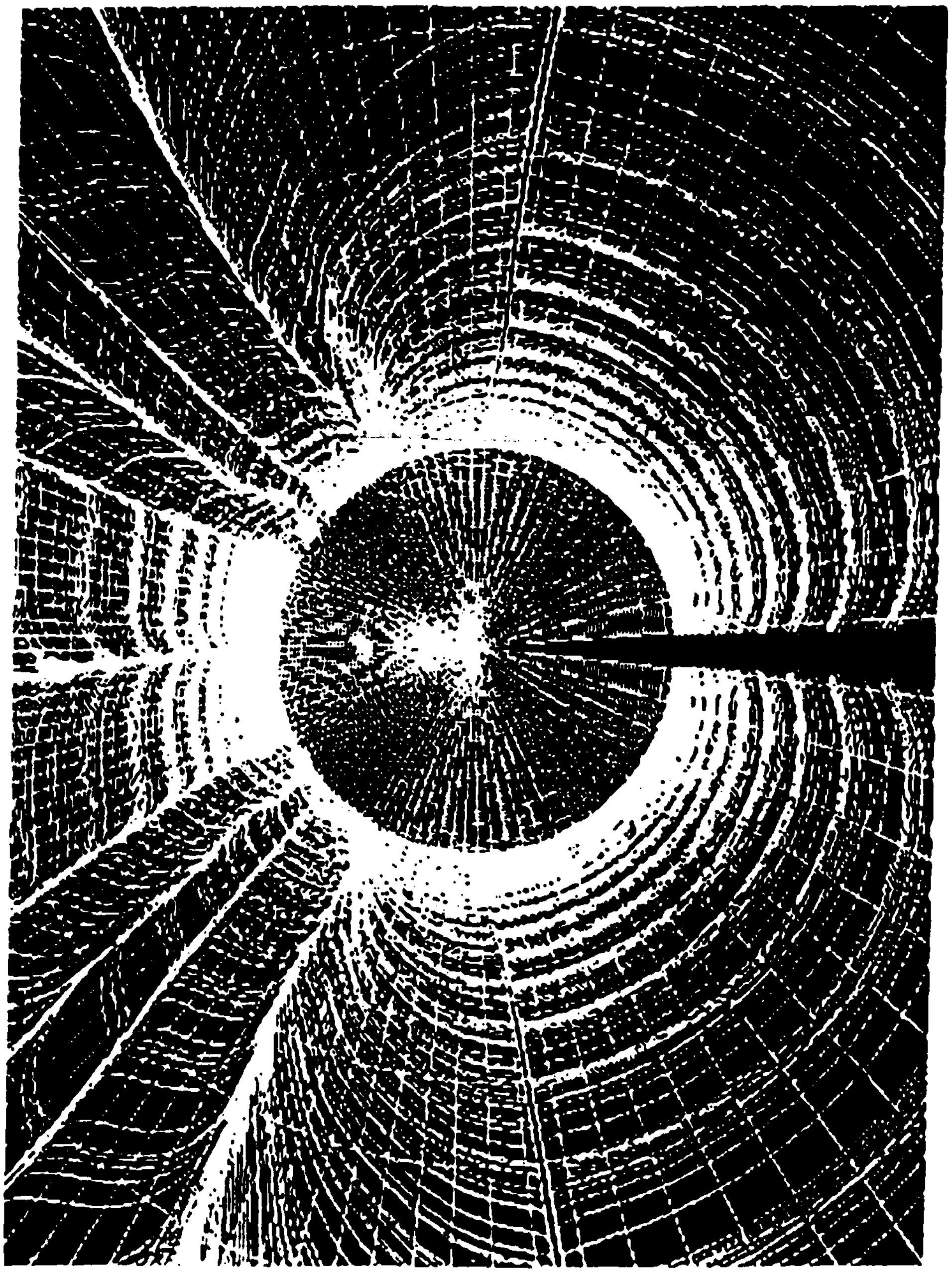

Figure 33. Rear Body Limiting Streamlines - Alpha = 37.5 deg

the limiting streamlines on the back portion of the body for the 37.5 degree case. The overall pattern is the same as the 30 degree case (Figure 15) although some skewness can be seen. The attachment node resulting from the primary vortices is offset to the left of the body center line. The other nodes are slightly asymmetric as well.

Figures 34-36 show the density contours at three axial locations along the body for 37.5 degrees. Figure 34 is the same plane as the streamlines in Figure 28. The stong gradient in density between the vortices is a crossflow shock. The density contours show what appears to be two circular structures where the primary vortices are usually located in crossflow separation. However, this is not the correct position as can be seen from comparison with the streamlines. The density contours indicate that the left vortex is closer to the body than it actually is. Figures 37-39 are constant vorticity contours at the same axial location of the density contours, again at 37.5 degrees. They also do not give the correct position of the left vortex. These calculations indicate that it is possible to have nearly symmetric vorticity and density countour plots when there are large asymmetries in the flow.

A calculation was completed at 37.5 degrees with the normal viscous term set to zero from 20 grid points away from the body to the farfield. Figure 40 shows the streamlines and can be compared with Figure 28. Since the streamlines were basically unchanged, the flow outside the boundary layer region is essentially inviscid and viscosity does not play a critical role in the relative size, shape, and location of the primary vortices. Based on the small effect of this normal viscous term, the thin-layer approximation produced accurate results away from the boundary layer region.

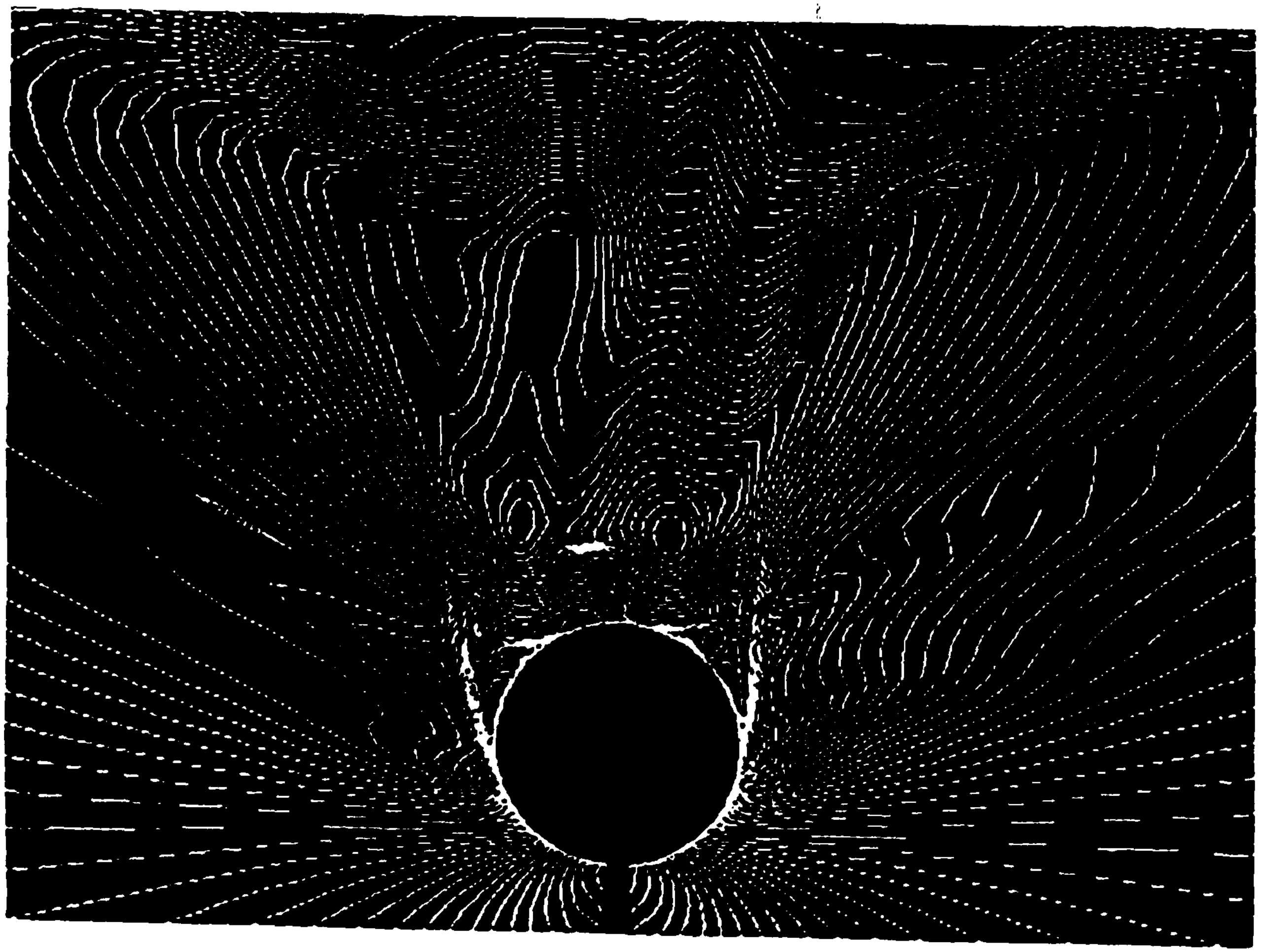

Figure 34. Constant Density Contours - Alpha = 37.5 deg, X/L = 97.0%

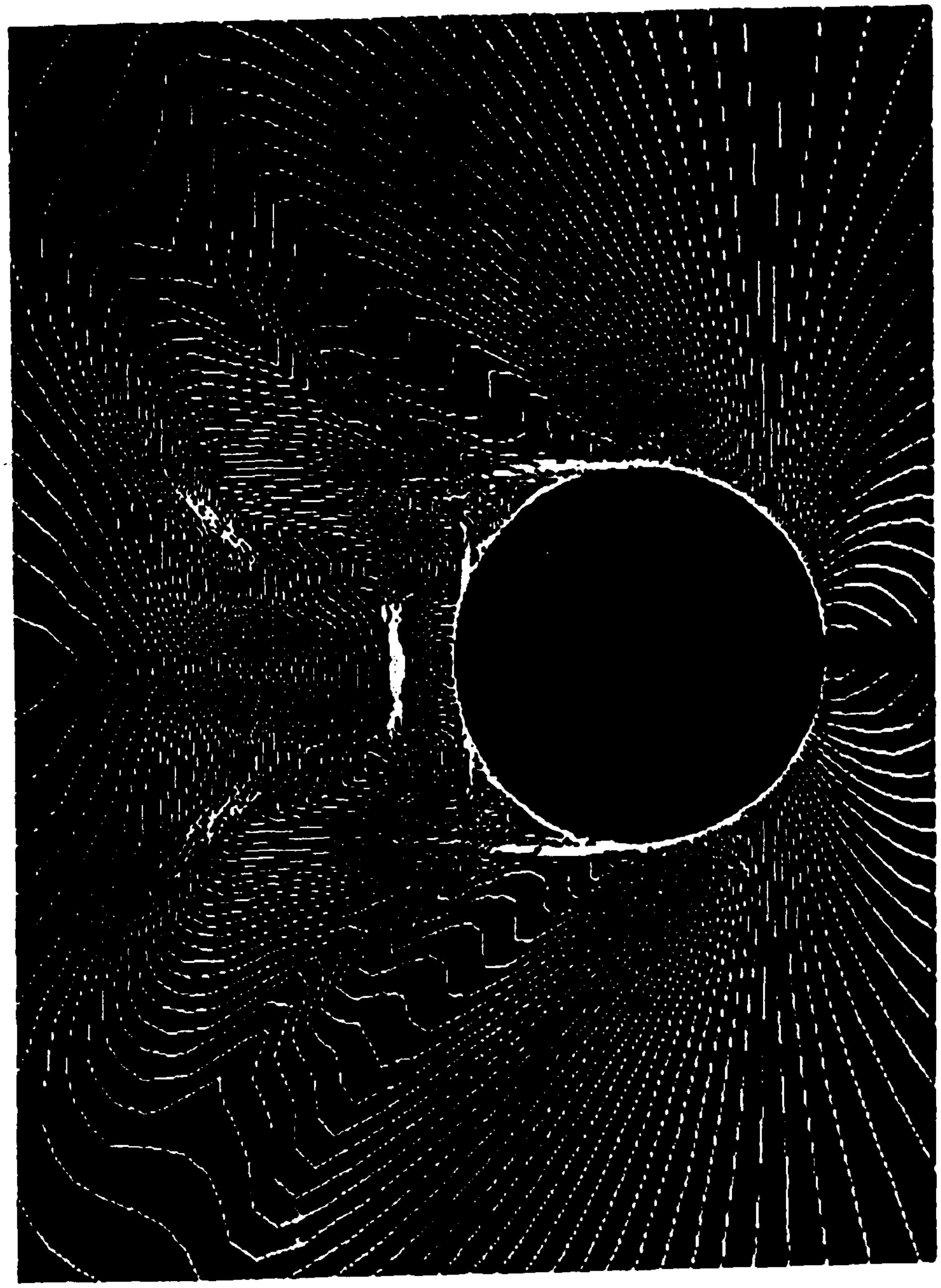

Figure 35. Constant Density Contours - Alpha = 37.5 deg, X/L = 31.0%

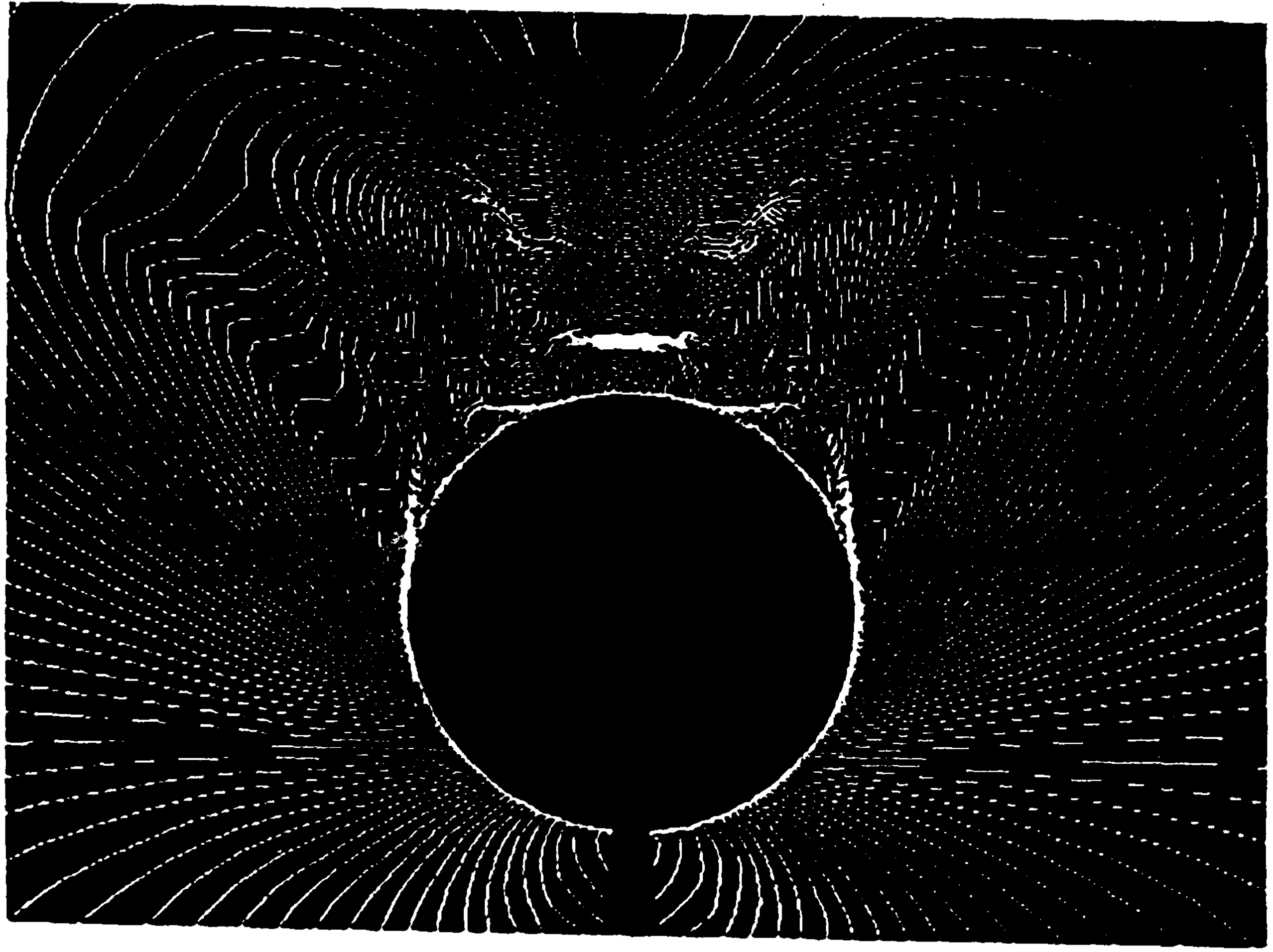

Figure 36. Constant Density Contours -
Alpha = 37.5 deg, X/L = 15.0%

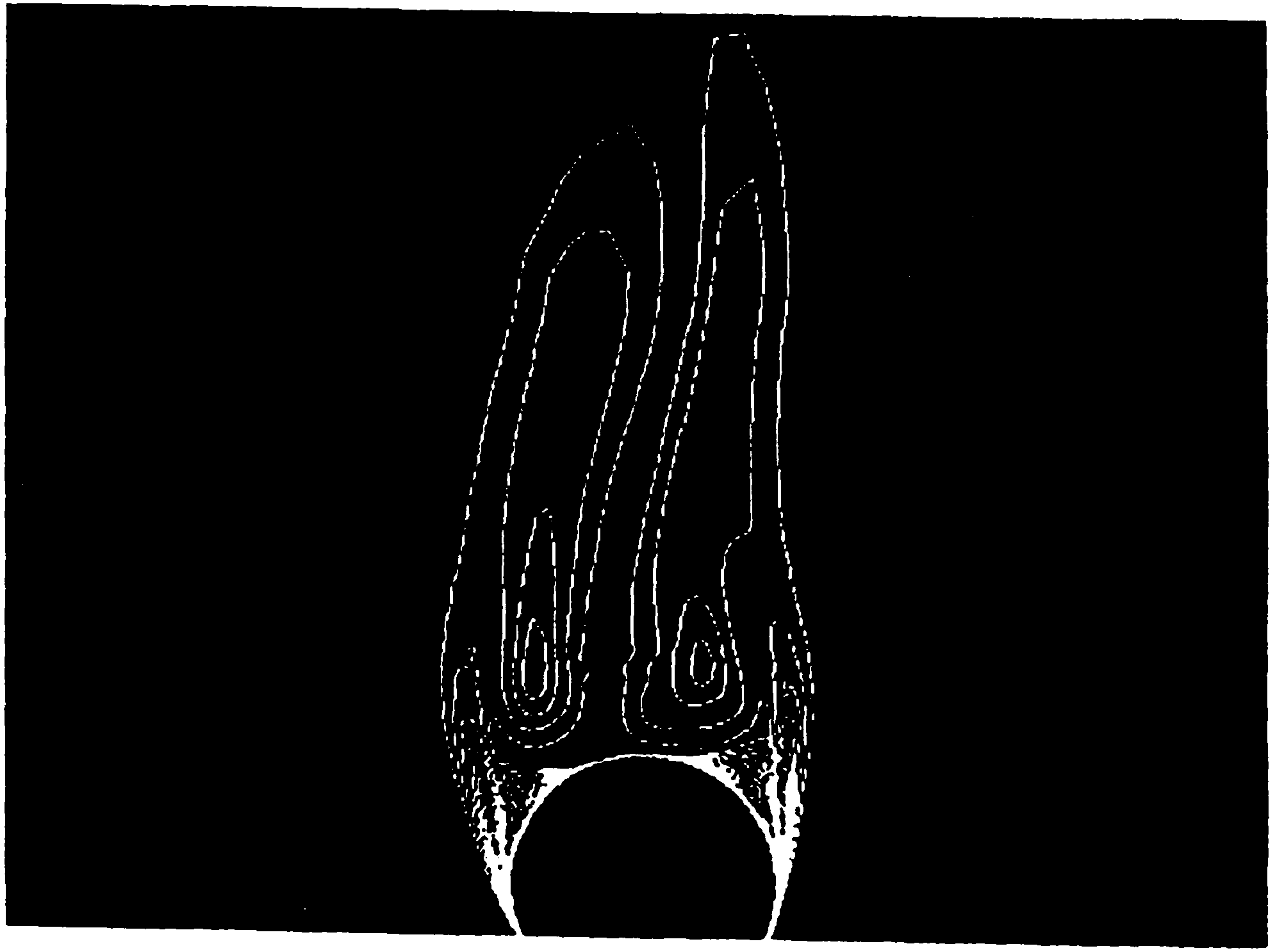

Figure 37. Constant Vorticity Contours - Alpha = 37.5 deg, X/L = 97.0%

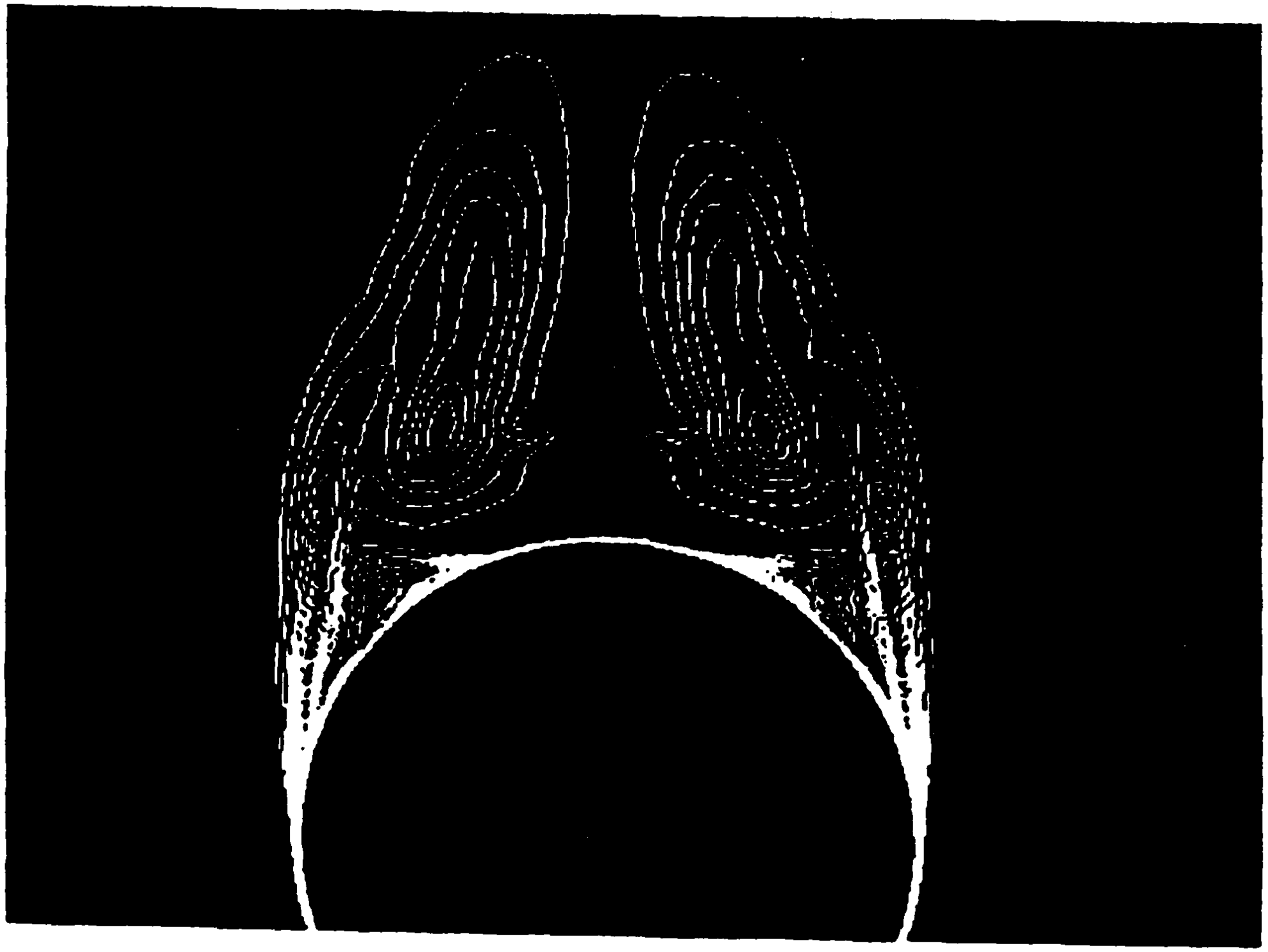

Figure 38. Constant Vorticity Contours - Alpha = 37.5 deg, X/L = 31.0%

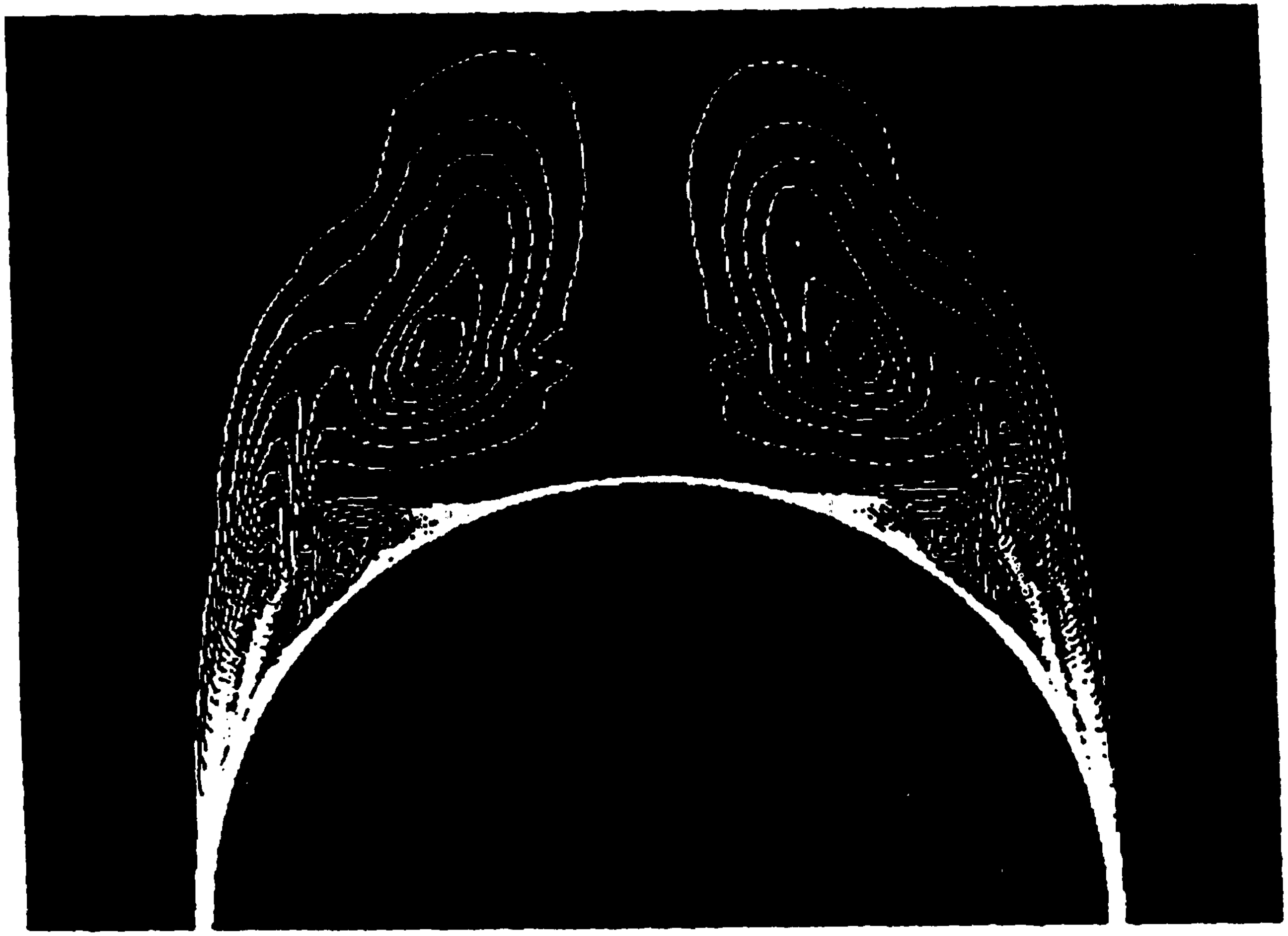

Figure 39. Constant Vorticity Contours -
Alpha = 37.5 deg, X/L = 15.0%

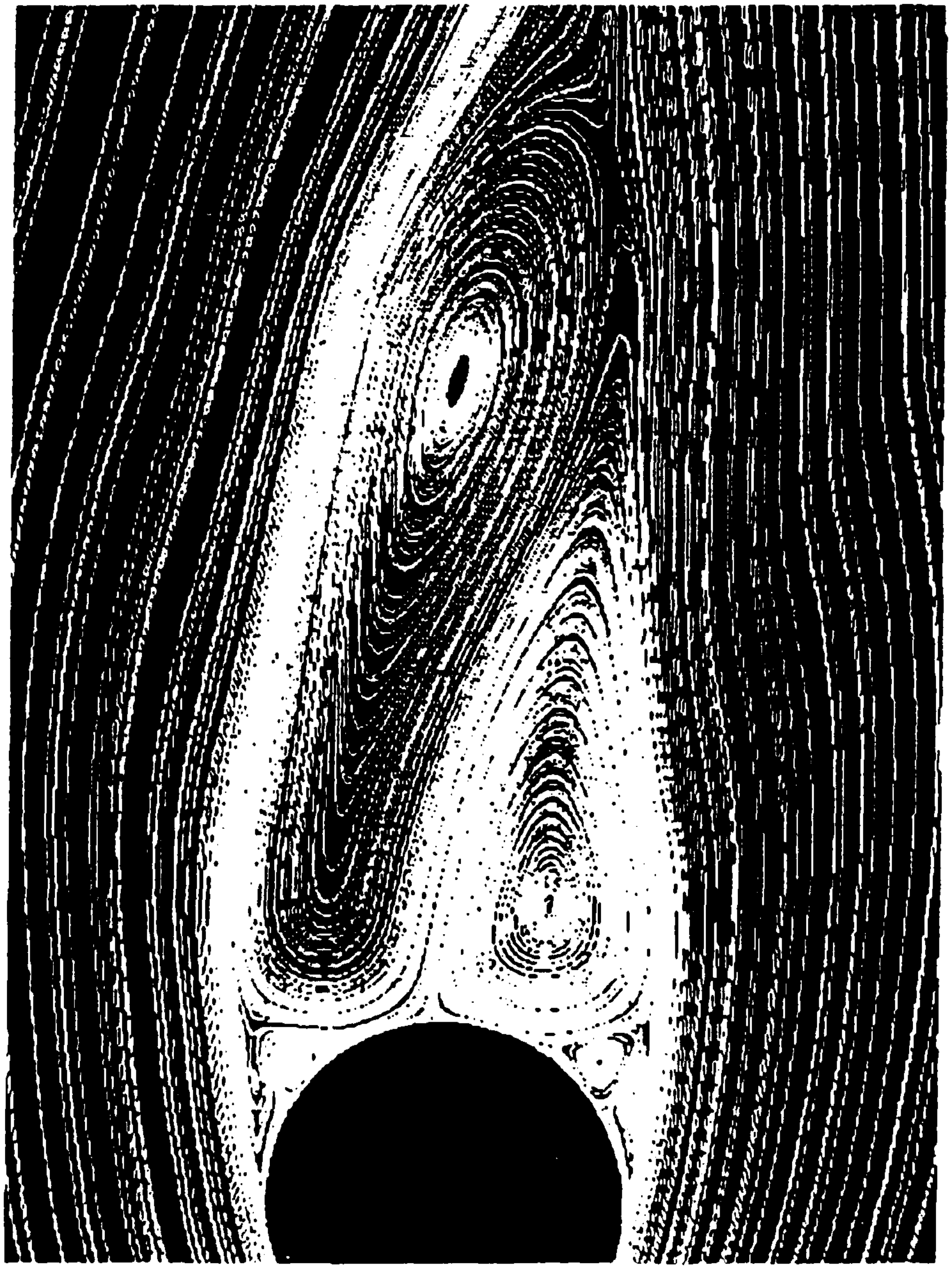

Figure 40. Streamlines - Alpha = 37.5 deg, X/L = 97.0%

Figure 41 shows the two-dimensional streamlines for 38.5 degrees. The additional degree from 37.5 degrees to 38.5 degrees has resulted in a third primary vortex appearing and an additional saddle point appearing between one of the previous primary vortices and the new one. Figure 42 shows an enlargement of the area containing the new vortex and the new primary saddle point. Figure 43 shows the three-dimensional streamlines that form the core of the new vortex. The primary vortex that was located the farthest from the body in the 37.5 degree case has moved even farther away in the 38.5 degree case. These two vortices rotate in the same direction and are fed by the same shear layer. They are separated by a separatrix of the saddle point. The vorticity contours in Figures 44-49 show this shear layer at different longitudinal locations. This third vortex appears to occur when the primary vortex flattens sufficiently to pinch off a portion of itself, thus forming a separate region of rotation. This agrees well with the conceptual three vortex configuration given by Peake and Tobak[32]. Figures 50 and 51 show the entire left side secondary flow region, and Figure 52 shows the right side. The secondary flows on both sides contain the same singular points as the 37.5 degree case (Figures 30-32). The additional foci and saddle point in the primary flow region balance each other in the topological summation equation. In the entire cross-flow plane there are 12 half saddles, 10 foci, and 5 saddles (Figure 53). Substituting into the topological summation equations gives

$$(10 + \frac{0}{2}) - (5 + \frac{12}{2}) = -1$$

in complete agreement. The limiting streamlines on the rear of the body

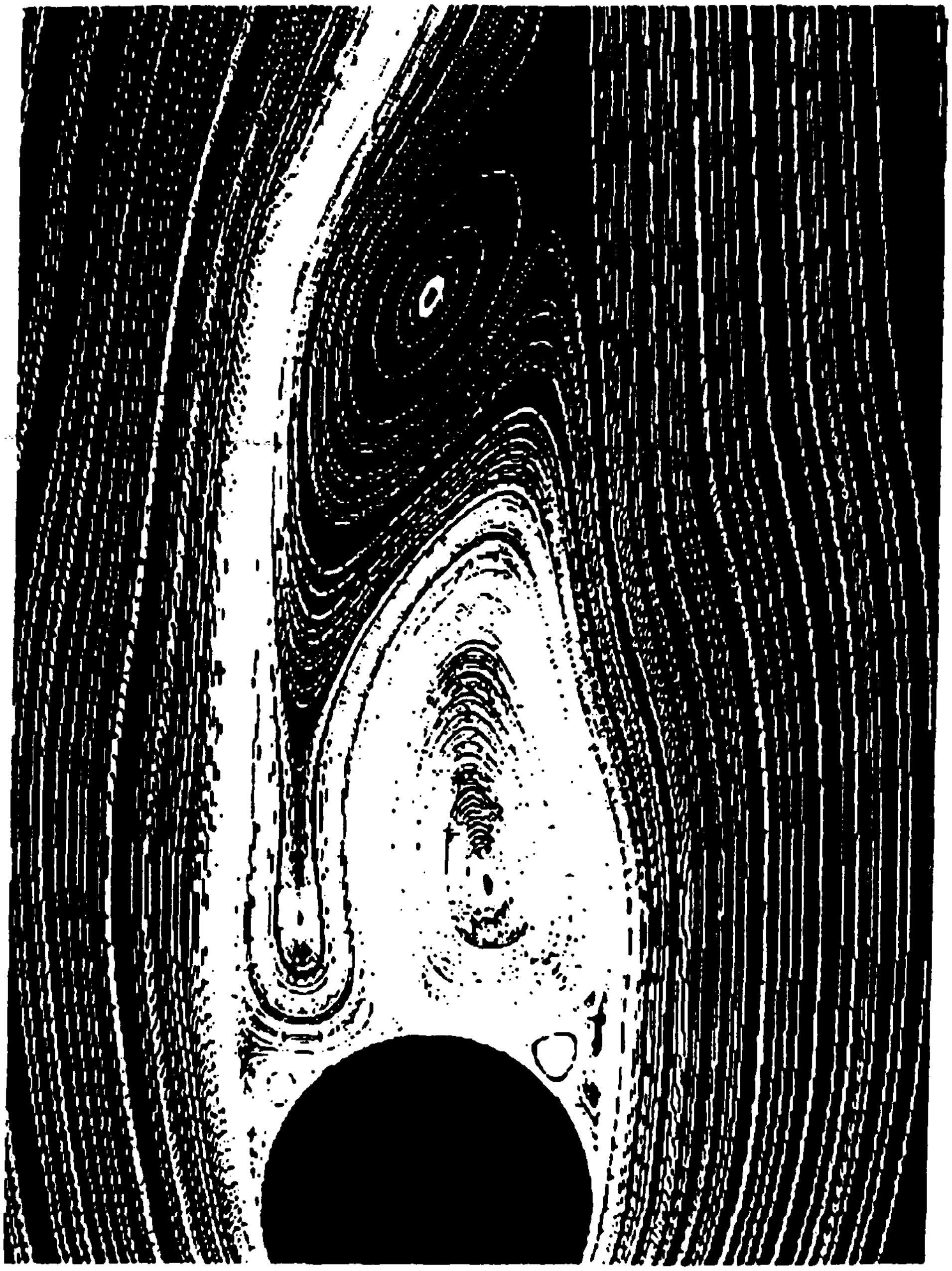

Figure 41. Streamlines - Alpha = 38.5 deg, X/L = 97.0%

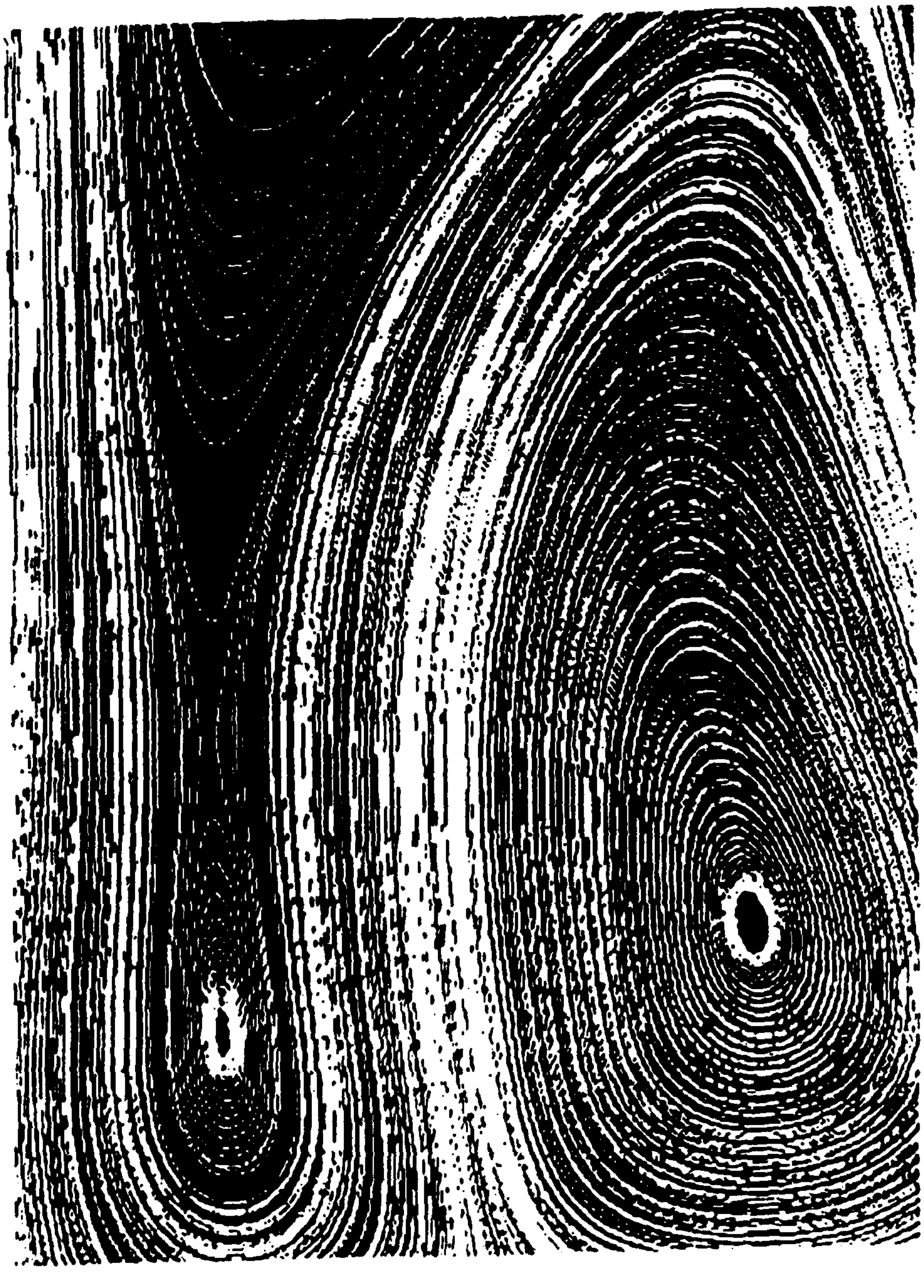

Figure 42. Streamlines - Alpha = 38.5 deg, X/L = 97.0%

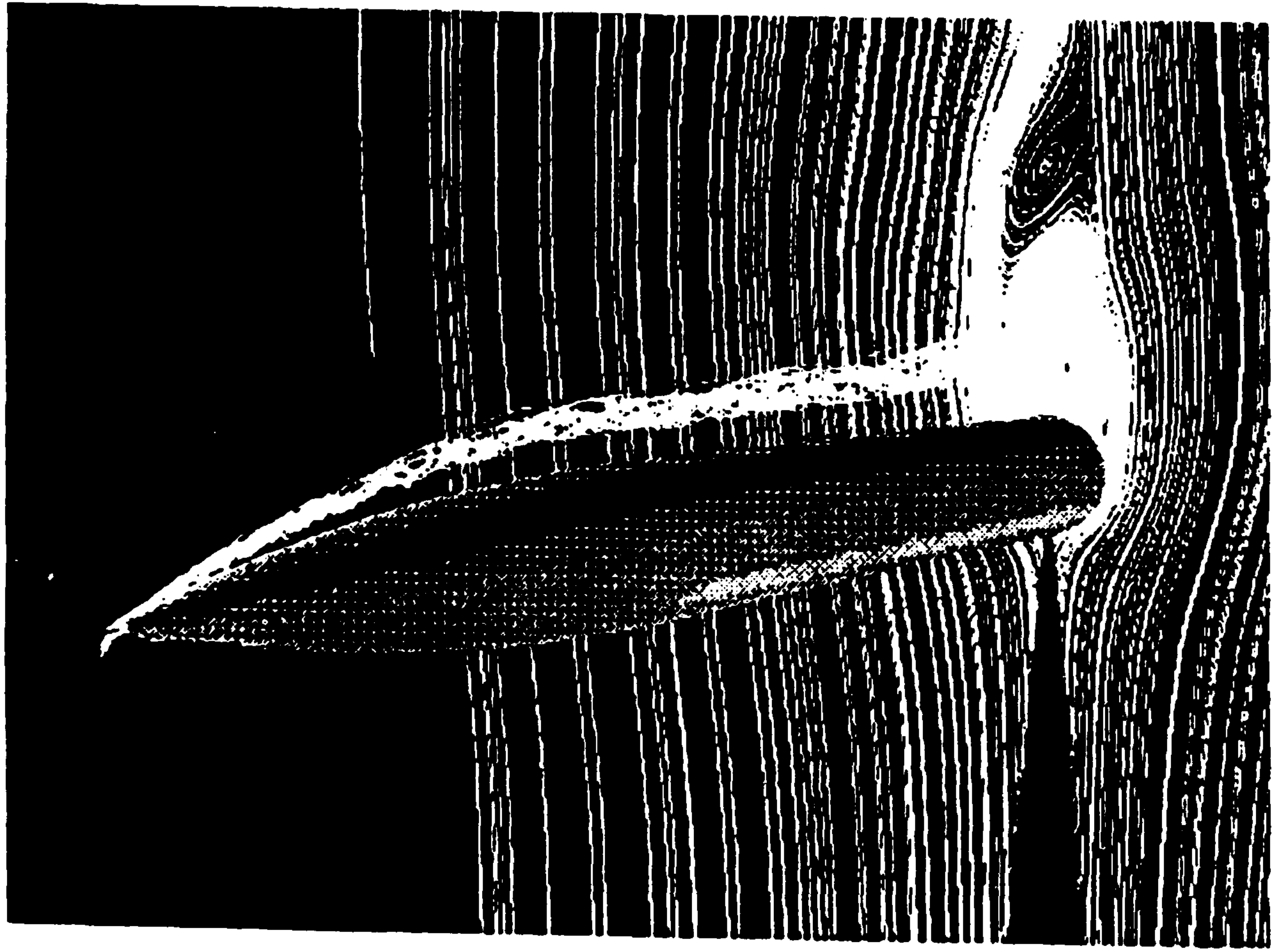

Figure 43. Three-Dimensional Streamlines of New Vortex - Alpha = 38.5 deg, X/L = 97.0%

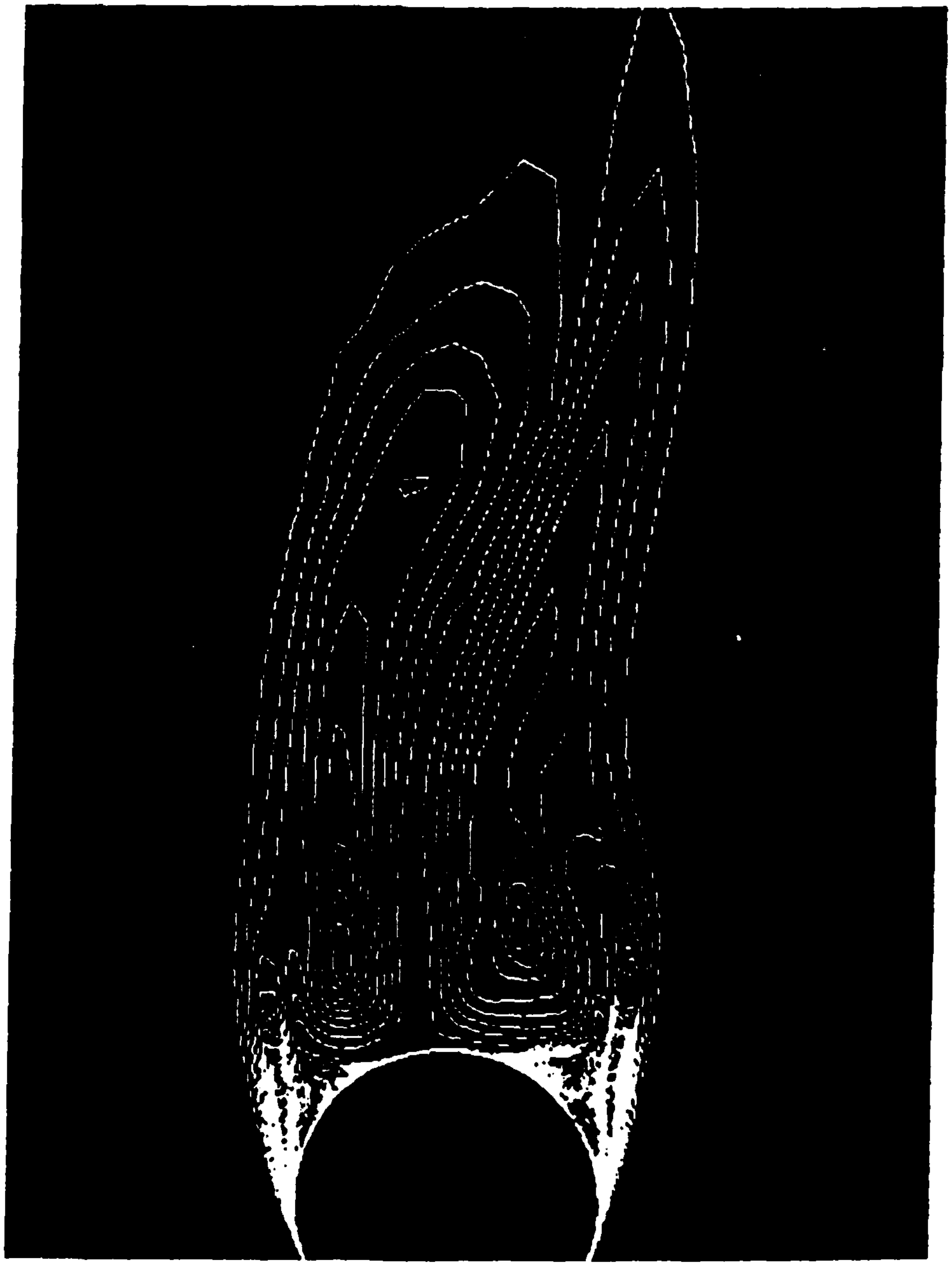

Figure 44. Constant Vorticity Contours - Alpha = 38.5 deg, X/L = 55.0%

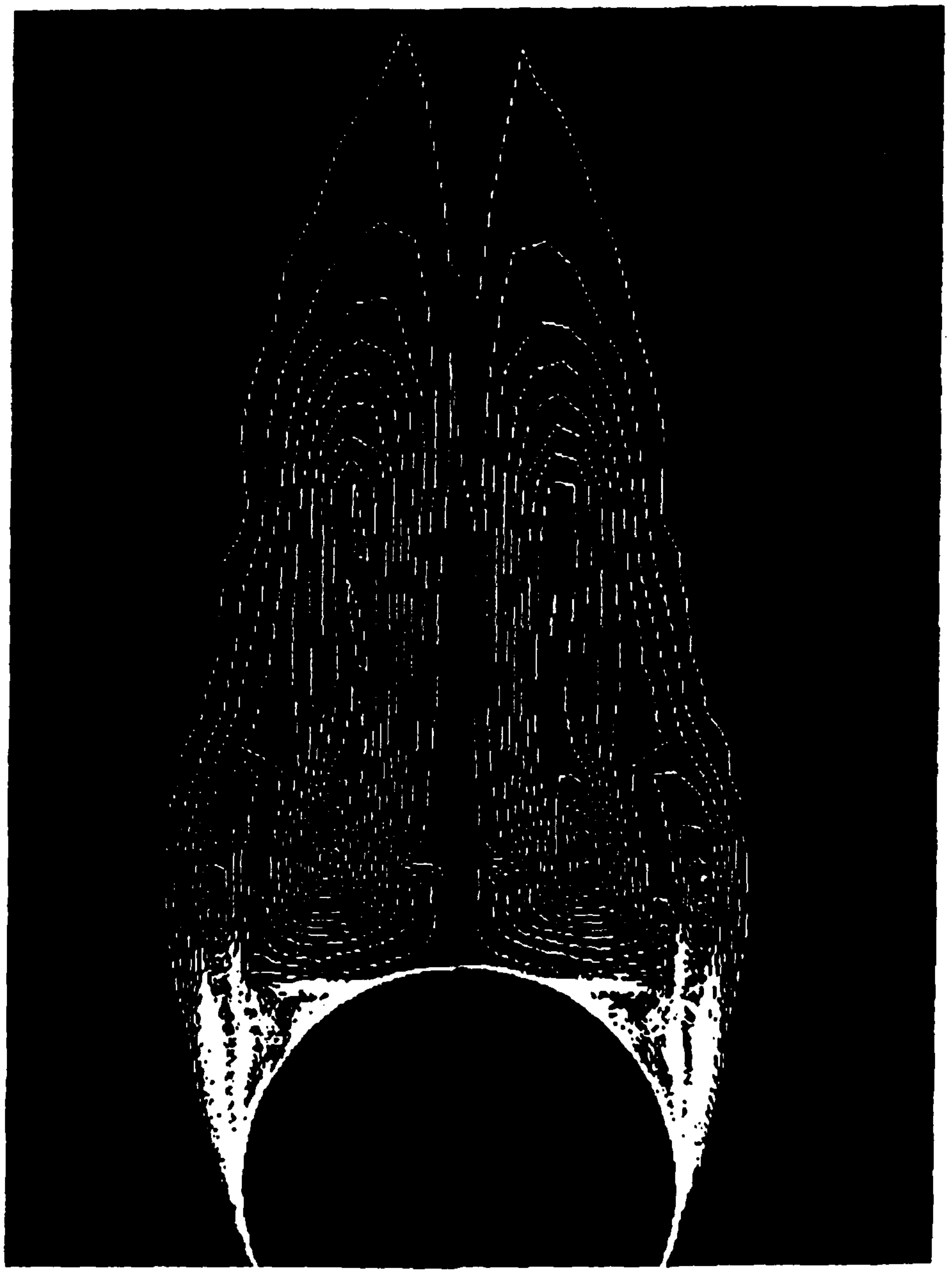

Figure 45. Constant Vorticity Contours - Alpha = 38.5 deg, X/L = 52.0%

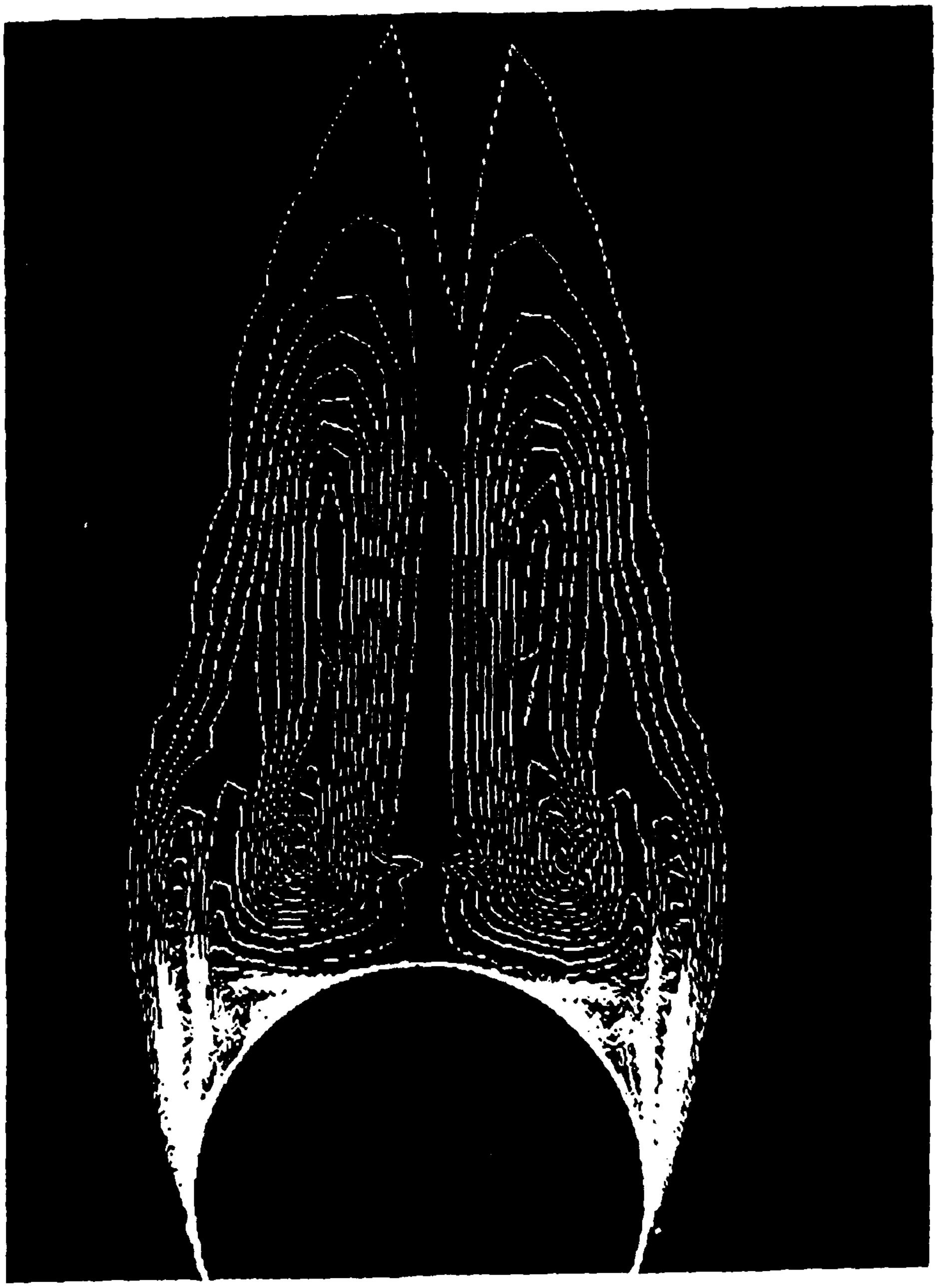

Figure 46. Constant Vorticity Contours -
Alpha = 38.5 deg, X/L = 50.0%

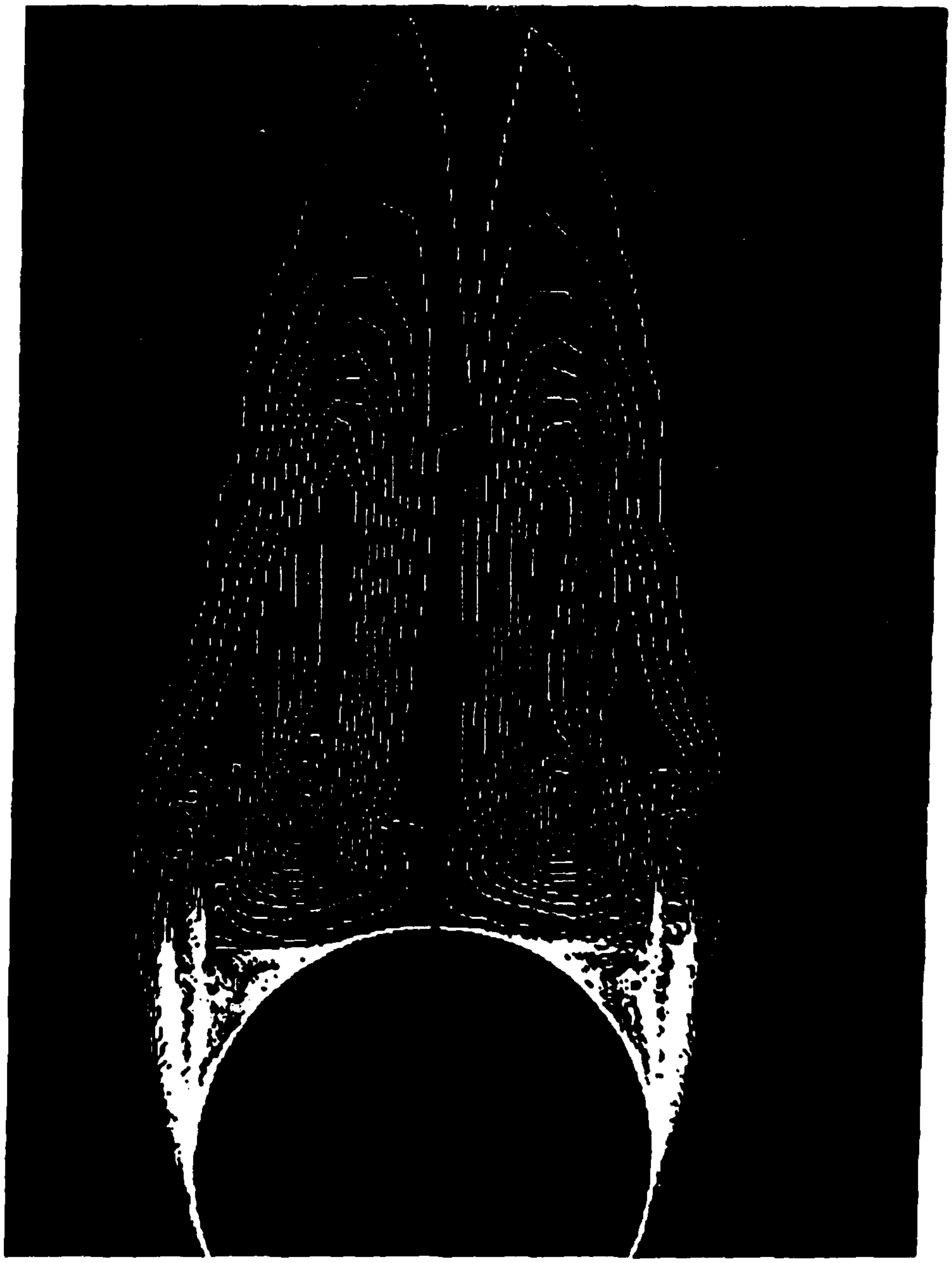

Figure 47. Constant Vorticity Contours - Alpha = 38.5 deg, X/L = 48.0%

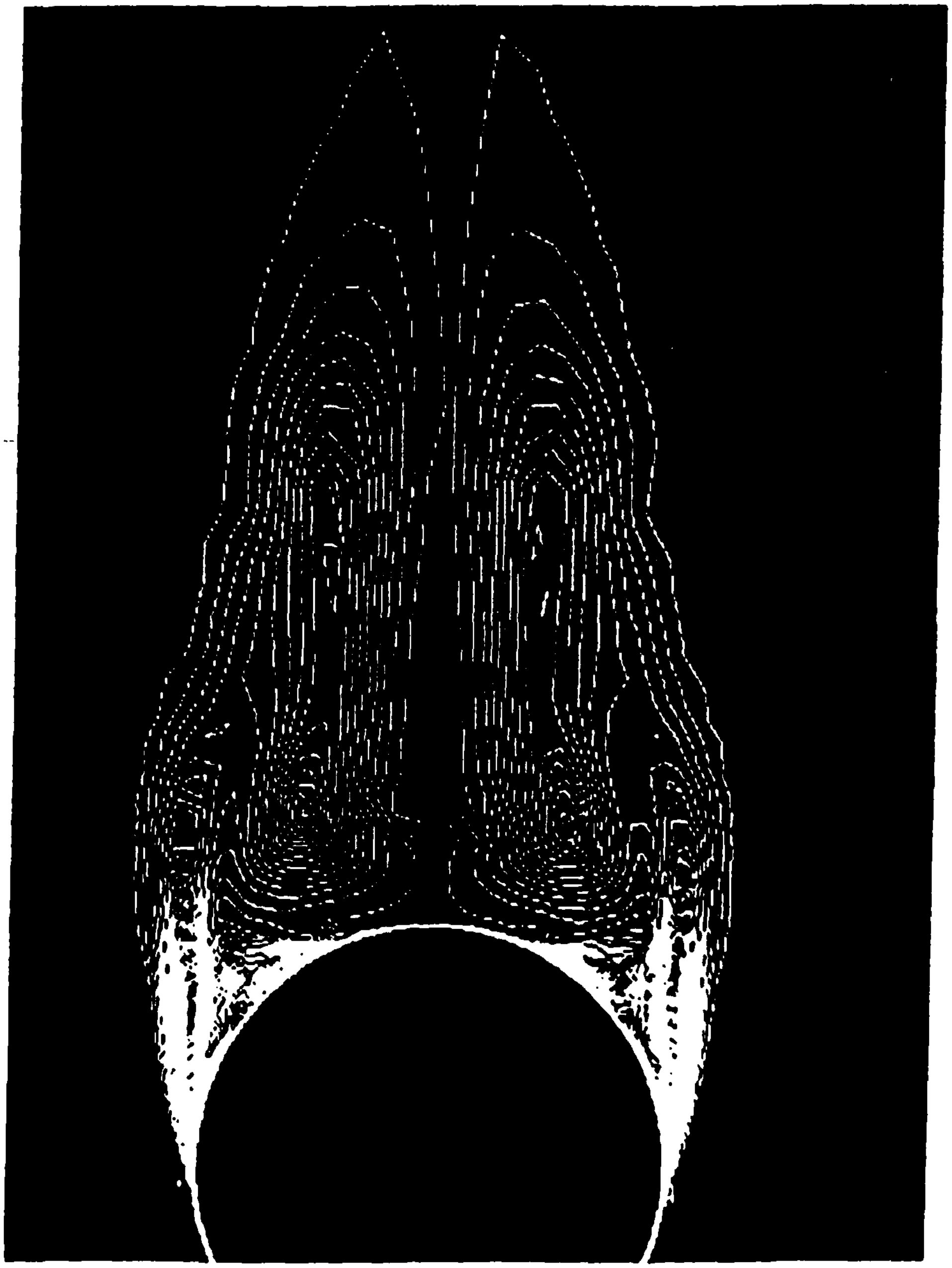

Figure 48. Constant Vorticity Contours - Alpha = 38.5 deg, X/L = 45.0%

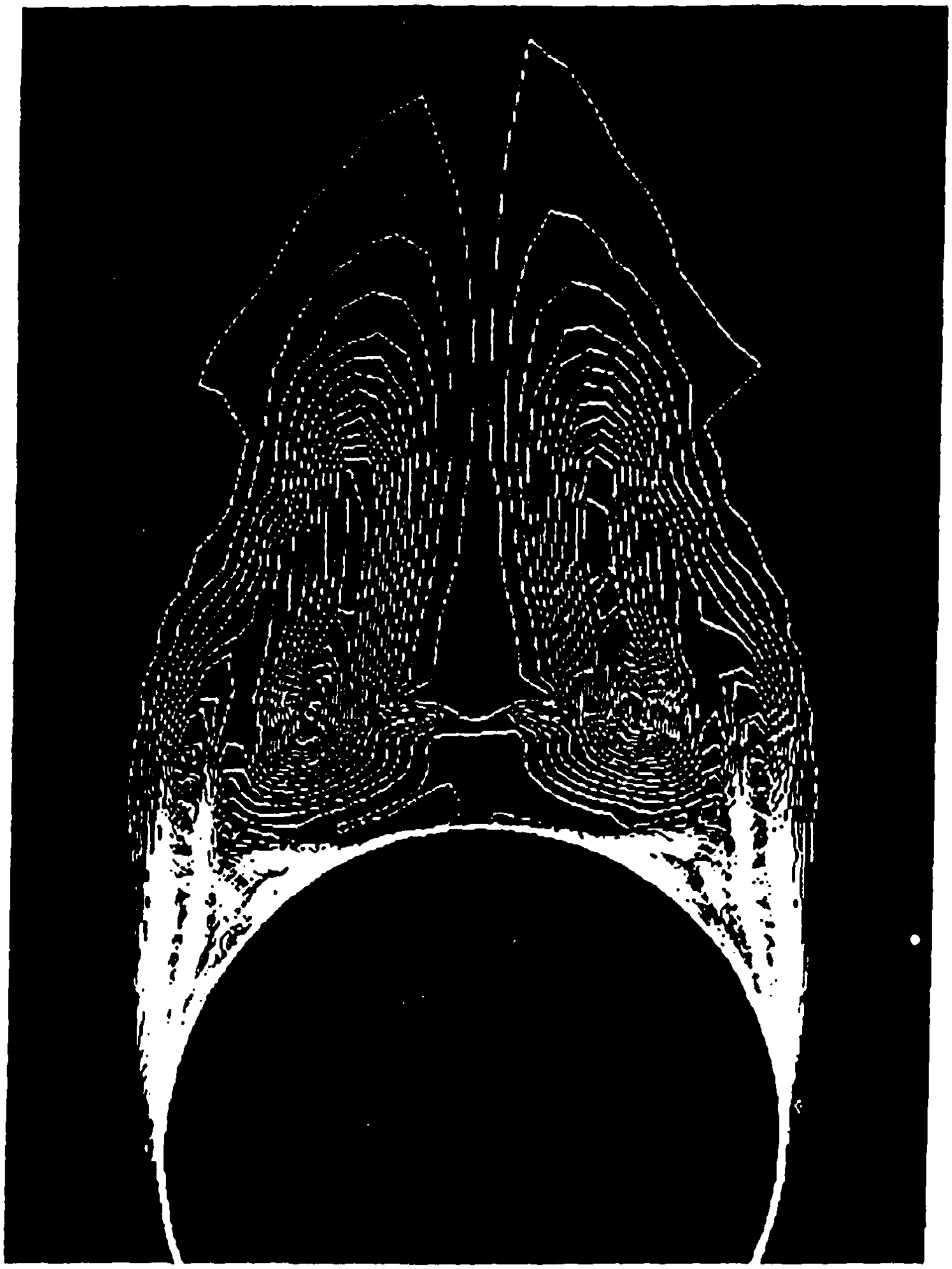

Figure 49. Constant Vorticity Contours - Alpha = 38.5 deg, X/L = 30.0%

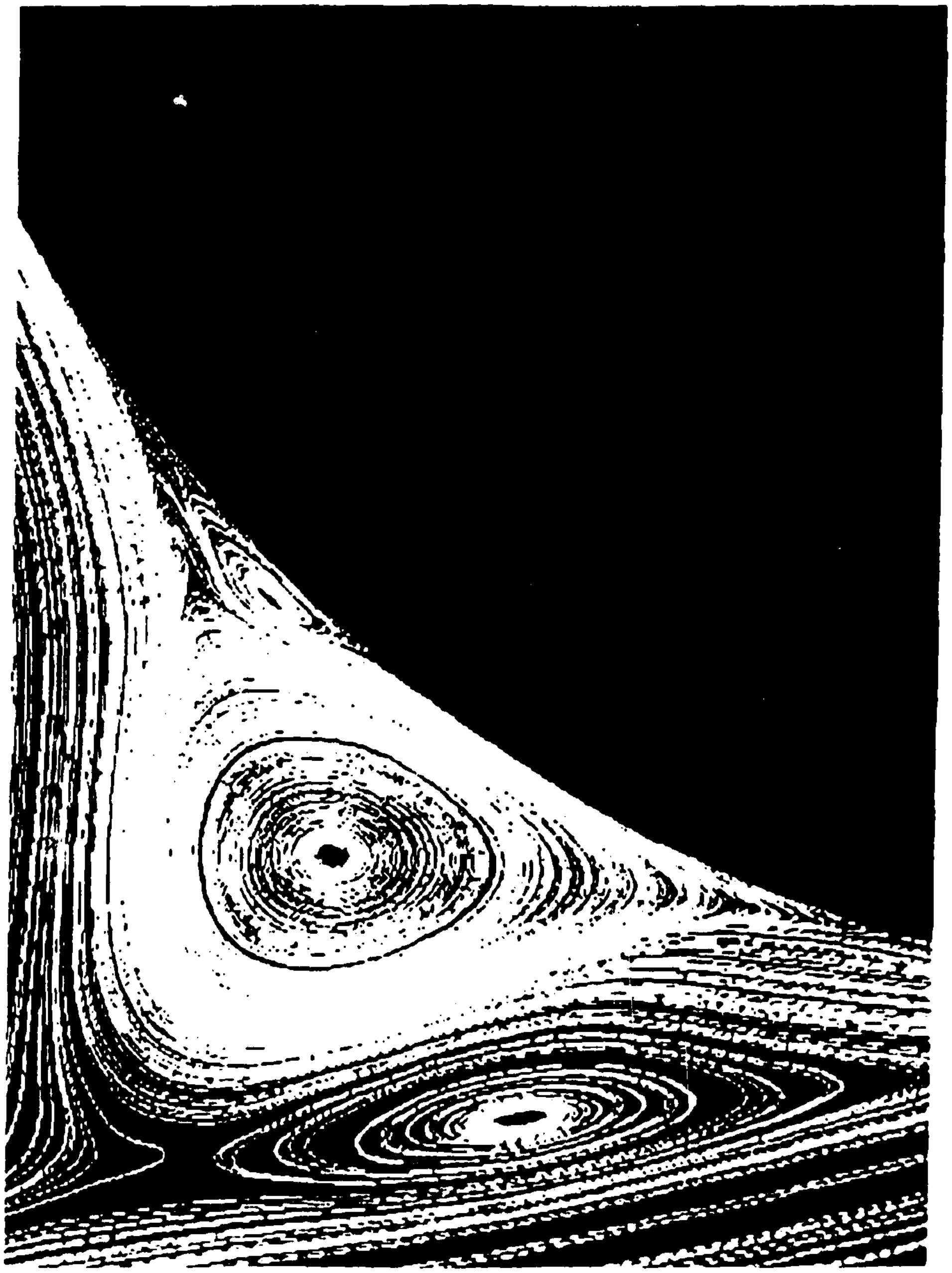

Figure 50. Left Side Secondary Flow Streamlines - Alpha = 38.5 deg, X/L = 97.0%

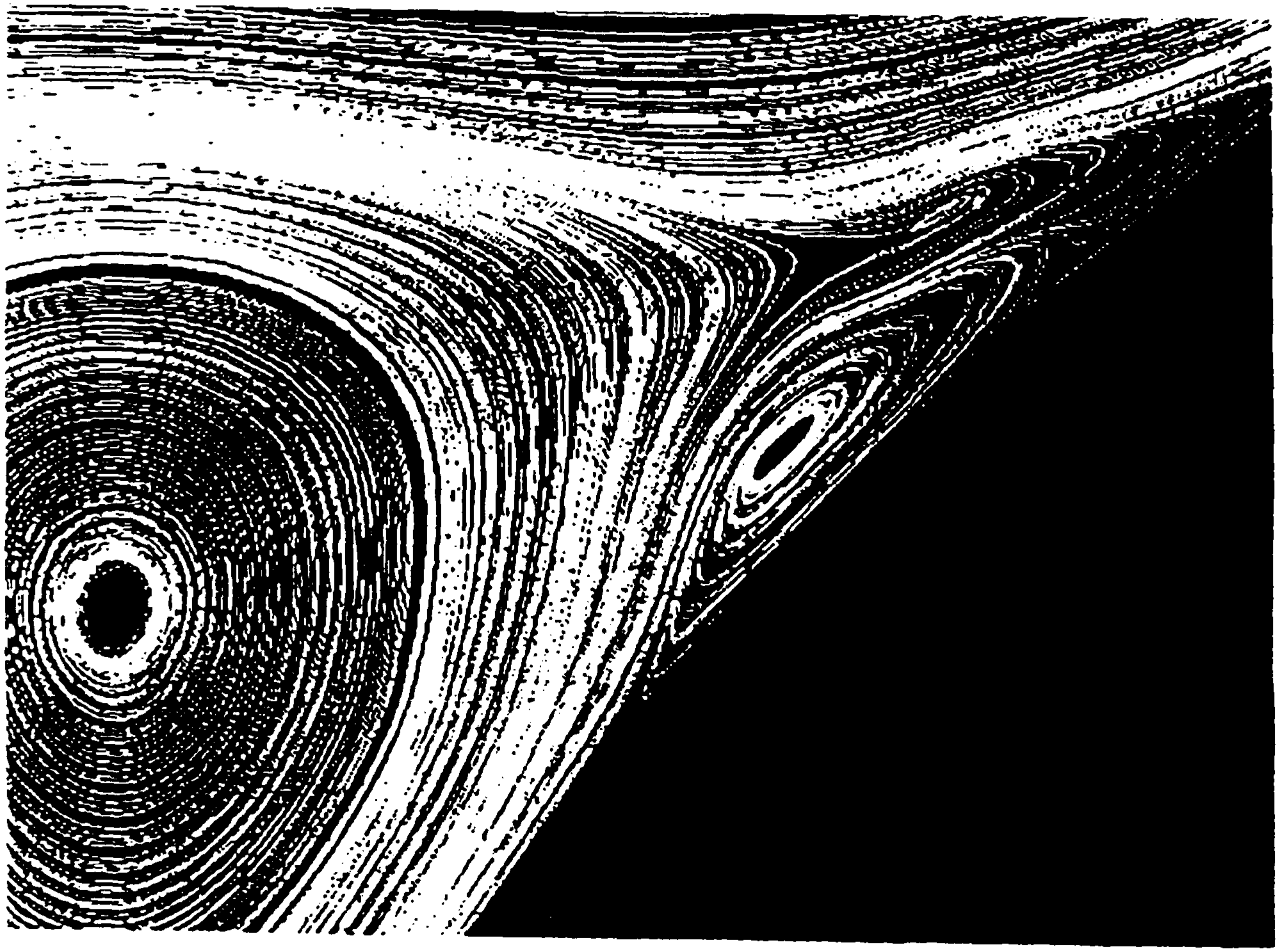

Figure 51. Left Side Secondary Flow Streamlines - Alpha = 38.5 deg, X/L = 97.0%

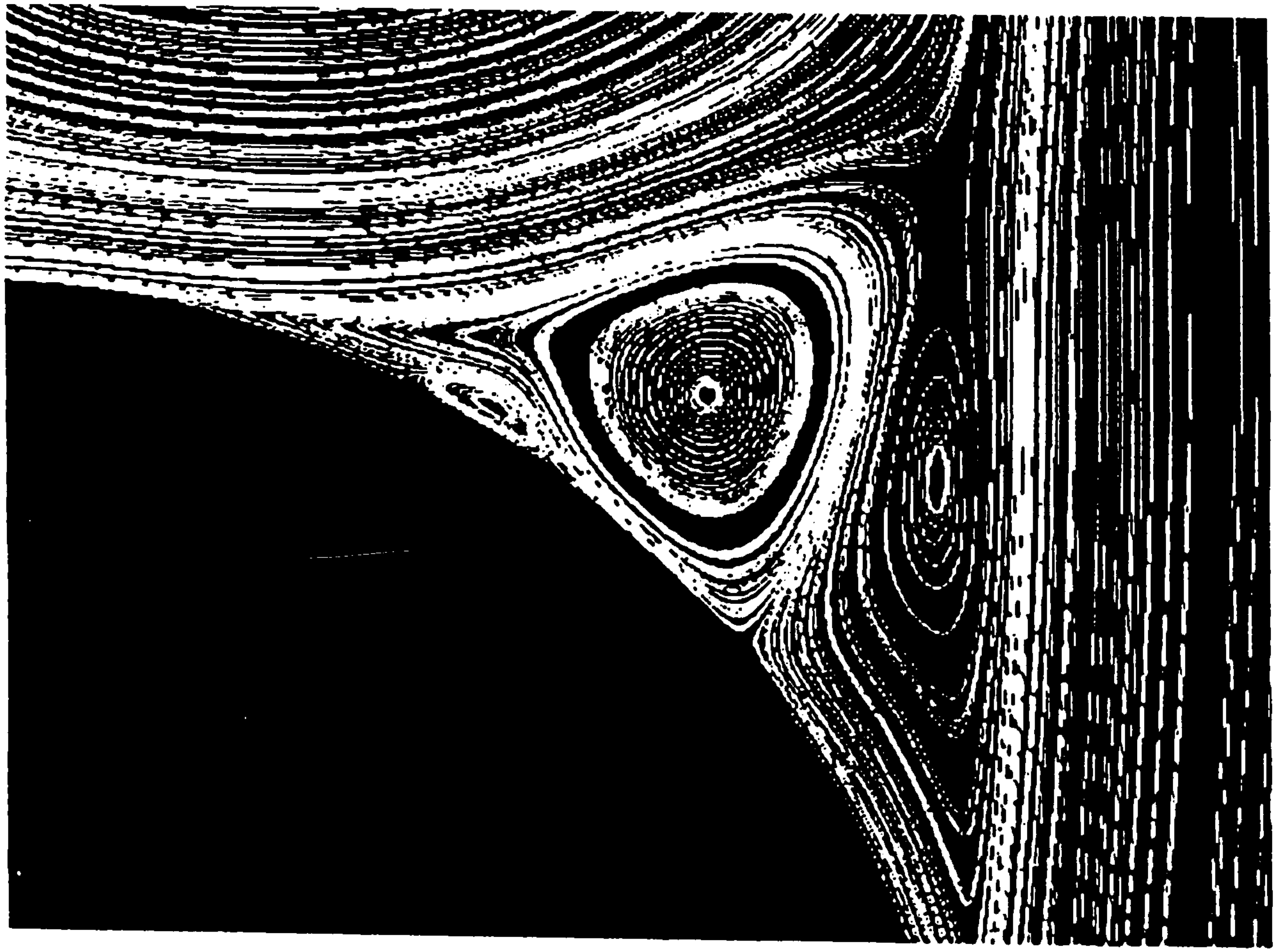

Figure 52. Right Side Secondary Flow Streamlines -
Alpha = 38.5 deg, X/L = 97.0%

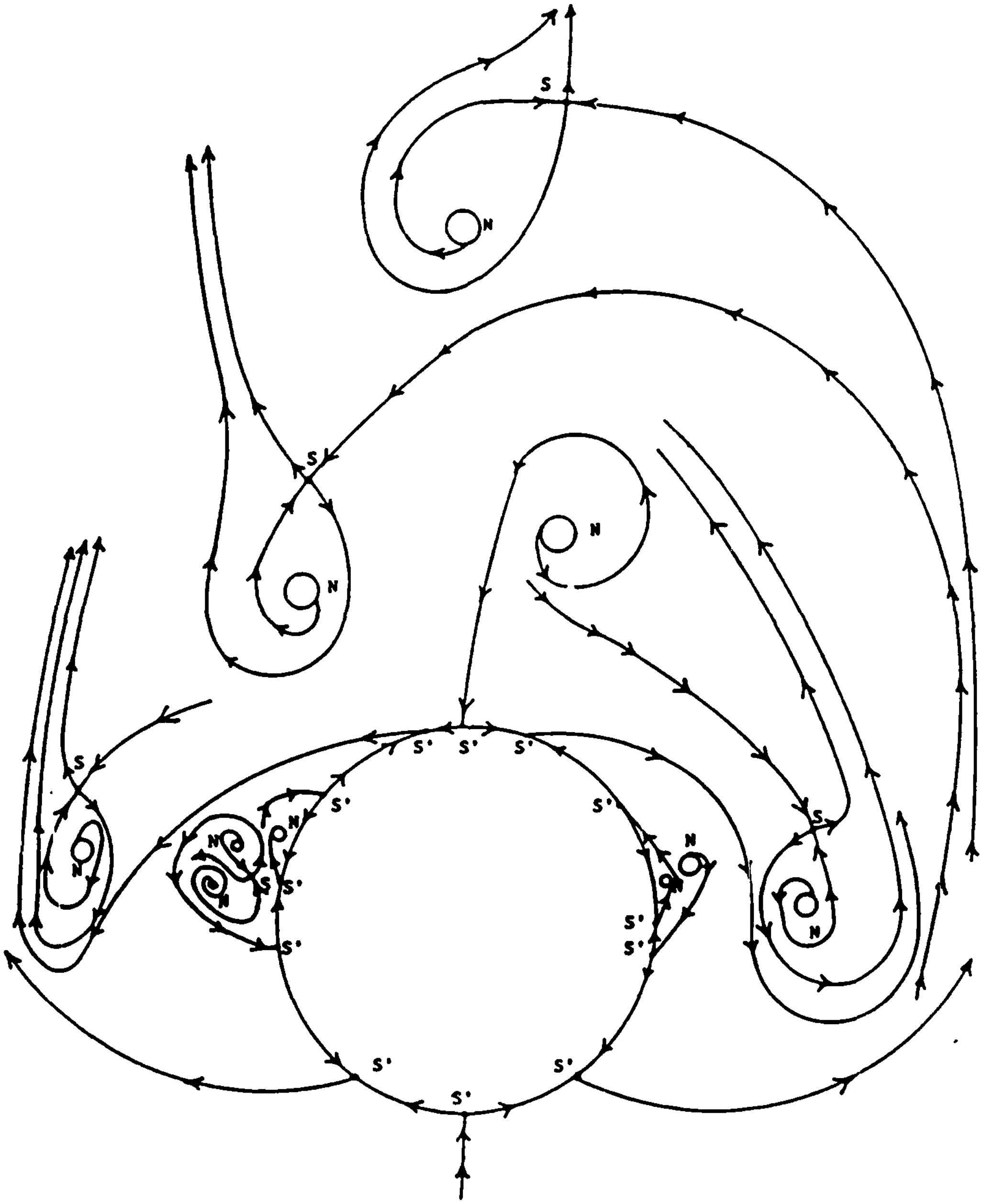

Figure 53. Crossflow Topology -
Alpha = 38.5 deg, X/L = 97.0%

are shown in Figure 54. The separation and attachment convergence lines are noticeably more skewed than the 37.5 degree case (Figure 33). The particle traces forming the first attachment line above the primary separation line on the right side appear to spread apart. This is from the plotting package and not part of the flow structure. This software draws particle traces in both the upstream and downstream directions. Since the body is terminated, and not infinite, there is a region near the base that only particle traces from the upstream direction reach. Thus, the convergence lines formed by limiting streamlines are not resolved well.

Figure 55 shows the streamlines for 40.0 degrees angle of attack. Since no calculations were made between 38.5 degrees (Figure 42) and 40.0 degrees it is impossible to determine how the flow reached this new state. However, it is clear that major changes took place going from the three vortex configuration of 38.5 degrees (Figure 42) to a two vortex configuration. One vortex of the 40.0 degree calculation is very near the body and similar in shape to the vortices observed at lower angles of attack. The other vortex is much larger and very irregular in shape. The saddle point associated with these two primary vortices is to the left of the center of the smaller vortex and nearly in line with the left side of the body. Figure 56 shows the streamlines in the right secondary flow region. The arrangement and type of singular points is similar to that already discussed for lower angles of attack except a foci-saddle combination has disappeared. The particle traces of the left secondary flow (Figure 57) show the most complex topology yet calculated. There are three foci and two saddle points in addition to two half saddle points on the body. An enlargement of the region with the two

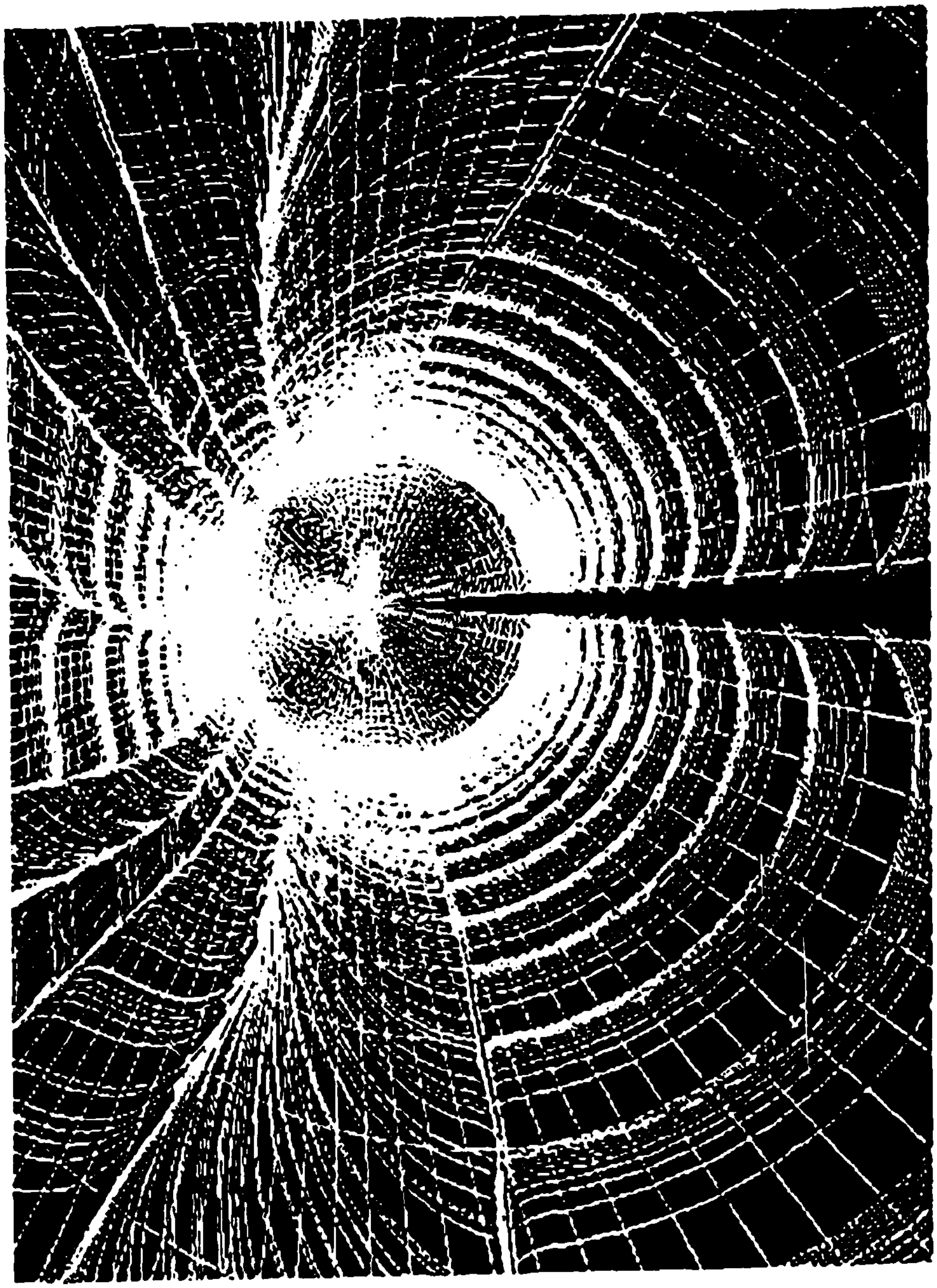

Figure 54. Rear Body Limiting Streamlines -
Alpha = 38.5 deg, X/L = 97.0%

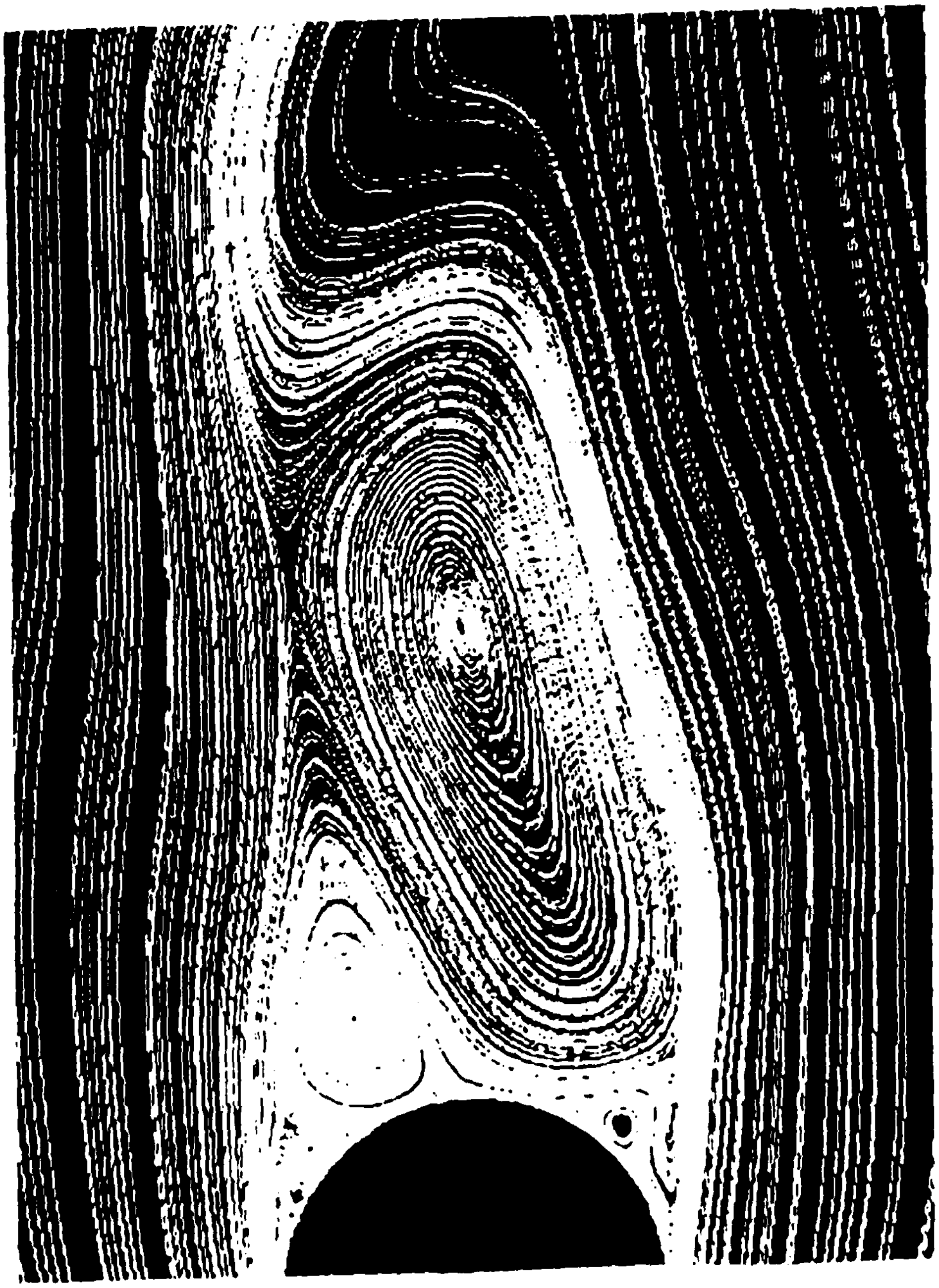

Figure 55. Streamlines - Alpha = 40.0 deg, X/L = 97.0%

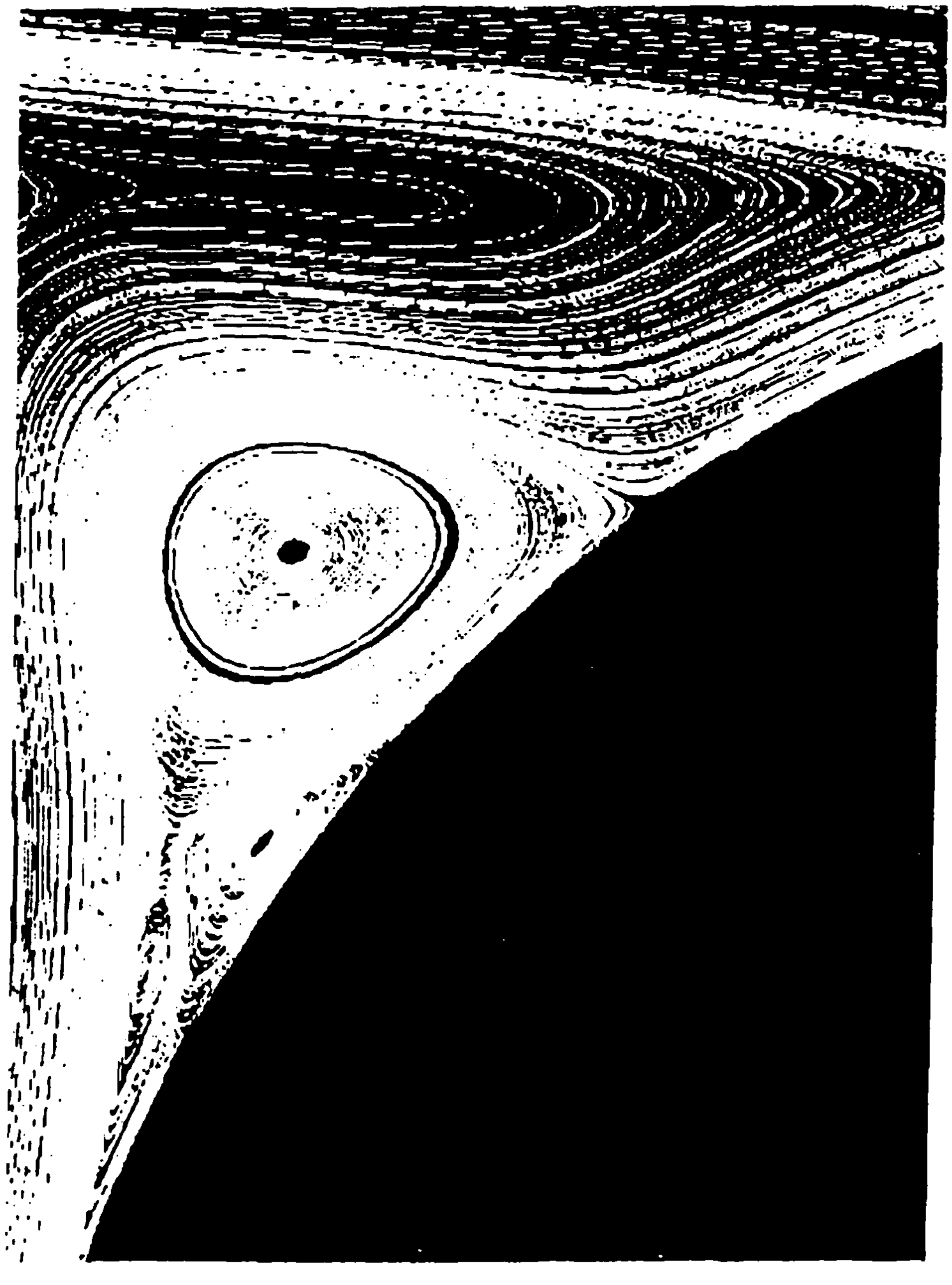

Figure 56. Right Side Secondary Flow Streamlines - Alpha = 40.0 deg, X/L = 97.0%

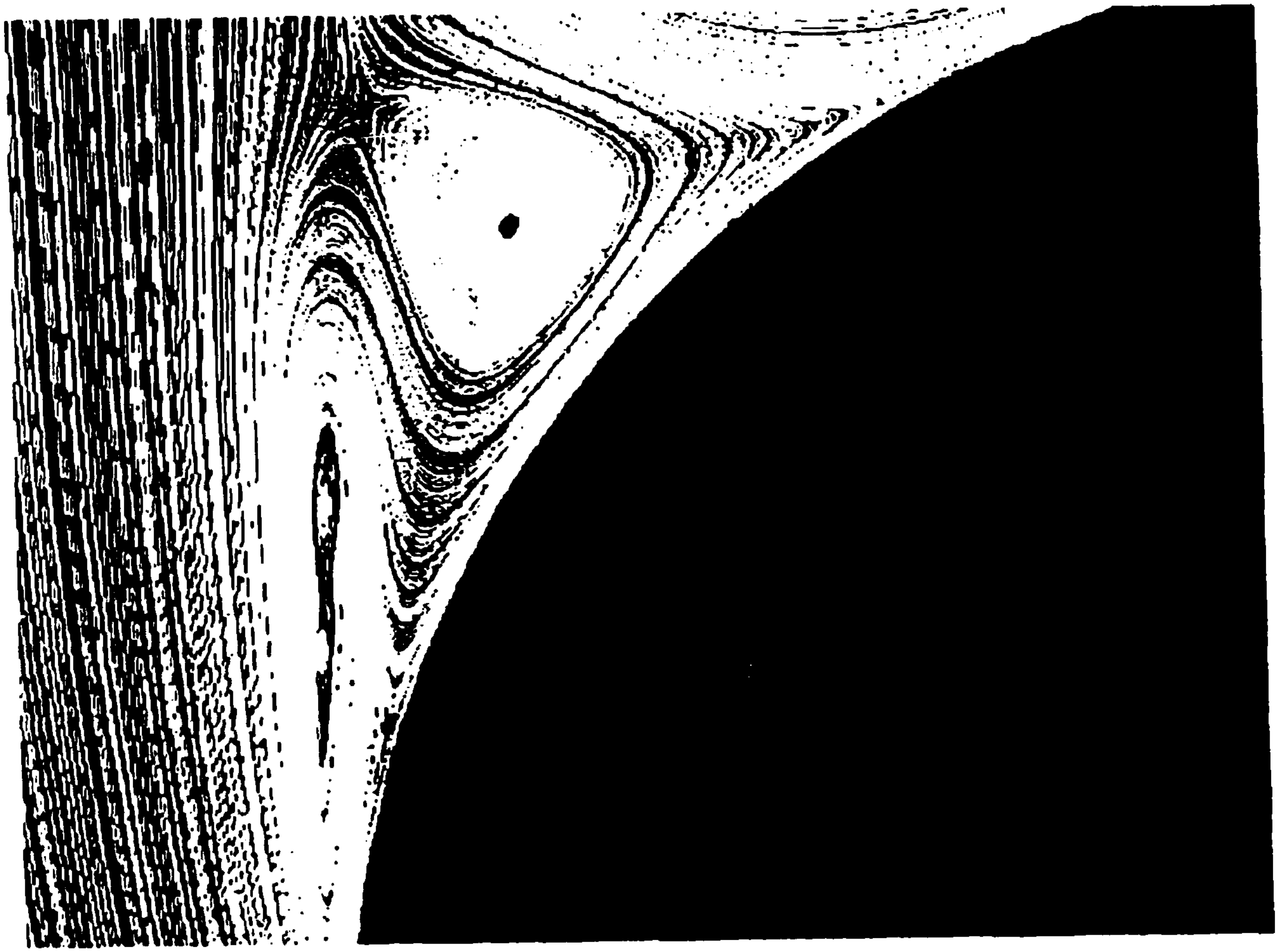

Figure 57. Left Side Secondary Flow Streamlines - Alpha = 40.0 deg, X/L = 97.0%

foci-saddle point combination is shown in Figure 58. This gives, in the overall flow, eight nodes, three saddles, and 12 half saddle points. Substituting into the topology summation equation gives

$$(7 + \frac{0}{2}) - (2 + \frac{12}{2}) = -1$$

again in complete agreement. Figure 59 shows the limiting streamlines on the rear of the body. They are highly asymmetric and contain a number of sharp kinks.

Figures 60-64 show the circumferential coefficient of pressure at X/L=97.0% for all the angles of attack calculated. Theta equal to zero and 360 correspond to the windward stagnation point. The direction of rotation is clockwise in relation to the two-dimensional streamline calculations previously shown. The symmetric pressure coefficient distribution agrees qualitatively with Lamont[6] and Ericsson and Reding[33]. The bumps in the pressure coefficient at approximately a theta of 135 degrees for each of the cases correspond to the portion of the secondary flow with the small vortices nearest the body. Table 1 gives the forces and moments for all cases calculated. Since the free stream flow is supersonic the vortex-induced side forces are smaller than the normal force, agreeing qualitatively with Lamont[6], Ericsson and Redding[34], and Keener[9] et al.

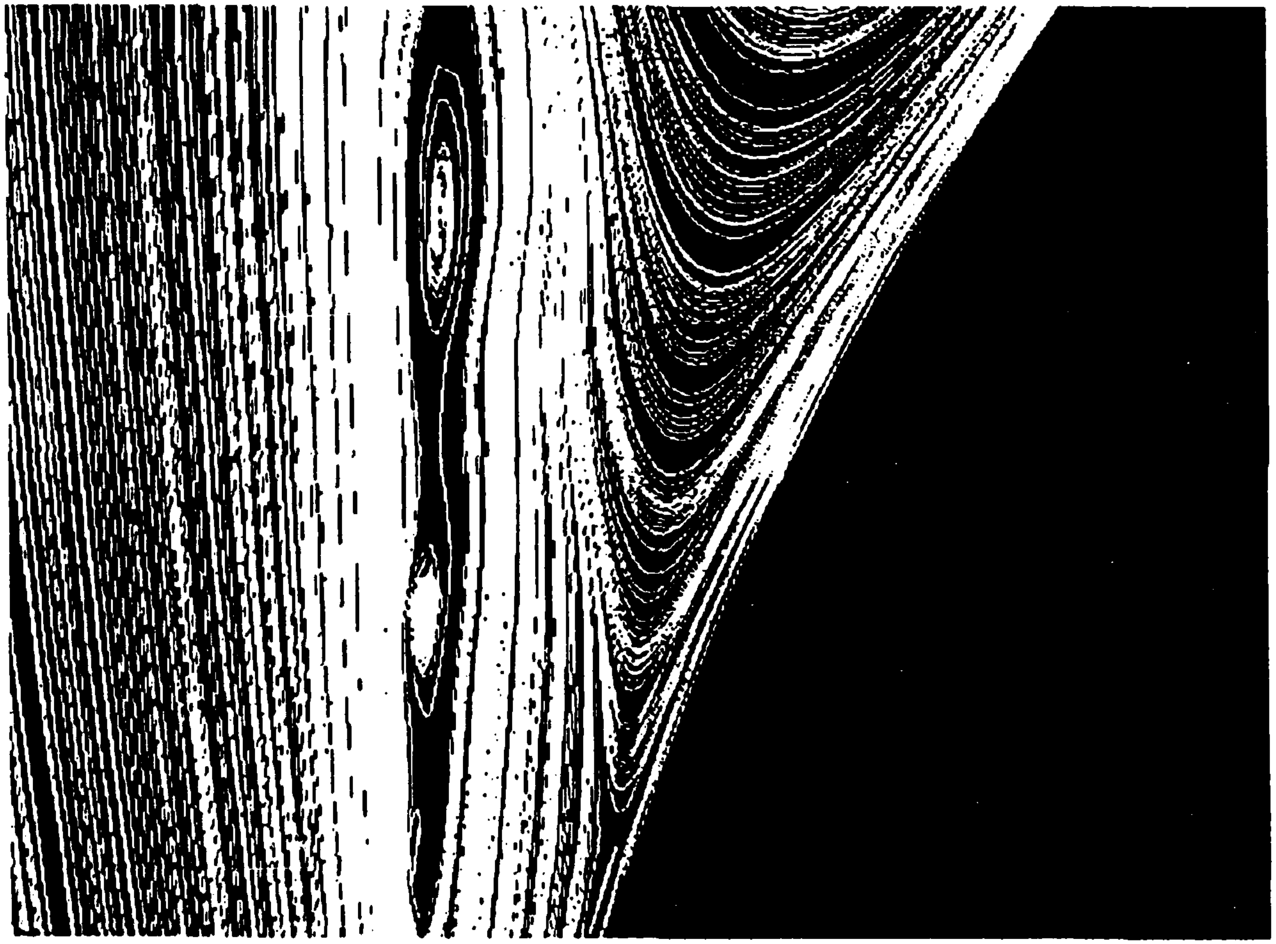

Figure 58. Left Side Secondary Flow Streamlines - Alpha = 40.0 deg, X/L = 97.0%

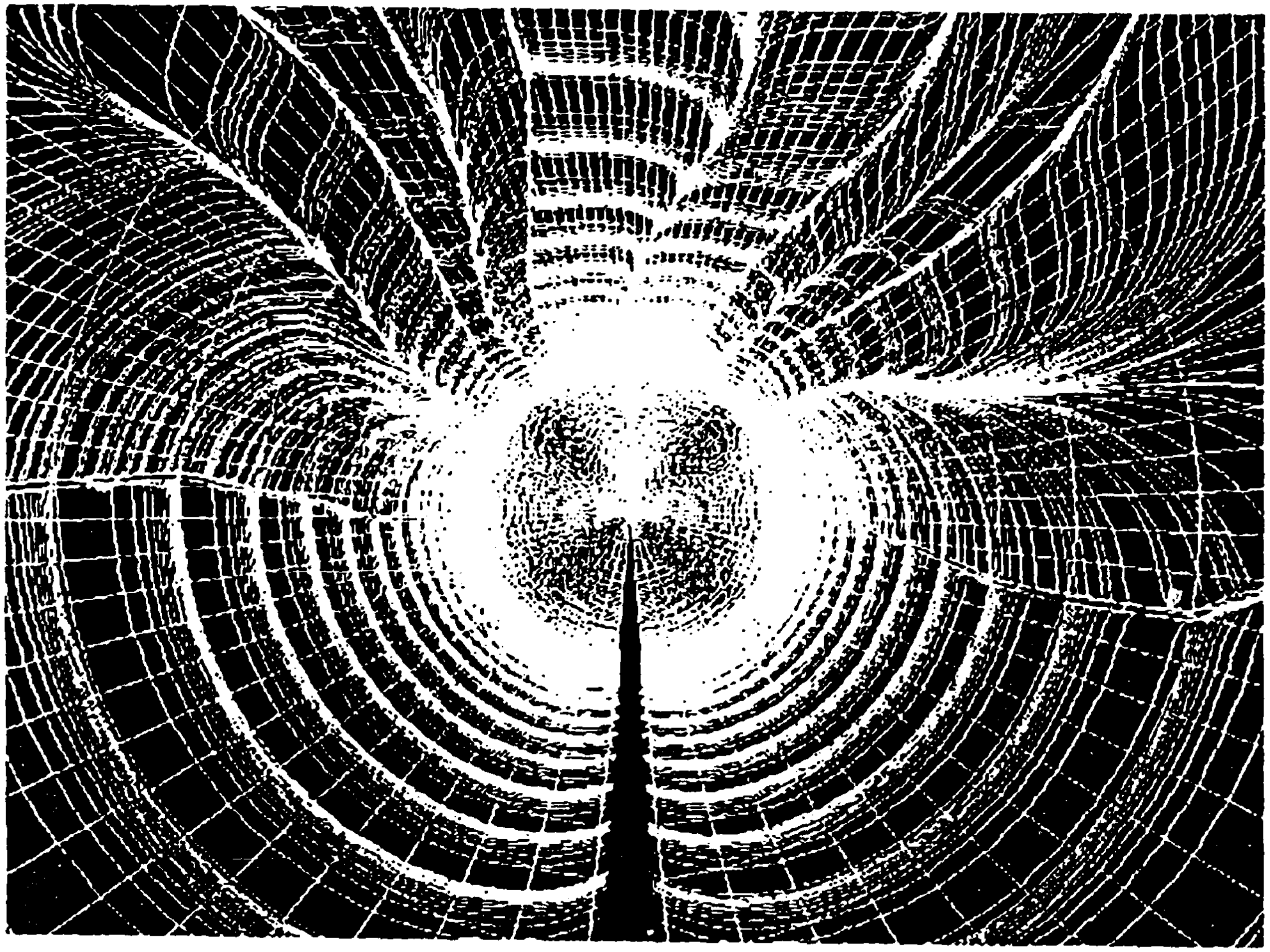

Figure 59. Rear Body Limiting Streamlines - Alpha = 40.0 deg, X/L = 97.0%

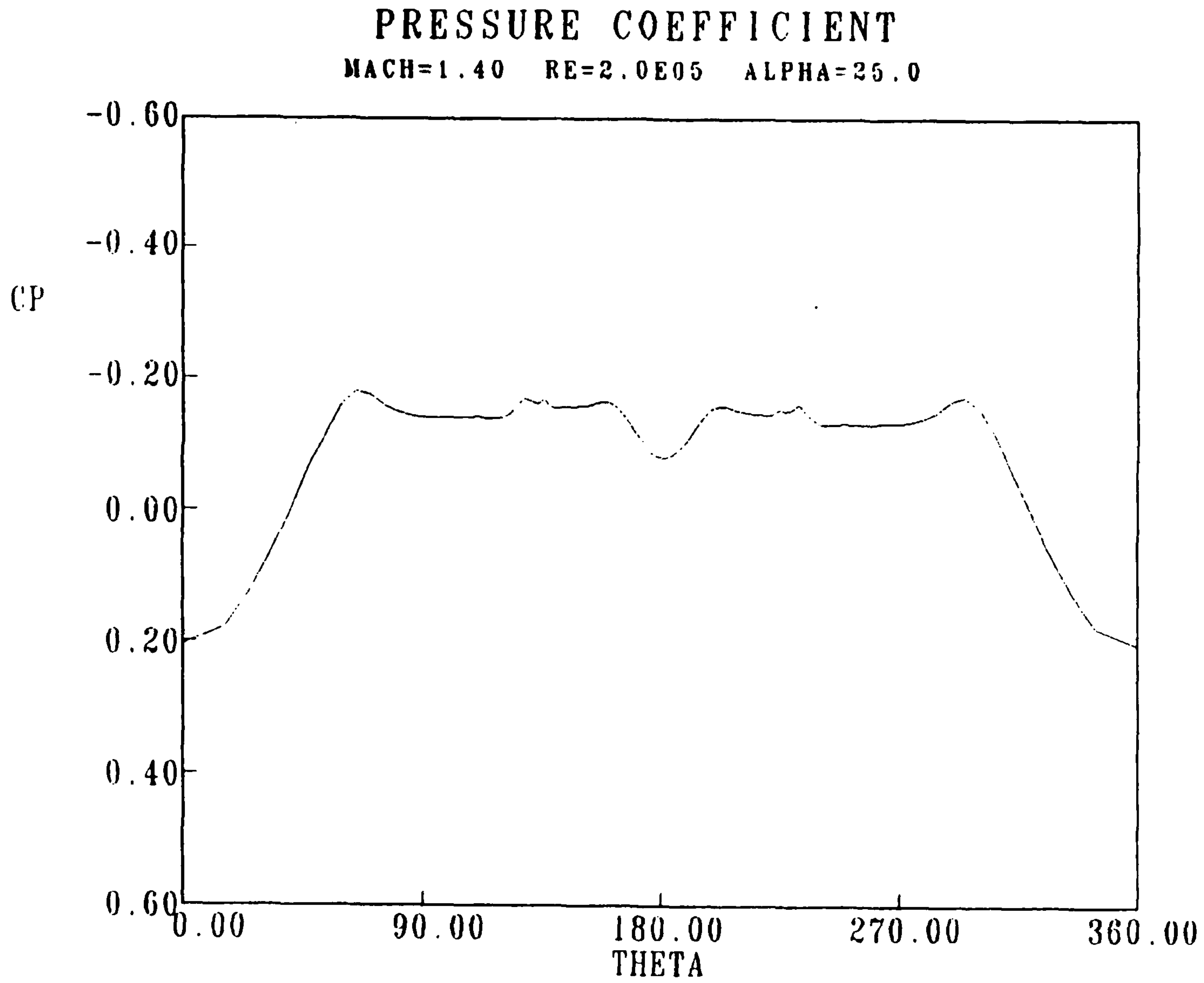

Figure 60. Circumferential Pressure Coefficient - Alpha = 25.0 deg, X/L = 97.0%

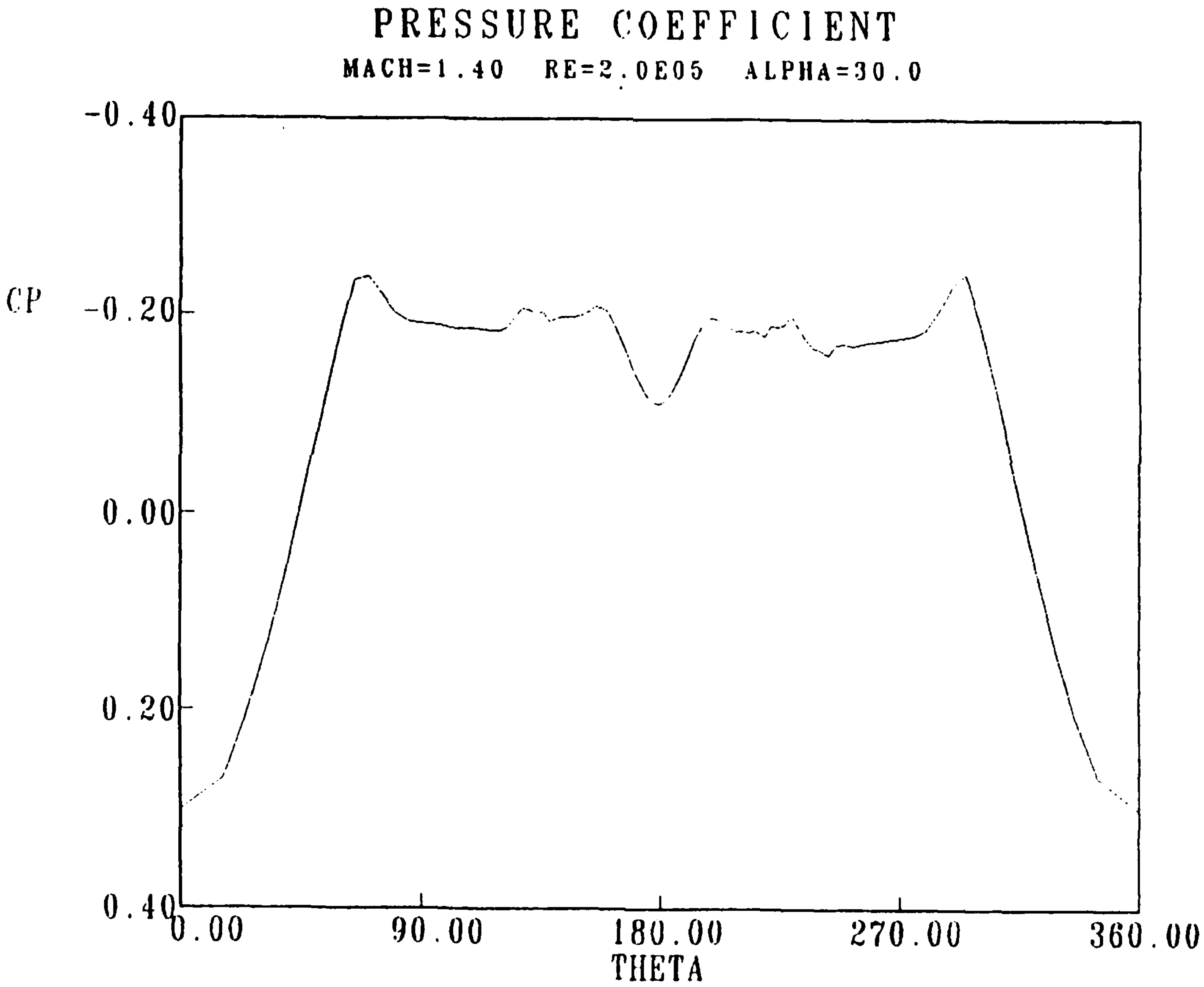

Figure 61. Circumferential Pressure Coefficient - Alpha = 30.0 deg, X/L = 97.0%

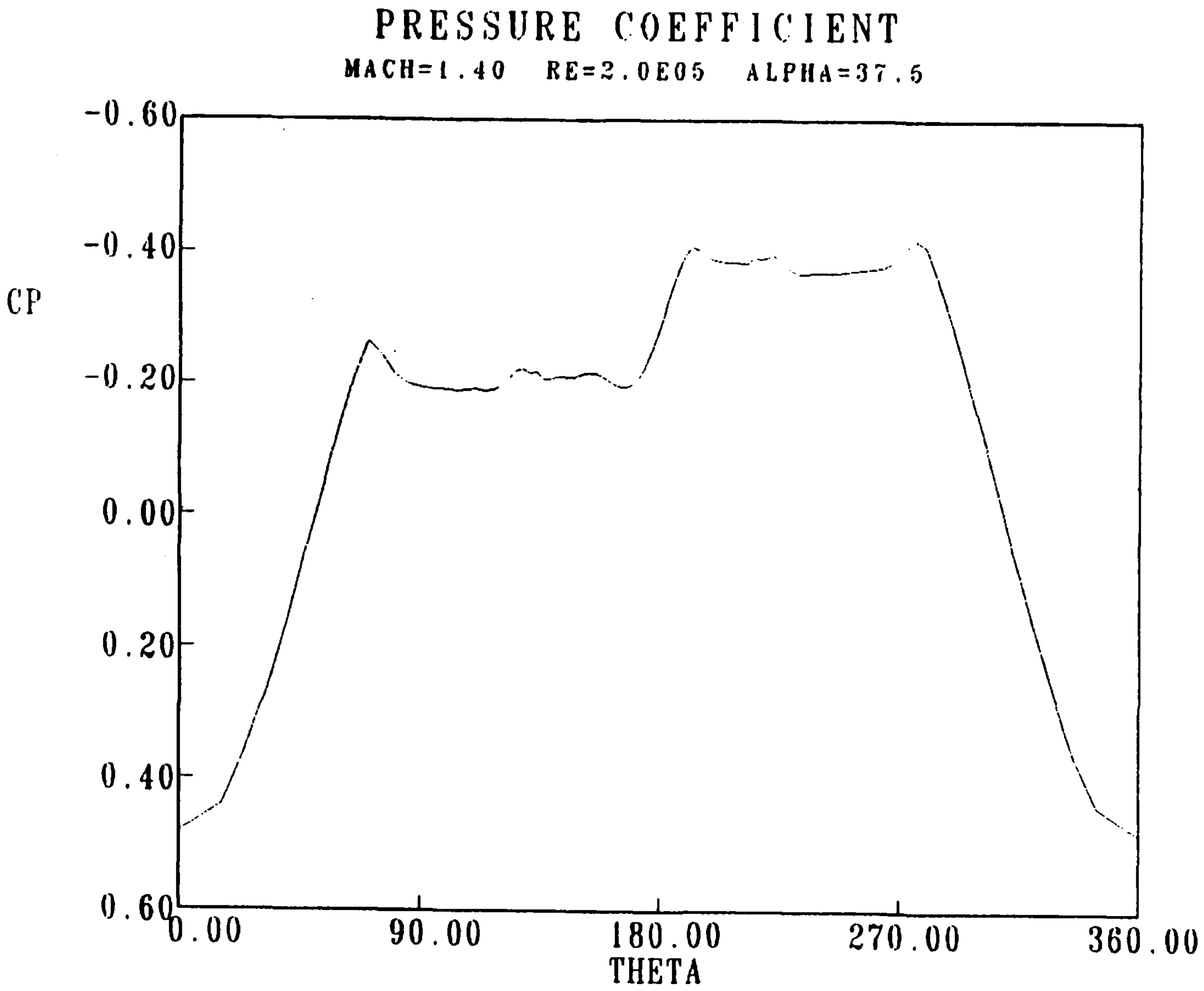

Figure 62. Circumferential Pressure Coefficient - Alpha = 37.5 deg, X/L = 97.0%

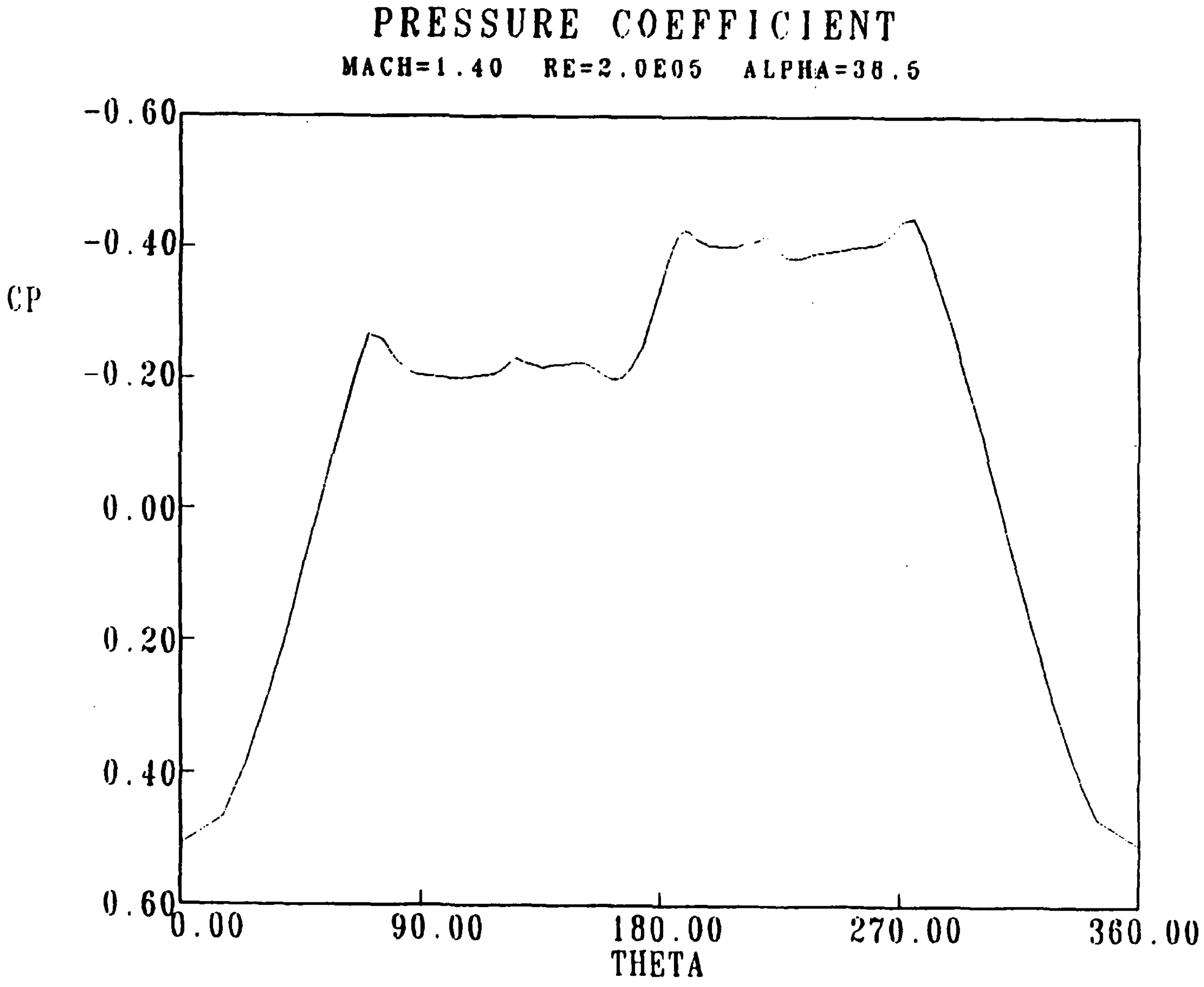

Figure 63. Circumferential Pressure Coefficient - Alpha = 38.5 deg, X/L = 97.0%

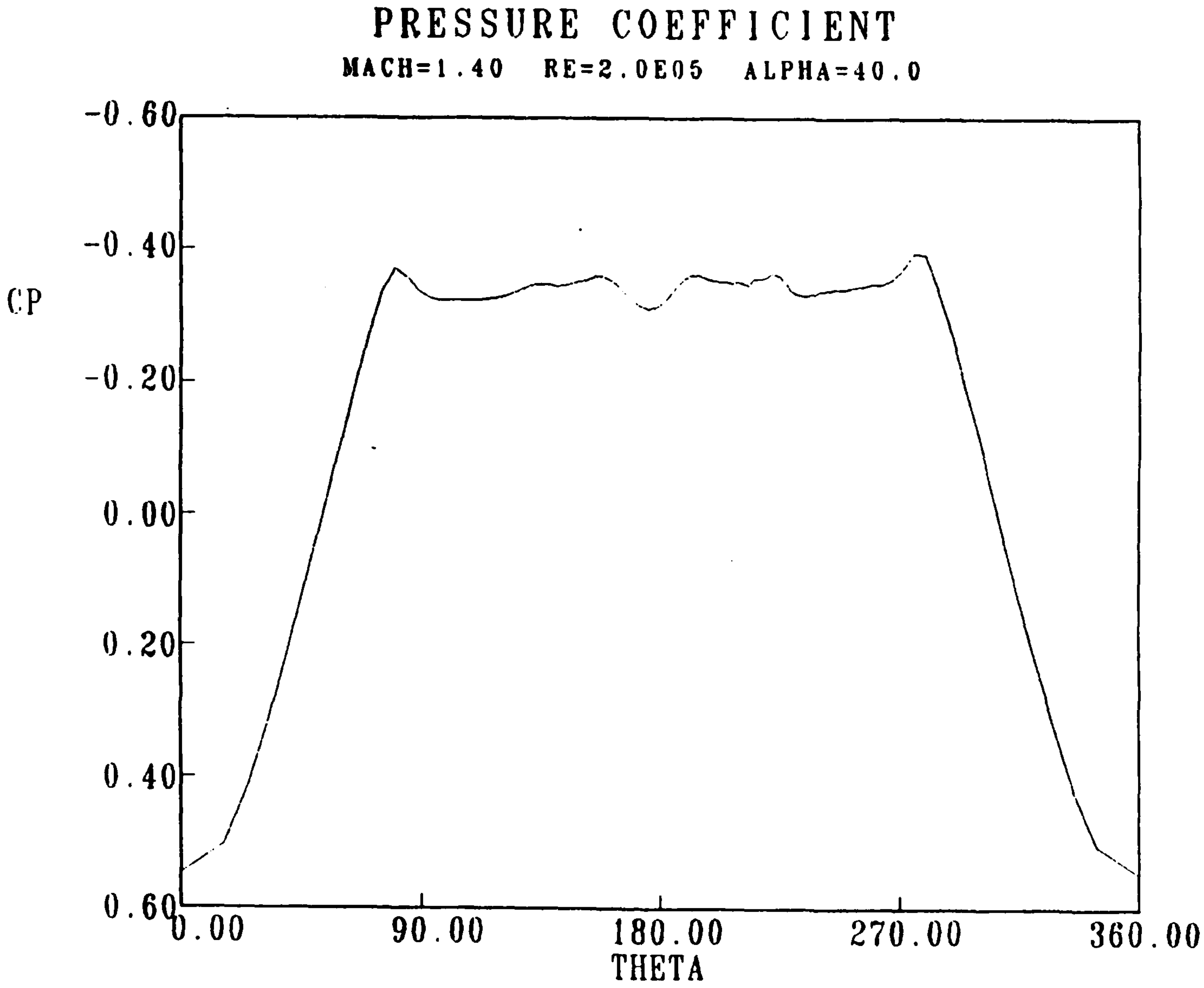

Figure 64. Circumferential Pressure Coefficient - Alpha = 40.0 deg, X/L = 97.0%

Alpha	Normal Force	Pitch Moment	Side Force	Yaw Moment
25.0	-4.25	25.68	0.0065	0.03
30.0	-6.00	37.51	-0.2500	2.07
37.5	-9.05	59.567	-0.1200	1.48
38.5	-9.51	63.270	-0.3150	3.77
40.0	-10.16	68.179	-0.3550	3.95

Based on base area

Table 1. Forces and Moments

CHAPTER VI

CONCLUSIONS

Asymmetric vortical flow has been calculated numerically using a thin-layer Navier-Stokes algorithm. It was found that the thin-layer approximation models the physics acceptably in both the boundary-layer and outer flow regions.

Both symmetric and asymmetric cases were calculated and analyzed. The secondary flow was shown in detail. The basic structure was found to agree qualitatively with experimental results, and a number of additional structures and characteristics were observed. The complexity of the secondary flow region increased with angle of attack.

Crossflow topology diagrams were given for symmetric and asymmetric conditions to illustrate the fundamental difference between these conditions. Asymmetry, according to this research, was characterized by the change in the topological structure near the saddle point associated with the primary vortices. In addition, the creation of a vortex by the pinching of another vortex was found to occur. A saddle point was formed in the middle of this two vortex structure. This phenomenon was observed in both the primary and secondary flow.

In general, these results were in qualitative agreement with experimental data, but showed additional structures not observed previously.

REFERENCES

1. Keener, E.R., and Taleghani, J., "Wind Tunnel Investigations of the Aerodynamic Characteristics of Five Forebody Models at High Angles of Attack at Mach Numbers from 0.25 to 2," National Aeronautics and Space Administration Technical Memorandum NASA TM X-73076, December 1975.

2. McElroy, G.E., and Sharp, P.S., "An Approach to Stall/Spin Development and Test," American Institute of Aeronautics and Astronautics Paper AIAA 71-772, July 1971.

3. Mounts, J.S., Belk, D.M., and Whitfield, D.L., "Program EAGLE - Users's Manual Volume IV: Multi-block, Implicit, Steady-State Euler Algorithm," Air Force Armament Laboratory Technical Report AFATL-88-117, September 1988.

4. Chapman, G.T., "Nonlinear Problems in Flight Dynamics," National Aeronautics and Space Administration Technical Memorandum NASA-TM-85940, May 1984.

5. Legendre, R., "Separation de l'Ecoulement Laminaire Tridimensional," La Recherche Aeronautique, No. 54, pp. 3-8, November-December 1956.

6. Lamont, P.J., "Pressure Measurements on an Ogive Cylinder at High Angles of Attack with Laminar, Transitional, or Turbulent Separation," American Institute of Aeronautics and Astronautics Paper AIAA 80-1556, 1980.

7. Yanta, W.J., Wardlaw, A.B., and Sternklar, D., "Vortex Asymmetry Development on a Tanget Ogive," Naval Surface Weapons Center Technical Report NSWC 82-394, October 1982.

8. Keener, E.R., "Flow-Separation Patterns on Symmetric Forebodies," National Aeronautics and Space Administration Technical Memorandum NASA TM-86016, January 1986.

9. Keener, E.R., Chapman, G.T., and Kruse, R.L., "Effects of Mach Number and Afterbody Length on Aerodynamic Side Forces at Zero Sideslip on Symmetric Bodies at High Angles of Attack," American Institute of Aeronautics and Astronautics Paper AIAA 76-66, January 1976.

10. Keener, E.R., and Chapman G.T., "Onset of Aerodynamic Side Forces at Zero Sideslip on Symmetric Forebodies at High Angles of Attack," American Institute of Aeronautics and Astronautics Paper AIAA 74-770, August 1974.

11. Peake, D.J., Owen, F.K., and Johnson, D.A., "Control of Forebody Vortex Orientation to Alleviate Side Forces," American Institute of Aeronautics and Astronautics Paper AIAA 80-0183, January 1980.

12. Fidler, J.E., "Active Control of Asymmetric Vortex Effects," American Institute of Aeronautics and Astronautics Journal of Aircraft, Volume 18, pp. 267-272, April 1981.

13. Ying, S.X., Schiff, L.B., and Steger, J.L., "A Numerical Study of Three-Dimensional Separated Flow Past a Hemisphere Cylinder," American Institute of Aeronautics and Astronautics Paper AIAA 87-1207, June 1987.

14. Siclari, M.J., and Marconi, F., "The Computation of Navier-Stokes Solutions Exhibiting Asymmetric Vortices," American Institute of Aeronautics and Astronautics Paper AIAA 89-1817, June 1989.

15. Whitfield, D.L., "Implicit Upwind Finite Volume Scheme for the Three-Dimensional Euler Equations," Mississippi State University Report, MSSU-EIRS-ASE-85-1, Sepetmber 1985.

16. Belk, D.M. and Whitfield, D.L., "Time-Accurate Euler Equations Solutions on Dynamic Blocked Grids," American Institute of Aeronautics and Astronautics Paper AIAA 87-1127, June 1987.

17. Gatlin, B. and Whitfield, D.L., "An Implicit, Upwind, Finite-Volume Method for Solving The Three-Dimensional Thin-Layer Navier-Stokes Equations," American Institute of Aeronautics and Astronautics Paper AIAA-87-1149, June 1987.

18. Simpson, L.B., "Unsteady Three-Dimensional Thin-Layer Navier-Stokes Solutions on Dynamic Blocked Grids," Ph.D. Dissertation, Mississippi State University, December 1988.

19. Roe, P.L., "Approximate Riemann Solvers, Parameter Vector, and Difference Schemes," Journal of Computational Physics, Volume 43, pp. 357-372, 1981.

20. Davey, A., "Boundary-Layer Flow at a Saddle Point of Attachment," Journal of Fluid Mechanics, Volume 10, pp. 593-610, 1961.

21. Lighthill, M.J., "Attachment and Separation in Three-Dimensional Flow," Laminar Boundary Layers, Section II 2.6, L. Rosenhead, ed., Oxford University Press, pp. 72-82, 1963.

22. Smith, J.H.B., "Remarks on the Structure of Conical Flow," Royal Aircraft Establishment Technical Report RAE TR 69119, June 1969.

23. Perry, A.E., and Fairlie, B.D., "Critical Points in Flow Patterns," Advances in Geophysics, Volume 18B, pp. 299-315, 1974.

24. Hunt, J.C.R., Abell, C.J., Peterka, J.A., and Woo, H., "Kinematical Studies of the Flows Around Free or Surface-Mounted Obstacles; Applying Topology to Flow Visualization," Journal of Fluid Mechanics, Volume 86, Part 1, pp. 179-200, 1978.

25. Tobak, M. and Peake, D.J., "Topology of Three-Dimensional Separated Fluid Flows," Annual Review of Fluid Mechanics, Volume 14, pp. 61-85, 1982.

26. Sears, W.R., "The Boundary Layer of Yawed Cylinders," Journal of Aeronautical Sciences, Volume 15, Number 1, pp. 49-52, January 1948.

27. Legendre, R., "Lignes de Courant d'un Ecoulement Continu," Recherche Aerospatiale., Number 105, pp. 3-9, 1965.

28. Thompson, J.F., "Program EAGLE - User's Manual, Volumes II and III," Air Force Armament Laboratory Technical Report AFATL-TR-88-117, September 1988.

29. Binion, T.W., and Stanewsky, E., "Observed Reynolds Number Effects: Low Aspect Ratio Wings and Bodies," Advisory Group for Aerospace Research and Development Conference Proceedings AGARD CP-232, 1989.

30. Walatka, P.P. and Buning, P.G., "PLOT3D User's Manual," National Aeronautics and Space Administration Technical Memorandum NASA TM-101067, 1989.

31. Bouard, R., and Coutanceau, M., "The Early Stage of Development of the Wake Behind an Impulsively Started Cylinder for 40<RE<10,000," Journal of Fluid Mechanics, Volume 101, Part 3, pp. 583-607, 1980.

32. Peake, D.J., and Tobak, M., "On Issues Concerning Flow Separation and Vortical Flows in Three Dimensions," Advisory Group for Aerospace Research and Development Conference Proceedings AGARD CP-342, April 1983.

33. Ericsson, L.E., and Reding, J.P., "Asymmetric Vortex Shedding From Bodies of Revolution," Progress in Aeronautics and Astronautics Volume 104, "Tactical Missile Aerodynamics," American Institute of Aeronautics and Astronautics, 1986.

34. Ericsson, L.E., and Reding, J.P., "Vortex-Induced Asymmetric Loads in 2-D and 3-D Flows," American Institute of Aeronautics and Astronautics Paper AIAA 80-1269, 1980.